

Universidade Federal de Juiz de Fora  
Engenharia Elétrica  
Programa de Pós-Graduação em Engenharia Elétrica

**Leonardo de Mello Brandão Abdo Dib**

**Multichirp Code Division Multiple Access For Smart Grids and Internet of  
Things**

Juiz de Fora

2018

Leonardo de Mello Brandão Abdo Dib

**Multichirp Code Division Multiple Access For Smart Grids and Internet of Things**

Dissertação apresentada ao Programa de Pós-Graduação em Engenharia Elétrica da Universidade Federal de Juiz de Fora, na área de concentração em sistemas eletrônicos, como requisito parcial para obtenção do título de Mestre em Engenharia Elétrica.

Orientador: Moisés Vidal Ribeiro

Juiz de Fora

2018

Ficha catalográfica elaborada através do Modelo Latex do CDC da  
UFJF com os dados fornecidos pelo(a) autor(a)

de M. B. A. Dib, Leonardo.

Multichirp Code Division Multiple Access For Smart Grids and Internet  
of Things / Leonardo de Mello Brandão Abdo Dib. – 2018.

85 f. : il.

Orientador: Moisés Vidal Ribeiro

Dissertação (Mestrado) – Universidade Federal de Juiz de Fora, En-  
genharia Elétrica. Programa de Pós-Graduação em Engenharia Elétrica,  
2018.

1. Comunicação híbrida. 2. Transformada discreta de Fresnel. 3. Mul-  
tichirp code division multiple access. I. Vidal Ribeiro, Moisés, orient. II.  
Título.

Leonardo de Mello Brandão Abdo Dib

**Multichirp Code Division Multiple Access For Smart Grids and Internet of Things**

Dissertação apresentada ao Programa de Pós-Graduação em Engenharia Elétrica da Universidade Federal de Juiz de Fora, na área de concentração em sistemas eletrônicos, como requisito parcial para obtenção do título de Mestre em Engenharia Elétrica.

Aprovada em:

BANCA EXAMINADORA

---

Prof. Dr. Moisés Vidal Ribeiro - Orientador  
Universidade Federal de Juiz de Fora

---

Professor Dr. Ricardo Suyama  
Universidade Federal do ABC

---

Professor Dr. Alexandre Bessa dos Santos  
Universidade Federal de Juiz de Fora

## AGRADECIMENTOS

Agradeço a Deus por ter colocado pessoas muito especiais ao meu lado!

À minha família que me apoiou e entendeu todas as minhas ausências.

Ao Prof. Moisés, por toda oportunidade proporcionada e pela sincera amizade.

Ao Prof. Guilherme Colen por todo suporte e paciência no desenvolvimento deste trabalho.

Aos colegas do Lcom pelas contribuições e incentivo.

“A tarefa não é tanto ver aquilo que ninguém viu, mas pensar o que ninguém ainda pensou sobre aquilo que todo mundo vê.” (Arthur Schopenhauer)

## RESUMO

Este trabalho descreve características importantes de um sistema híbrido *power line communication* (PLC)/comunicação sem fio para aplicações smart grid (SG) e Internet das coisas (IoT). Além disso, discute as vantagens dos sistemas híbridos em comparação com os sistemas não híbridos. Estas vantagens são demonstradas não somente do ponto de vista técnico, mas também pela perspectiva de infraestrutura. Além disso, esta dissertação destaca uma conexão entre a capilaridade do IoT e a infraestrutura de comunicação fornecida pelo SG, bem como os aspectos de segurança que relacionam o contexto SG e IoT. Além disso, este trabalho aborda a influência do meio ambiente nas comunicações de rede elétrica e sem fio. Por outro lado, existe um enorme esforço de pesquisa em relação às tecnologias avançadas de comunicação de dados, considerando tanto as aplicações IoT de baixa taxa de bits quanto as aplicações SG, de modo a cumprir os requisitos de projeto para sistemas de telecomunicações. Com o objetivo de maximizar o uso da largura de banda disponível para aplicações PLC, esta dissertação faz uso do esquema *orthogonal chirp division multiplexing* (OCDM) que usa a transformada discreta de Fresnel de forma análoga à transformada discreta de Fourier. Trabalhos anteriores mostraram resultados de desempenho interessantes para esse esquema em aplicações de banda passante (por exemplo, comunicação sem fio, fibra óptica e mídia acústica subaquática). Este trabalho aborda a construção de versões do esquema OCDM que permitem a comunicação de dados usando sinais banda base, possibilitando a aplicação do esquema OCDM em sistemas PLC. Além disso, ele introduz um esquema baseado em vários usuários denominado *multichirp code division multiple access* (MCp-CDMA), que é uma combinação de CDMA e OCDM com o objetivo de acomodar um grande número de nós e *endpoints* para PLC de banda estreita e que também seja adequado para aplicações SG e IoT. Finalmente, os resultados numéricos apontam que, para um ambiente difícil e ruidoso, o esquema OCDM é capaz de suavizar o efeito do ruído impulsivo. Além disso, o esquema OCDM demonstrou resultados excepcionais quando o comprimento do canal é desconhecido comparativamente aos esquemas *Hermitian symmetric orthogonal frequency division multiplexing* e mono-portadora com prefixo cíclico. As simulações usando o esquema MCp-CDMA demonstraram grande estabilidade e consistência de desempenho entre os diferentes cenários analisados.

Palavras-chave: Comunicação híbrida. Transformada discreta de Fresnel. Multichirp code division multiple access.

## ABSTRACT

This work outlines important characteristics of hybrid power line communication (PLC)/wireless data communication system for smart grid (SG) and Internet of Things (IoT) applications. Moreover, it discusses the hybrid systems advantages in comparison to non-hybrid ones. These advantages are demonstrated not only in the technical point of view but also in the infrastructural perspective. Also, this thesis highlights a connection between the capillarity of IoT and the communication infrastructure provided by SG as well as the security aspects that relate SG and IoT context. Furthermore, this work addresses the environmental influence on wireless and power line communications. In another hand, there is a huge research effort regarding advanced data communication technologies considering both low bit rate IoT and SG applications in order to comply with the requirements to design telecommunications systems. Aiming to maximize the use of the available bandwidth for PLC applications, this thesis makes use of the orthogonal chirp division multiplexing (OCDM) scheme that uses discrete Fresnel transform in an analogous fashion as discrete Fourier transform. Previous works showed interesting performance results for such scheme in passband applications (e.g., wireless, optical fiber, and underwater acoustic media). This work addresses the design of versions of the OCDM scheme that can allow the data communication using baseband signals, making possible the application of the OCDM scheme in PLC systems. Furthermore, it introduces a multiuser based scheme termed multichirp code division multiple access (MCp-CDMA), which is a combination of CDMA and OCDM, in order to accommodate a large number of nodes and end-points aiming narrowband PLC that is also suitable for SG and IoT applications. Finally, numerical results point out that for a hard and noisy environment, OCDM scheme is able to soften the impulsive noise effect. Also, OCDM scheme demonstrated outstanding results when the channel length is unknown comparatively to Hermitian symmetric orthogonal frequency division multiplexing and single carrier-cyclic prefix schemes. The simulations using the MCp-CDMA scheme demonstrated great stability and performance consistency among the different scenarios analyzed.

Key-words: Hybrid communication. Discrete Fresnel transform. Multichirp code division multiple access.

## List of Figures

Figure 1 – Typical USA distribution network. . . . .	22
Figure 2 – Typical European distribution network. . . . .	22
Figure 3 – The Hybrid PLC/Wireless system approach. . . . .	29
Figure 4 – The downlink of the multichirp code division multiple access (MCp-CDMA) scheme for a PLC system. . . . .	34
Figure 5 – The block diagram of type-I OCDM: (a) represents $\mathcal{P}(\cdot)$ and (b) represents $\mathcal{Q}(\cdot)$ . . . . .	39
Figure 6 – Graphic representation of (a) mapping function $\nu(\cdot)$ and (b) mapping function $\xi(\cdot)$ . . . . .	40
Figure 7 – Spectrogram for type-I OCDM: sub-chirp #130 from a 256-length symbol considering quadrature phase shift keying (QPSK) modulation. . . . .	42
Figure 8 – Graphic representation of $\zeta(\cdot)$ for (a) type-II and (b) type-IV. . . . .	44
Figure 9 – Block diagram of the type-II and type-IV OCDM schemes: (a) represents $\mathcal{P}(\cdot)$ and (b) represents $\mathcal{Q}(\cdot)$ . . . . .	45
Figure 10 – Spectrogram for the type-II OCDM scheme: sub-chirp #130 from a 256-symbol length considering QPSK modulation. . . . .	46
Figure 11 – Spectrogram for the type-IV OCDM scheme: sub-chirp #130 from a 256-symbol length considering QPSK modulation. . . . .	47
Figure 12 – Graphic representation of the artificial insertion of the Hermitian symmetric property for a type-III OCDM. . . . .	47
Figure 13 – Block diagram of the OCDM type-III scheme: (a) represents $\mathcal{P}(\cdot)$ and (b) represents $\mathcal{Q}(\cdot)$ . . . . .	48
Figure 14 – Block diagram for $\mathcal{Q}(\cdot)$ of the type-III OCDM scheme with reduced implementation complexity. . . . .	50
Figure 15 – Spectrogram for the type-III OCDM scheme: sub-chirp #130 from a 256-symbol length considering QPSK modulation. . . . .	51
Figure 16 – Single-user representation block diagram. . . . .	52
Figure 17 – Normalized CFR of the PLC channel considered for performance analyses. . . . .	53
Figure 18 – BER performances considering the AWGN channel model and both binary phase shift keying (BPSK) and QPSK modulations. . . . .	54
Figure 19 – BER performances considering the ABGN channel model and both BPSK and QPSK modulations. . . . .	55
Figure 20 – BER performance considering BPSK and power line communication (PLC) channel model corrupted by additive white Gaussian noise (AWGN): (a) $L_{cp} = 100\%$ of $L_1$ ; (b) $L_{cp} = 50\%$ of $L_1$ ; (c) $L_{cp} = 23\%$ of $L_1$ ; (d) $L_{cp} = 10\%$ of $L_1$ . . . . .	59

Figure 21 – BER performance considering QPSK and PLC channel model corrupted by AWGN: (a) $L_{cp} = 100\%$ of $L_1$ ; (b) $L_{cp} = 50\%$ of $L_1$ ; (c) $L_{cp} = 23\%$ of $L_1$ ; (d) $L_{cp} = 10\%$ of $L_1$ . . . . .	60
Figure 22 – BER performance considering BPSK and PLC channel model corrupted by ABGN: (a) $L_{cp} = 100\%$ of $L_1$ ; (b) $L_{cp} = 50\%$ of $L_1$ ; (c) $L_{cp} = 23\%$ of $L_1$ ; (d) $L_{cp} = 10\%$ of $L_1$ . . . . .	61
Figure 23 – BER performance considering QPSK and PLC channel model corrupted by ABGN: (a) $L_{cp} = 100\%$ of $L_1$ ; (b) $L_{cp} = 50\%$ of $L_1$ ; (c) $L_{cp} = 23\%$ of $L_1$ ; (d) $L_{cp} = 10\%$ of $L_1$ . . . . .	62
Figure 24 – Comparison among MCp-CDMA, multicarrier code division multiple access (MC-CDMA) and single carrier-code division multiplexing (SC-CDMA) Four-user PLC channel+AWGN: (a) BPSK, $L_{cp} = 100\%$ of $L_j$ ; (b) QPSK, $L_{cp} = 100\%$ of $L_j$ ; (c) BPSK, $L_{cp} = 10\%$ of $L_j$ ; (d) QPSK, $L_{cp} = 10\%$ of $L_j$ . . . . .	67
Figure 25 – Comparison among MCp-CDMA, MC-CDMA and SC-CDMA Four-user PLC channel+additive Bernoulli-Gaussian noise (ABGN): (a) BPSK, $L_{cp} = 100\%$ of $L_j$ ; (b) QPSK, $L_{cp} = 100\%$ of $L_j$ ; (c) BPSK, $L_{cp} = 10\%$ of $L_j$ ; (d) QPSK, $L_{cp} = 10\%$ of $L_j$ . . . . .	68
Figure 26 – Comparison among each the four users for type-III MCp-CDMA: (a) BPSK and AWGN channel model; (b) QPSK and AWGN channel model; (c) BPSK and PLC channel model corrupted by AWGN; (d) QPSK and PLC channel model corrupted by AWGN. . . . .	69
Figure 27 – Comparison among each the four users for type-III MCp-CDMA: (a) BPSK and ABGN channel model; (b) QPSK and ABGN channel model; (c) BPSK and PLC channel model corrupted by ABGN; (d) QPSK and PLC channel model corrupted by ABGN. . . . .	70
Figure 28 – (a) Sub-chirp #130 spectrogram from a 256-length symbol of an orthogonal chirp division multiplexing (OCDM) scheme. (b) Sub-carrier #165 spectrogram from a 256-length symbol of an orthogonal frequency division multiplexing (OFDM) scheme. (c) Sub-symbol #130 spectrogram from a 256-length symbol of a single carrier-cyclic prefix (SC-CP) scheme. All indicated schemes employ QPSK modulation as input data.	81
Figure 29 – Sub-chirp #130 Spectrogram from a 256-length symbol of an OCDM scheme employing QPSK modulation as input data. . . . .	82
Figure 30 – QR Codes for video showing the spreading effect obtained for types I-IV and passband OCDM considering a 256-length symbol. . . . .	84

## List of Tables

Table 1 – Correspondence between $L_{cp}$ reduction and its associated CIR energy. . .	55
--	----

## ACRONYMS

<b>ABGN</b>	additive Bernoulli-Gaussian noise
<b>AMI</b>	automated meter infrastructure
<b>AMR</b>	automatic meter reading
<b>AWGN</b>	additive white Gaussian noise
<b>BER</b>	bit error rate
<b>BPSK</b>	binary phase shift keying
<b>CDMA</b>	code division multiple access
<b>CFR</b>	channel frequency response
<b>CIR</b>	channel impulse response
<b>C-LAN</b>	classified local area network
<b>CP</b>	cyclic prefix
<b>CSS</b>	chirp spread spectrum
<b>CSI</b>	channel state information
<b>CT</b>	current transformer
<b>CZT</b>	chirp Z-transform
<b>DA</b>	distribution automation
<b>DFT</b>	discrete Fourier transform
<b>DFnT</b>	discrete Fresnel transform
<b>DG</b>	distributed generation
<b>DS-CDMA</b>	direct sequence code division multiple access
<b>DSSS</b>	direct sequence spread spectrum
<b>ERT</b>	encoder receiver transmitter
<b>FDE</b>	frequency-domain equalizer
<b>FSS</b>	frequency-selective surface
<b>HS</b>	Hermitian symmetric

**HS-OFDM** Hermitian symmetric OFDM

**IoT** Internet of things

**ISI** intersymbol interference

**LV** low-voltage

**LV/MV** low-voltage/medium-voltage

**LP-RF** low-power radio frequency

**LPTV** linear periodically time-variant

**LPWAN** Low-power wide-area network

**LTI** linear and time invariant

**MC-CDMA** multicarrier code division multiple access

**MC<sub>p</sub>-CDMA** multichirp code division multiple access

**NB-PLC** narrowband power line communication

**OCDM** orthogonal chirp division multiplexing

**OFDM** orthogonal frequency division multiplexing

**PLC** power line communication

**P/S** parallel/serial

**QPSK** quadrature phase shift keying

**SC-CDMA** single carrier-code division multiplexing

**SC-CP** single carrier-cyclic prefix

**S<sub>F</sub>** spreading factor

**SG** smart grid

**SM** smart meter

**SNR** signal-to-noise ratio

**S/P** serial/parallel

**TOU** time-of-use

**UNB** ultra narrowband

**UNB-PLC** ultra narrowband power line communication

**ZF** zero forcing

## CONTENTS

<b>1</b>	<b>INTRODUCTION . . . . .</b>	<b>15</b>
1.1	OBJECTIVES . . . . .	16
1.2	THESIS ORGANIZATION . . . . .	16
<b>2</b>	<b>HYBRID PLC/WIRELESS COMMUNICATION FOR SMART GRIDS AND THE INTERNET OF THINGS . . . . .</b>	<b>18</b>
2.1	THE HYBRID PLC/WIRELESS DATA COMMUNICATION . . . . .	18
2.1.1	<b>Power line communication . . . . .</b>	<b>19</b>
2.1.2	<b>Wireless communication . . . . .</b>	<b>20</b>
2.2	THE PREFERENCE FOR WIRELESS OR PLC . . . . .	21
2.2.1	<b>Environmental influence on data communications . . . . .</b>	<b>23</b>
2.3	SECURITY ASPECTS . . . . .	24
2.4	IOT ROLE IN SG DOMAIN . . . . .	26
2.5	HYBRID DATA COMMUNICATION SYSTEMS . . . . .	28
<b>3</b>	<b>MULTIUSER BASEBAND ORTHOGONAL CHIRP DIVI- SION MULTIPLEXING . . . . .</b>	<b>30</b>
3.1	PROBLEM STATEMENT . . . . .	31
3.2	DISCRETE FRESNEL TRANSFORM . . . . .	37
3.3	THE OCDM FOR BASEBAND DATA COMMUNICATION . . . . .	38
3.3.1	<b>The type-I OCDM scheme . . . . .</b>	<b>39</b>
3.3.2	<b>The type-II and type-IV OCDM schemes . . . . .</b>	<b>42</b>
3.3.3	<b>The type-III OCDM scheme . . . . .</b>	<b>45</b>
3.4	SIMULATION RESULTS . . . . .	50
3.4.1	<b>The OCDM scheme: single-user analyses . . . . .</b>	<b>52</b>
3.4.2	<b>Multuser analyses . . . . .</b>	<b>63</b>
<b>4</b>	<b>CONCLUSIONS . . . . .</b>	<b>71</b>
4.1	FUTURE WORKS . . . . .	72
	<b>REFERENCES . . . . .</b>	<b>73</b>
	<b>Appendix A – SPREADING FORMS FOR OCDM, OFDM AND SC-CP SCHEMES . . . . .</b>	<b>81</b>
	<b>Appendix B – QR Codes . . . . .</b>	<b>83</b>

Appendix C – PUBLICATIONS . . . . . 85

## 1 INTRODUCTION

The world today is undergoing a very rapid change regarding the behaviors and habits related to the use of telecommunication technologies. Easy information access, real time data transfer based on the use of widespread and low-cost of data communication technologies are increasing the level of user and machine demands. Smart devices and smart things are continuously requiring a reliable (and also cost-effective) data communication solutions. In this context, the incessant search for advanced data communication technologies that are capable of offering improved trade off among performance, reliability, availability, coverage, security, cost is driving R&D efforts from research centers and industries around the world.

In this context, Internet of things (IoT) and smart grid (SG) demands and requirements are at the center of the discussion about advances in telecommunication industry as these applications rely on intensive connectivity between devices and equipment that constitute the nodes of a data network designed for assisting the successful deployment of these technologies. As a matter of fact, these applications are more oriented to exchange short data packets with a high level of security because such data packets are responsible for exchanging important information of the cyber-physical systems.

In this regards, it is recognized that the distribution automation (DA), which previously demanded a specific and not widely accessible technology, today has IoT as an ally, facilitating the integration of devices and systems in a more direct and simple way. More than 130 years had passed since the electricity started being generated and distributed in European and North American cities and just now we have a chance to make significant improvements to the existing electric power distribution by means of SG concept. But all this support was only possible thanks to the insertion of a data communication infrastructure that allows intelligent, accessible and controllable equipment on the field. At this point two communication technologies arise naturally as candidates: PLC and wireless communication. If for one side, the PLC technology has the advantage of making use of existing electric cables, not requiring new infrastructure for its use, on the other side, the wireless technology has the advantage of its inherent mobility and also being a more established technology. Which communication technology should be used? Why not both? In this circumstances, PLC and wireless communication, working together, can complete each other in many positive aspects for both SG and IoT applications.

Moreover, there is a huge research effort to come up with advanced data communication technologies that are capable of fulfilling the constraints applied to design telecommunications systems oriented for both low bit rate IoT and SG applications, regardless the channel conditions. Currently, there are initiatives based on 5G that has a potential to satisfy astonishing data communication demands related to these technolo-

gies. Regarding the physical layer, the use of single-carrier-, multicarrier-, and spread spectrum-based technologies is being widely applied. For instance, SigFox applies ultra narrowband (UNB) technology, using only 100 Hz for each user, which ensures a reduced noise perception from the received message and also increases the possible number of users utilizing the system [1]; LoRA makes use of chirp spread spectrum (CSS), which uses linear frequency modulated chirp pulses to encode information [2]; narrowband power line communication (NB-PLC) applies single-carrier or multicarrier modulation technique, aiming the communication reliability, depending on the strategy adopted by each development [3], to name a few. Based on the fact that the large number of nodes in the data networks applied to assist the IoT and SG applications is large, the use of multiuser techniques at the physical layer starts to be interesting, mainly when a coordinator is used to organize the data communication among the nodes connected to the data networks or with other data networks.

## 1.1 OBJECTIVES

The discussion about telecommunications perspectives to assist the massive deployment of the IoT and SG applications is huge. However, the previous discussion has brought the attention to two interesting aspects to be investigated. In this regard, the aims of this thesis are as follows:

- To provide a discussion about the hybrid data communication technologies and their comparison to non-hybrid ones. Also, the idea is to show a comparison not only in the technical point of view, but also in the infrastructural perspective. In addition, a connection between the capillarity of IoT and the communication infrastructure provided by SG is highlighted. Moreover, a discussion regarding the environmental influences on PLC and wireless communication is held which also covers important security aspects.
- To introduce and analyze different configuration types for the recently released OCDM scheme with the view to allow baseband communication and also to introduce a combination of code division multiple access (CDMA) and OCDM, giving rise to the named multichirp code division multiple access (MCp-CDMA), which is a multiuser based scheme, aiming narrowband PLC for SG and IoT applications in order to accommodate a large number of nodes and end-points. All analyses take into account the performances obtained with the use of the MCp-CDMA scheme in a single-user and also in a multiuser context.

## 1.2 THESIS ORGANIZATION

This thesis is organized as follows:

- Chapter 2 discusses a historical overview of PLC and wireless technologies, and their interaction on the development of the automatic meter reading (AMR) and automated meter infrastructure (AMI) applications. Furthermore, the environmental importance of PLC and wireless communications are considered in this discussion. Security issues, as well as real cases occurrence regarding this aspect, are explored. Also, a classification of security attacks treated in the literature is described. The interaction between SG and IoT is enhanced, considering the benefits for each one when these both concepts are put together, working in a win-win situation.
- Chapter 3 treats the situation of a multiuser based communication scheme for SG and IoT applications, allowing simultaneous data transmission to several users. This chapter considers the use of OCDM scheme, that applies the discrete Fresnel transform (DFnT) in an analogous fashion as the discrete Fourier transform (DFT), introducing the MCp-CDMA scheme for handling with multiuser data communication associated with the SG and IoT applications in a PLC environment. Moreover, numerical results and analyses are performed for MCp-CDMA considering single- and multiuser configurations.
- Chapter 4 states concluding remarks of this thesis, as well as suggestions for future works.

## 2 HYBRID PLC/WIRELESS COMMUNICATION FOR SMART GRIDS AND THE INTERNET OF THINGS

SG and IoT are promising technologies for electric power grid management. Many efforts have been made so far in order to demonstrate how complex electric power grids can become intelligent and reliable but, despite all techniques available today, the grid is still not effectively “smart”. It is true that such process is slower than what was initially predicted, but it is also true that this is a way of no return.

The key factor for SG and IoT is certainly the communication infrastructure. The path connecting the end-devices to the system gateway or concentrator part is what brings effectiveness to the smart portion of the electric power grid. The type of technology that will connect the entities of the SG and IoT systems must be adequate for the required data rate and also appropriate for the environment in which the data communication path is constituted, giving the right reliability for each application in service. On the top of that, the concern about security is a subject that must be carried out with severity.

The target for a hybrid PLC/wireless data communication system is to increase data communication reliability. Such concept is still not widely implemented and there is a noticeable lack of contribution regarding this subject. In this context, the chapter aims to discuss a historical overview of PLC and wireless technologies as well as a reference about the use of each one regarding AMR and AMI applications. Also, environmental influences on both power line and wireless communications are addressed. Also, it focuses on SG and IoT applications and the inevitable interaction between them.

This chapter is organized as follows: Section 2.1 discusses and defines hybrid PLC/wireless data communication concept for the context of this thesis. Subsection 2.1.1 outlines characteristics and drawbacks of PLC technology, while Subsection 2.1.2 discusses challenges and working architecture evolutions regarding wireless communication technology. Section 2.2 addresses how electric power grids induct the use of wireless or power line as communication technology for AMR and AMI applications. Furthermore, Subsection 2.2.1 addresses the environmental influence on wireless communication and PLC. Section 2.3 briefly discusses security aspects for SG and IoT implementations. IoT interaction within a SG deployment is addressed in Section 2.4. The advantages of a hybrid PLC/wireless data communication system are highlighted in Section 2.5.

### 2.1 THE HYBRID PLC/WIRELESS DATA COMMUNICATION

PLC [4–6] and wireless communication systems have been used to constitute pathways to SG and IoT implementations, but commonly only one of these technologies is considered in the project design. There are unquestionable environmental influences on both electric power grid and wireless media that provide advantages and disadvantages

for data communication purposes. We come up in this chapter that PLC and wireless are complementary technologies when the ambient conditions are subjected to unexpected modifications and when there is a need to be flexible in terms of data communication technology. PLC or wireless, working alone, will not fulfill all communication needs.

Nowadays, the consumers are starting to experience the advantages of producing part of their electric energy using distributed generation (DG), where the most used types of power generation are photovoltaic panels and wind turbines. During part of the day or when the natural resource is sufficiently available, the energy can be generated and stored in batteries for further use. In terms of reliability, DG can be considered a form of diversifying the power generation source, having more than one method for achieving its target (an hybrid method), that is, in this particular case, to have electric energy available for immediate consumption. The same relation can be applied to the data communication infrastructure, combining and creating redundancy to the critical and essential data communication path. This is the so-called heterogeneous data communication architecture or also hybrid data communication system.

In 2005, a first discussion regarding hybrid data communication system was held [7], but it considered PLC and wireless technologies not working at the same time. Hybrid data communication system, at that time, was defined as the ability to join two or more access technologies; however, working in cascade (a serial approach). A similar hybrid definition was shown in [8] involving in-home and vehicular applications and also in [9] for AMI application. A hybrid PLC/wireless solution for AMI application, which considered PLC and wireless working at the same time was presented in [10] and [11]. The simultaneous use of indoor PLC and wireless communication was analyzed in [12] aiming to investigate the performance of the link throughput. Hybrid data communication link considering SG applications was discussed in [13]. Full-hybrid wireless and PLC channels aiming in-home applications as an alternative to enhance the wireless indoor access link was presented in [14], which also became a patent [15]. Nevertheless, a restricted number of works considering cooperative protocols together with the hybrid data communication concept are available in technical literature: [16] showed a hybrid PLC/wireless data communication system and [17] considered a cooperative system that cascades wireless and PLC links, working separately in distinct segments of the system.

### 2.1.1 Power line communication

Research and development efforts in PLC area moved it from an initial simple signaling application to an addressable technology for AMR and AMI deployments [18,19]. The use of PLC was also pushed by the intrinsic characteristic of power lines: it is an ubiquitous infrastructure, unlike any other available option. Moreover, the PLC has a very useful advantage for providing data communication for sensing and SG devices

(e.g., PLC can be used for detecting and locating high impedance faults and power cable aging [20, 21]).

The data communication technologies available for SG and IoT markets are already changing slightly the way we live today, but they are still limited in terms of range and data rate. The target in this role is to combine reliability and the lowest energy consumption with the lowest cost and, in this context, PLC can be as competitive as wireless [18]. Long distances can be achieved by ultra narrowband power line communication (UNB-PLC) systems if low data rate is an acceptable characteristic for the target application [22]. UNB-PLC operates in the range of 0.1-3 kHz, occupying a very small bandwidth. As a result, it will compromise the effective data rate of such data communication system (up to dozens of bps), but their signals are capable of passing through the low-voltage/medium-voltage (LV/MV) transformers. Depending on the application needs (one-way communication in order to read electricity meters located in remote or rural areas), low data rate can be enough as UNB-PLC keeps its reliability in such conditions. Successful examples of UNB-PLC technologies are the Turtle System and TWACS [22].

The easy integration among devices at a reasonable price will be an important legacy for automation engineering. NB-PLC technology is widely used for such task, after all, the data rates provided by NB-PLC is suitable for applications such as AMI, DA, and building & industrial automation (B&IA). NB-PLC considered in this chapter is a data communication via LV electric power grids which operates in the frequency bandwidth of 0-500 kHz and provides data rates of tens of kbps [23]. If compared to the broadband PLC (BPL, 1.7-250 MHz), which commonly requires a number of repeaters with a shorter distance among devices, NB-PLC has been considered the technology with best trade-off among communication distance range, low data rate requirement, and implementation cost.

NB-PLC can be subdivided into two categories: single-carrier and multicarrier, see PRIME, G3-PLC, ITU-T G.hnem, and IEEE 1901.2 standards [24].

### 2.1.2 Wireless communication

In the mid of 80s, the USA was using a simple wireless one-way on-off keying (OOK) modulated 900 MHz transmitter in their meters in order to make the reading easier by means of a handheld receiver (walk-by) and also by using a car equipped with receiver units (drive-by) [25]. Such data collection process called encoder receiver transmitter (ERT) is yet dependent on a manual activity; however, it is still in use today for gas, water, and electricity meters. The full automation of the meter reading process was effectively reached later using the already installed ERT meters and introducing a concentrator device equipped with a dial-up land line modem, providing the capability of having a different and smaller reading interval, rather than the usual standard monthly reading.

Cost-effective devices were always a premise for AMR and AMI markets as they drove the technology manufacturers to utilize the so-called unlicensed frequency bands. As well as, regulation compliances that have their specificities from country to country (besides the regions defined by International Telecommunication Union), together with the requirement of tolerating interference generated by other devices working in the same frequency band, motivated the evolution of wireless communications for SG and IoT to fulfill bi-directional and autonomous-generated data network needs. According to [26], a network formation should be designed to accommodate the trade-off between reliability and efficiency. Its working architecture also indicates the level of technical evolution, encompassing mesh-type networks as well as self-governing features such as self-healing and self-balancing functionalities.

Differently from PLC systems, wireless systems have the advantage of mobility, not being confined to electrical wiring extension. However, such characteristic can be also a vulnerability, as anyone inside the coverage range of the wireless signal can capture it. Spread-spectrum techniques grant some alleviation, as they reduce the chance of sensing the transmitted signal, distributing it over a large bandwidth. Naturally, this is not sufficient for wireless communications security, thus, defense strategies must be adopted. However, due to the limited computational resource available in wireless IoT sensors, there must be a balanced set of security features consistent to the risk of the target application [27].

There is also a challenge for applications demanding a battery operated device, like water/gas metering and IoT applications (e.g., personnel and equipment tracking, medical and healthcare wearables, agriculture and farm sensors, to name a few). Usually, these are low data rate applications and this condition alone is certainly an unprompted relief to battery consumption. Low-power wide-area network (LPWAN) is suited for such needs with the advantages of providing an extensive coverage range [28] and the low cost of the device nodes. Due to all these facts, there is a recent increasing interest in LPWAN for endpoint nodes of SG and IoT applications.

## 2.2 THE PREFERENCE FOR WIRELESS OR PLC

It is clear that, through the years, the technical characteristics of the outdoor LV electric power grids were determinant for the development of data communication technologies targeting AMR and AMI applications. Such development was mainly based on the cost effectiveness of each solution which is directly influenced by the number of consumers served by the distribution transformer. In the USA, the development was based on wireless technology for communicating with electricity meters rather than in Europe where PLC prevailed. Such situation is explained by the configuration difference of the existing outdoor LV electric power grids in the USA and Europe.

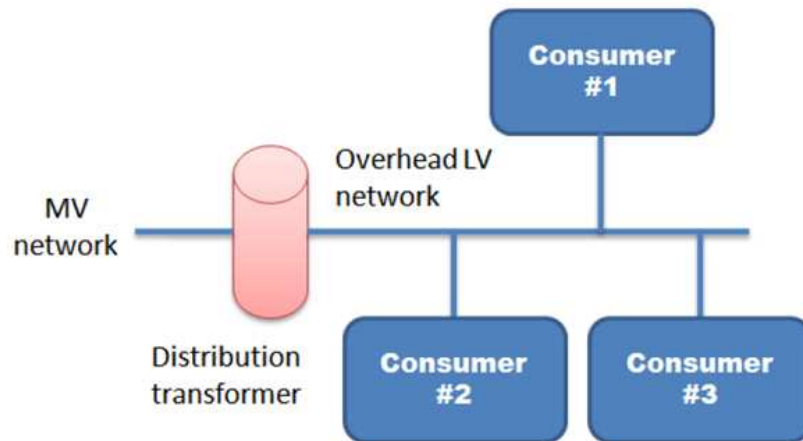


Figure 1: Typical USA distribution network.

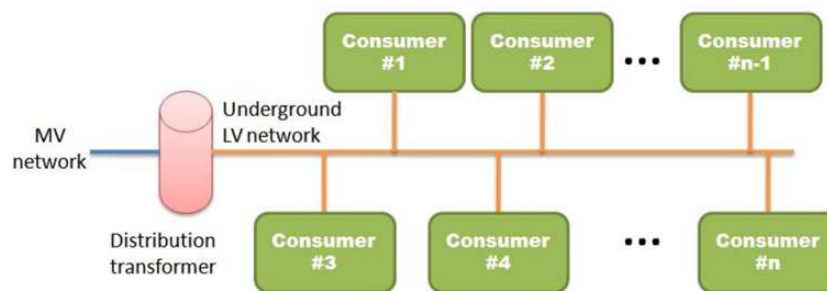


Figure 2: Typical European distribution network.

In fact, in the USA there are only a few houses connected to a distribution transformer (see Fig. 1), which makes the usage of PLC costly as each transformer typically needs a data concentrator [29]. On the other hand, the European outdoor LV electric power grids are installed underground and the distribution transformer serves in average 250-320 houses [3] as suggested in Fig. 2, which makes the PLC an effective data communication technology in terms of implementation costs.

In terms of coverage area, LV PLC systems will be confined by the electric circuit to which it is connected, this way one data concentrator typically will provide connectivity to the devices attached to the same circuit. On the other hand, wireless will cover an area without defined borders. If the PLC system has the functionality of self-registration, then all connected smart devices on the same circuit will be recognized by the data concentrator. From the point of view of the electric utility, such asset management control is highly desirable. In the case of wireless, this asset control needs a list indicating each equipment and its belonging LV electric circuit.

The many endpoints the system can support using a similar structure is the key for determining the effective implementation costs. This is an equation that must be treated also under the perspective of signal transmission integrity, which are extremely connected to the installation environment and will be discussed in the next section.

### 2.2.1 Environmental influence on data communications

Wireless and PLC suffer expressive influence of the environment in which they are immersed. This environmental influence can happen due to human interventions or natural causes. Some of the most common issues are as follows:

- Wireless signal attenuation due to rain and snow events: wireless communication suffers with obstructions in its path between two terminals. In this case, the higher is the center frequency of the signal, the higher is the attenuation introduced by natural events such as rain or snow. In other words, when a raindrop is as small as the wavelength, it becomes an obstruction for the data communication.
- Wireless communication path interruption: the point-to-point wireless communication is highly dependent on the path between the terminals. A tree growing or a building construction can reduce the line-of-sight propagation and greatly attenuate the signal carrying information.
- The mutual interference between wireless and PLC signals: it is yielded by a distinct user operating in the same frequency band. This issue can occur in any frequency band that is occupied by PLC and wireless systems.
- Interruption of the power line: it is related to a fall of a pole, a fall of a tree over the power line, a cable breaking, or a high impedance fault. These problems can happen due to a car crash or even a strong storm.
- Power cable aging: it degrades the data communication medium as the time goes by [30] and, as a consequence, the PLC performance will be seriously affected.

Also, their performance is highly dependent on the propagation frequency band. Wireless devices emitting signals of around 900 MHz tend to have a wider distance range if compared to higher frequencies devices, like 2.4 GHz or even 5.8 GHz, due to the wavelength associated with each frequency and how they interact with the environment obstructions, or more specifically, how the signal carrying information is affected by the phenomena of reflection, refraction, diffraction, absorption, polarization, and scattering. On the other hand, data communication through power cables is mainly affected by noise, signal attenuation associated with the increase of frequency and distance, multipath propagation, and impedance mismatching along the path (electric power grid) [4–6, 31–

34]. Furthermore, cable splicing and splitting, as well as the aging, alter its impedance. The amount of load over time also varies and the noise generated by switched power supplies and compact fluorescent lamps, among other loads, can produce high power noise on the range of frequencies used by PLC technology. There will always be favorable and unfavorable factors to support PLC and wireless communication, but, in fact, they both have something in common: they do not need a new infrastructure for the data communication path to be built.

The environment in which the data communication infrastructure is immersed can highlight specific characteristics of wireless or PLC technologies. For example, a wireless AMI deployment in a building environment has some particularities. The usual situation is that the floors and walls are dense obstructions for wireless communication and attenuate the wireless signal strongly. An alternative in some cases is the elevator pathway, which can help with the signal range performance.

In order to enhance indoor environment for wireless propagation, frequency-selective surface (FSS) has been investigated over the last 40 years, as such scenario is an important data traffic source and the obstructions impact also in the battery lifetime of devices that require such type of power supply [35]. Modifications on wall materials aiming indoor wireless signal strength enhancement by means of smart bricks or external dry-wall modules are discussed in [36].

On the other hand, PLC technology is not affected by obstructions. Moreover, the outdoor and in-home LV electric power grids capillarity is an useful characteristic that such technology can exploit. However, modifications in the distribution topology will affect the PLC systems and can derail an existing and reliable data communication path.

### 2.3 SECURITY ASPECTS

Security violation in SG and IoT systems can lead not only to economic losses [37], but also induce in serious risk to life when the target is IoT devices such as connected medical equipment used for monitoring purposes. The data from an IoT set will consistently be handled by established and mature information technology systems; however, battery-operated IoT gadgets have constrained computing capacity due to their low dimension requirements, energy consumption, and memory storage capacity, which harshly affects the security features that can be implemented [38]. In order to overcome such limitations, IoT devices can make use of lightweight cryptography algorithm [39, 40]. Alternatively, physical layer authentication approach can alleviate the computing requirements for low-power IoT devices and still keep authentication security active [39].

SG and IoT security analysis can be figured in an architectural approach. In [41], it was presented a concise security attack classification for such purpose, splitting the

security inspection and making it to coincide with the structure of an IoT system, which at the same time simplifies the process and focuses on the specific threat of each segment:

- Physical attacks are related to hardware components and direct interaction with the target device. Mechanical manipulation, tampering, and unauthorized firmware change are related situations for this type of attack.
- Network attacks make use of eavesdropping (sniff out the confidential information), data traffic interference in order to access restricted data, gain system access or even prevent the system from working (denial of service).
- Software attacks explore vulnerabilities by using virus programs, Trojan horses, and spyware scripts in order to manipulate system data, steal information or deteriorate system operation.
- Encryption attacks use different techniques to disturb encoding design with the purpose of obtaining the encryption key.

The data communication infrastructure enables intelligent, reachable, and controllable devices on the field. But there is also a security risk in terms of privacy of information from smart meter (SM), metering theft, and external cyber-attacks [42].

There is a legal concern about the information that an SM is able to provide mainly because of the energy consumption profiling capability. In [43], it was demonstrated that by means of statistical methods and analyses of the data from an SM, it is possible to get electricity usage pattern of a specific consumer. From the technical point of view of the electric utilities, this is an advantage that makes possible to compare the total usage registered by the entire LV electric power circuit with the hourly (or even lower register rate) load profile of the consumers. This ability makes possible for the electric utility to find out an electricity theft. This information, that can potentially be hacked, is likewise valuable to specific market industries such as insurance companies or media and entertainment companies. There is also another negative side for the electric utilities about SM hacking: the meter tamper.

In 2010, an FBI report alerted about SM hacker in Puerto Rico, changing the SM settings for recording less power consumption [44]. In 2014, the government of Malta revealed a sophisticated hacking in SM making them to register less energy than what is being consumed [45].

Besides the SM itself, the data communication path is also another possible entrance door for hackers to access both the SM parameters and the registered consumer information, so the security is very important as a protection against illegal and inappropriate log. There are several techniques that can be used to encrypt the data, but the

system complexity can be increased and affect the performance, therefore a reasonable trade-off must be considered for implementation purposes.

The SM remote communication can also help to detect illegal load consumption reduction by tampering the current and voltage connection part that is outside of the SM, as shown in [46]. This tamper was found in Brazil, where large-scale consumers are equipped with time-of-use (TOU) solid state current transformer (CT) meters. This type of connection requires a tests switch (also called as switch block), which is a special gadget that is used to disconnect CT-meter without interrupting the electricity flow to the consumer. The detected tamper consisted of built-in small relays, remote-controlling the connection and disconnection of the current portion of the tests switch and therefore preventing these currents to be registered by the meter. Electric utilities recognized that the meter load profile collected remotely was inconsistent and triggered a more detailed investigation that made possible the tamper detection.

More recently, SG has been linked as part of IoT with the implication of alleviating the number of data communication protocols and assisting on the handle of a big amount of data [47]. But along with this new concept, there is also more security concern, as the number of devices and networked things that are potentially vulnerable is extensive. A large portion of these devices (usually designed targeting a minimal cost and that now are having the opportunity to be part of a wider network) was not developed to ensure the needed security level on data privacy and unauthorized control access [48, 49].

It is true that IoT and SG implementations that are Internet-connected have higher chances to suffer cyber-attacks, but even classified local area network (C-LAN) are not free of such treats. In 2010, a silent but very powerful computer worm named Stuxnet was detected in a dozen of industrial sites in Iran [50], including an uranium-enrichment plant. The infection mechanism uses Windows-based PC configuration software that is used to program industrial control systems causing the logic controllers to perform a slightly different script than the original set. At the uranium-enrichment plant, this threat caused the centrifuges to fast-spinning and consequently to be damaged.

## 2.4 IOT ROLE IN SG DOMAIN

Each device or sensor in a stand-alone situation will perform limited and only pre-configured tasks. But when they are connected, making part of a wide and complex organization (cyber-physical system), the possibilities are shifted to a new level. In the context of SG, these possibilities are related to more efficiency, reliability and sustainability [51]. When devices and sensors are connected, the system management can perform analysis and use the received data in an intelligent decision transaction that can feedback to end-device an “educated-command”, controlling or adapting the system to behave or act in a more appropriate and adjusted manner.

In [51], it is shown that the complete realization of the SG concept depends on a data communication infrastructure that is responsible for connecting all elements of the electric power grid besides transmitting control information and monitoring data so that the system managers can handle the devices and sensors. Moreover, it also shows that SG depends on information technologies and applications. Information technologies are mainly responsible for processing and analyzing the information coming from different devices and also providing interoperability between layers and devices of the SG, while applications are responsible for improving the management, control, and automation techniques.

Information and communication technologies perform an important role in a SG domain and, as a consequence, their projects need considerable attention from designers and engineers. In this context, IoT resides as the chain link, realizing the data from each required sensor and device to be as granular as needed and also improving the required interoperability when using multiple data communication protocols. For example, [52] describes IoT as an enabling architecture for the development of applications, in which high degrees of autonomy, connectivity and interoperability are required.

Regarding communication infrastructure, IoT and SG can be considered complementary concepts. The idea is to highlight the win-win situation for both concepts when they are part of a whole solution. SG is enhanced in terms of new possibilities, as well as IoT can benefit from a data communication backbone infrastructure that is inherent of a SG implementation. On the other hand, with respect to information technologies, IoT will foster the development of the Internet Protocol to make objects addressable and reachable from everywhere [52], which can benefit the application of the SG concept.

The combination of IoT and SG leverages deployment options and project expansion for alternative configurations. Such applications can be found in implementations like B&IA (commercial buildings, offices, factories, and hospitals), Retail Environment (stores, banks, restaurants), and Street Light automation. For instance, [53] discussed a system design of IoT in a residential real-world environment aiming to control and monitor the use of energy by consumers. In addition, [54] proposed an algorithm, supported by IoT applications, for real-time detections of network attacks that aim to corrupt terminal nodes or “hijack” the communication channel in SG domains. Another example can be found in [55], in which an investigation on a narrowband IoT technology applied to Machine-to-Machine applications is made and it is shown that the narrowband data communication technology associated with IoT is a good solution for SG applications. In terms of technical data communication models [56], IoT can also play an important role in applications such as Vehicular Automation, Surveillance & Security Systems, Mining, Construction, among others.

The small amount of data traffic for signaling, open/close commands, and registers

reading also fits the initial prerogative for using wireless or PLC, as discussed previously. An appropriate choice for implementing it is to keep the data communication cost as low as possible. The data rate, in this case, is not a critical target and the data communication addressed here should be delay-tolerant and reliable.

## 2.5 HYBRID DATA COMMUNICATION SYSTEMS

The target of a more robust data communication technology can be achieved by joining wireless and PLC in a cooperative way in which both can assist each other, at the same time, to ensure reliability in the data communication network. In fact, the idea of a hybrid system is not recent. In 2005, a discussion on this subject took place [7], but wireless and PLC were considered to be working alone, each one in a section of the data communication link because interconnection is an important issue for reliability and coverage. The concept to perform a multiple and simultaneous data communication through PLC and wireless parallel channels transforms the original sender-receiver dilemma in a collaborative approach. Such situation moves the main issue of a data communication system which is originally designed to reach the receiver with a restrictive link into a new situation where the system can focus on the quality of the delivered data to the receiver.

There is also another concept for hybrid in which a wireless instrument or also a PLC device is able to connect wirelessly to a PLC device through the signal irradiated from the unshielded power line, as discussed in [57, 58]. It is important to highlight that the present work does not consider the context of the irradiated PLC signal because wireless and PLC are not working parallelly in a collaborative way but as the cascade of PLC and wireless channels.

Regarding the parallel hybrid scheme, as depicted in Fig. 3, the main advantage is reliability gains due to the availability of two communication media with relevant diversity. Observe that this gains can be exchanged with the increase of end-to-end capacity [59]. Other benefits of using hybrid schemes are the reduced need for infrastructure deployment due to the available electric power grids for PLC, which may cause reduced costs of the overall communication system [51] and increase the communication coverage. On the other hand, the main disadvantage is related to complex synchronization process between the hybrid nodes of the system, which is a key feature to ensure the gains of the hybrid data communication system.

Overall, the implementation of a hybrid PLC/wireless data communication system is dependent on the configuration of the low-voltage (LV) outdoor electric power grids and the environment in which it is immersed. Moreover, the combination of IoT and SG technologies, deployment options and project expansions for alternative configurations can be leveraged, while the cost of data communication is kept as low as possible.

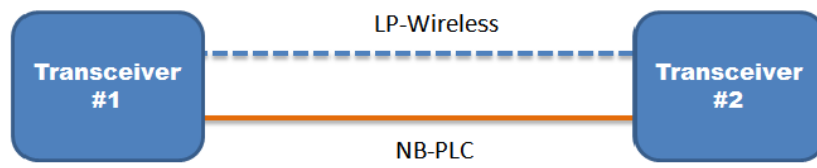


Figure 3: The Hybrid PLC/Wireless system approach.

### 3 MULTIUSER BASEBAND ORTHOGONAL CHIRP DIVISION MULTIPLEXING

The search for reliable and/or spectral efficient PLC systems [60] drove technical solutions to the use of multicarrier schemes at the physical layer level [61] because this scheme divides the transmission bandwidth into narrowband subchannels. As a result, the equalization of frequency selective channels, which is a typical feature of PLC systems, can be easily handled. The literature shows that the OFDM scheme is the preferred choice for multicarrier-based PLC systems [62, 63] mainly due to its low computational complexity. In fact, the use of Fast Fourier Transform for implementing the OFDM scheme and the easiness to successfully perform the frequency-domain equalization of channel impulse response (CIR) with one-tap per subchannel when the OFDM symbol is correctly designed to guarantee that the channel convolutional matrix is circulant are very important motivations for the widespread use of the OFDM scheme in PLC systems. Despite some technical texts do not mention it explicitly, it is worth stating that PLC systems based on multicarrier schemes operate in the baseband. This way, the Hermitian symmetric OFDM (HS-OFDM) scheme, also known as discrete multitone modulation fits the requirements for this scenario [61, 64].

Currently, the data needs and demands related to SG and IoT bring attention to new drivers for the telecommunication field, such as the large number of nodes and the use of small size data packets and headers [65–67]. It is worth to emphasize that the large number of nodes must share the available and finite frequency bandwidth to have their data communication demands fulfilled, something that could be addressed with the use of multiuser schemes [68–70]. Therefore the use of multiuser-based communication schemes [71–75], such as MC-CDMA is an interesting topic for carrying out research for SG and IoT applications as it allows us to simultaneously transmit data to several users [76–79]. The use of the OFDM scheme as the multicarrier component of MC-CDMA has been widely investigated [80–84] and very interesting results have been reported so far in the literature, see [85, 86] and references therein.

Recently, researches on design of data communication systems capable of maximizing the use of the available bandwidth and minimizing the impairments related to transmit data by using wireless and/or optical fiber systems have led to the introduction of the spread spectrum technique based on chirp signals [87, 88] and, more recently, to the introduction of the OCDM scheme [89]. The OCDM scheme uses the DF<sub>n</sub>T in an analogous fashion as the DFT. However, each OCDM symbol in the Fresnel domain is frequency-spread linearly over a set of orthogonal chirps (DF<sub>n</sub>T matrix) before being transmitted in the time-domain. Previous works [89–91] showed that the OCDM scheme can surpass the performance of the OFDM scheme for wireless, optical fiber, and underwater acoustic media.

The use of the OCDM scheme in PLC systems is not straightforward, since, despite being an integral transform [92, 93], the DF<sub>n</sub>T does not share the same Hermitian symmetric property as the DFT and, as a consequence, the OCDM symbol is a complex signal. This means that it can not be transmitted through baseband channels [61, 94]. In other words, the analysis of possible advantages that the OCDM scheme may offer to PLC systems depends upon the design of versions of the OCDM scheme that can allow the data communication through baseband channels. Additionally, the introduction of the MCp-CDMA scheme, which is the combination of CDMA and OCDM, is interesting to analyze what kind of gains can be obtained by combining OCDM together with the CDMA scheme when PLC systems need to fulfill the needs and demands of large number of nodes that makes use of electric power grids for data communication purposes. In this context, this chapter discusses the use of the OCDM scheme in PLC systems for narrow-band data communication through baseband channels that are used for assisting data exchanges related to SG and IoT applications. Also, it focuses on the introduction of the MCp-CDMA scheme for dealing with multiuser data communication associated with the aforementioned applications.

This chapter is organized as follows: Section 3.1 introduces the MCp-CDMA scheme and its concept, addressing the challenge of transmitting data in a multiuser PLC scenario using the DF<sub>n</sub>T transform. Section 3.2 discusses the DF<sub>n</sub>T and its relation with the DFT. Section 3.3 describes four distinct procedures types for generating baseband transmission employing OCDM scheme. In Section 3.4, numerical results obtained from MCp-CDMA scheme are analyzed.

### 3.1 PROBLEM STATEMENT

The scenario portrayed in this chapter involves the downlink of a data communication system based on the MCp-CDMA scheme that transmits data through a bandwidth equal to  $B$ . In this respect, such environment is represented by the block diagram shown in Fig. 4. It is worth stating that this block diagram is similar to the one of the MC-CDMA scheme. As a matter of fact, the only difference is the use of the DF<sub>n</sub>T instead of the DFT. The use of the DF<sub>n</sub>T means that the data is orthogonally spread over the available frequency bandwidth, which is conceptually different from orthogonally spreading data over narrowband subchannels as done by the DFT. For this reason, such scheme is named MCp-CDMA.

According to Fig. 4, the  $i$ -th inputted symbol (originated from a digital modulator) that will be transmitted through the electric power grids to deliver data to the  $j$ -th user is assigned as  $\dot{x}_{ij} \in \mathbb{C}$ , where the dot sign is used to indicate transformed domain (Fresnel domain, in the present case) and  $j = 1, \dots, J$  refers to the  $j$ -th user. In sequel, the inputted symbol is spread using the direct sequence code division multiple access

(DS-CDMA) scheme [95, 96], forming, in a first step, a spread OCDM symbol, whose vectorial representation is expressed as

$$\dot{\mathbf{x}}_{ij,U} = \mathbf{U}\dot{x}_{ij}, \quad (3.1)$$

where  $\dot{\mathbf{x}}_{ij,U} \in \mathbb{C}^{N \times 1}$  and  $\mathbf{U} \in \mathbb{R}^{N \times 1}$  is the spreading vector composed by ones. Observe that  $N$  is associated with the DS-CDMA spreading factor ( $S_F$ ) which is the length of the spread OCDM symbol. The next step is the encoding process, whereat  $\dot{\mathbf{x}}_{ij,U}$  is multiplied by a vector that defines the encoding code, originating the CDMA chips, which is associated with the  $j$ -th user. In this regard, let  $\mathbf{k}_j \in \{-1, +1\}^{N \times 1}$  be the encoding vector associated with the  $j$ -th user, then

$$\dot{\mathbf{x}}_{ij} = \mathbf{diag}\{\mathbf{k}_j\}\dot{\mathbf{x}}_{ij,U}, \quad (3.2)$$

with  $\mathbf{diag}\{\cdot\}$  denoting a diagonal matrix. For the sake of simplicity, we will name  $\dot{\mathbf{x}}_{ij}$  as the  $i$ -th OCDM symbol associated with the  $j$ -th user. In such situation, one can interpret the spreading/encoding process as an encryption engine, whose key for getting back the original inputted symbol is precisely the used encoding code. If a node transmits data to  $J$  users by applying the MCp-CDMA scheme, then the  $i$ -th vector applied to the inverse DFNT, which is similar to what is performed in the MC-CDMA scheme with the use of the inverse DFT, is given by

$$\dot{\mathbf{x}}_i = \sum_{j=1}^J \dot{\mathbf{x}}_{ij}. \quad (3.3)$$

In the next step, the vector  $\dot{\mathbf{x}}_i$ , which is in the Fresnel domain, is submitted to the DFNT and also to the addition of cyclic prefix. As a result, the vectorial representation of the MCp-CDMA symbol that is transmitted in the time-domain is given by

$$\begin{aligned} \mathbf{s}_i &= \mathcal{P}(\dot{\mathbf{x}}_i) \\ &= \begin{bmatrix} \mathbf{0}_{L_{cp} \times (N-L_{cp})} & \mathbf{I}_{L_{cp}} \\ & \mathbf{I}_N \end{bmatrix} \Phi_N^\dagger \dot{\mathbf{x}}_i \\ &= \begin{bmatrix} \mathbf{0}_{L_{cp} \times (N-L_{cp})} & \mathbf{I}_{L_{cp}} \\ & \mathbf{I}_N \end{bmatrix} \Phi_N^\dagger \sum_{j=1}^J \dot{\mathbf{x}}_{ij} \\ &= \sum_{j=1}^J \begin{bmatrix} \mathbf{0}_{L_{cp} \times (N-L_{cp})} & \mathbf{I}_{L_{cp}} \\ & \mathbf{I}_N \end{bmatrix} \Phi_N^\dagger \dot{\mathbf{x}}_{ij} \\ &= \sum_{j=1}^J \mathbf{s}_{ij}, \end{aligned} \quad (3.4)$$

in which

$$\mathbf{s}_{ij} = \begin{bmatrix} \mathbf{0}_{L_{cp} \times (N-L_{cp})} & \mathbf{I}_{L_{cp}} \\ & \mathbf{I}_N \end{bmatrix} \Phi_N^\dagger \dot{\mathbf{x}}_{ij}, \quad (3.5)$$

$\mathbf{I}_a$  denotes an  $a$ -size square identity matrix, and  $\mathbf{0}_{b \times c}$  is a zero matrix of size  $b \times c$ . Also,  $\Phi_N^\dagger$  refers to the  $N \times N$  size inverse matrix associated with the DFNT. Observe that

$\mathcal{P}(\cdot)$  is the transmitter function that represents, in a condensed form, the OCDM scheme, including the Fresnel transform and the cyclic prefix (CP) insertion. At this point, the vectorial time-domain representation of the  $i$ -th MCp-CDMA symbol is ready to reach the parallel/serial (P/S) converter that will serialize the consecutive MCp-CDMA symbols, which are yielded by the node. The discrete-time representation of the sequence that is constituted by consecutive MCp-CDMA symbols is given as

$$s[n] = \sum_{i=-\infty}^{\infty} \sum_{q=0}^{N+L_{cp}-1} s_{i,q} \delta[n - i(N + L_{cp}) - q], \quad (3.6)$$

in which  $s_{i,q}$  is the  $q$ -th element of the vector  $\mathbf{s}_i$ .

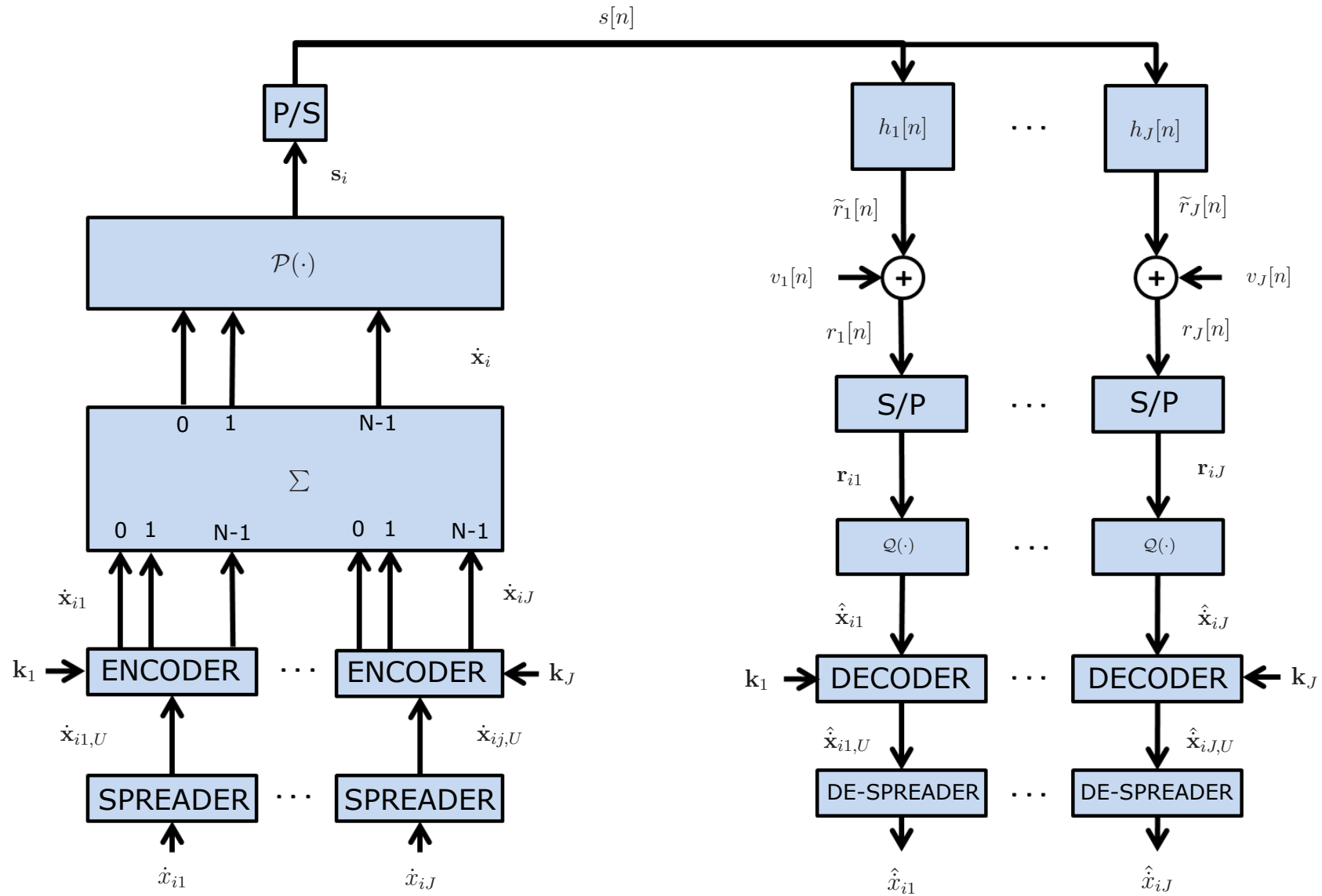


Figure 4: The downlink of the MCp-CDMA scheme for a PLC system.

The PLC channels have time varying nature that can be modeled as linear periodically time-variant (LPTV) [97]. However, if the coherence time of PLC channels,  $T_c$ , is much longer than the OCDM symbol time duration,  $T_{OCDM} = (N + L_{cp})T_s$ , in which  $T_s$  is the sampling period (i.e.,  $T_c \gg T_{OCDM}$ ), then one can assume that PLC channels are linear and time invariant (LTI) within an OCDM symbol time duration. In this sense, let  $\{h_j[n]\}_{n=0}^{L_j-1}$  be the discrete-time representation of the CIR of an LTI PLC channel associated with the data communication between the node and the  $j$ -th user, then the discrete-time representation of the signal at the input of the  $j$ -th user is expressed as

$$\begin{aligned}
r_j[n] &= \tilde{r}_j[n] + v_j[n] \\
&= h_j[n] * s[n] + v_j[n] \\
&= \sum_{l=0}^{L_j-1} h_j[l]s[n-l] + v_j[n] \\
&= \sum_{l=0}^{L_j-1} h_j[l] \sum_{i=-\infty}^{\infty} \sum_{q=0}^{N+L_{cp}-1} s_{i,q} \delta[n-l-i(N+L_{cp})-q] + v_j[n] \\
&= \sum_{i=-\infty}^{\infty} \sum_{q=0}^{N+L_{cp}-1} s_{i,q} \sum_{l=0}^{L_j-1} h_j[l] \delta[n-l-i(N+L_{cp})-q] + v_j[n] \\
&= \sum_{i=-\infty}^{\infty} \sum_{q=0}^{N+L_{cp}-1} s_{i,q} h_j[n-i(N+L_{cp})-q] + v_j[n]
\end{aligned} \tag{3.7}$$

where  $*$  denotes linear convolution operator,  $\tilde{r}_j[n]$  is the channel output free of noise, and  $v_j[n]$  is the PLC additive noise, which is modeled as ABGN with memory [98]. This noise model is orchestrated by a Bernoulli distribution with probability  $p$  for a low-power noise (background noise) and probability  $(1-p)$  for a high power noise (impulsive noise). The background noise component is formed by a sequence of Gaussian random variables with zero mean and variance  $\sigma_0^2$ . On the other hand, the impulsive noise component is constituted by Gaussian random variables with zero mean and variance  $\sigma_1^2 = K\sigma_0^2$ , where  $K \in \mathbb{N} | K > 1$  is the impulsive noise gain. Furthermore, [98] state the parameter named noise memory length  $L_m$  (for both low and high power portions) to indicate the number of samples that such state (low or high power Gaussian noise) remains.

Assuming that the received signal  $r_j[n]$  passes through a serial/parallel (S/P) converter, the adoption of the perfect symbol synchronization and the fact that  $L_{cp} \leq L_j - 1$ , then for each transmitted MCp-CDMA symbol, the time-domain vectorial representation of each of them at the output of the PLC channel is expressed as

$$\begin{aligned}
\mathbf{r}_{ij} &= \tilde{\mathbf{r}}_{ij} + \mathbf{v}_{rij} \\
&= \mathbf{C}_j \mathbf{s}_i + \mathbf{v}_{rij},
\end{aligned} \tag{3.8}$$

where  $\mathbf{r}_{ij}$  is a vector constituted by samples of the signal described in (3.7),  $\mathbf{C}_j \in \mathbb{R}^{(N+L_{cp}) \times N}$  is the channel convolutional matrix associated with the  $j$ -th user. Observe

that such convolutional matrix is related to the vector  $\mathbf{h}_j = [h[0] h[1] \cdots h[L_j - 1]]^T$ , which is the vectorial representation of the PLC CIR. In addition,  $\mathbf{v}_{rij}$  is the vector constituted by consecutive samples of the PLC additive noise at the output of the PLC channel, associated with the  $j$ -th user and the  $i$ -th MCp-CDMA received symbol. The removal of the cyclic prefix, that occurs inside  $\mathcal{Q}(\cdot)$ , results in

$$\begin{aligned} \mathbf{y}_{ij} &= \tilde{\mathbf{y}}_{ij} + \mathbf{v}_{ij} \\ &= \begin{bmatrix} \mathbf{0}_{N \times L_{cp}} & \mathbf{I}_N \end{bmatrix} \mathbf{r}_{ij}. \end{aligned} \quad (3.9)$$

Note that  $\mathbf{y}_{ij}$  is the time-domain vectorial representation of the signal at the output of the block responsible for removing the cyclic prefix, which is mathematically performed as described in Eq. (3.9). Alternatively, the vector  $\mathbf{y}_{ij}$  can be expressed as

$$\mathbf{y}_{ij} = \mathbf{C}_{h_{je}} \mathbf{s}_i + \mathbf{v}_{ij}, \quad (3.10)$$

in which  $\mathbf{C}_{h_{je}}$  is the circulant channel convolutional matrix associated with  $\mathbf{h}_{je} = [h]_j[0] \dots h_j[L_j-1] 0 \dots 0]^T$  and  $\mathbf{v}_{ij} \in \mathbb{C}^{N \times 1}$  is the time-domain vectorial representation of the additive noise. By transforming  $\mathbf{y}_{ij}$  to the frequency-domain, one can obtain

$$\begin{aligned} \mathbf{Y}_{ij} &= \mathbf{F}_N \mathbf{y}_{ij} \\ &= \mathbf{F}_N \mathbf{C}_{h_{je}} \mathbf{s}_i + \mathbf{F}_N \mathbf{v}_{ij} \\ &= \mathbf{F}_N \mathbf{C}_{h_{je}} \mathbf{\Phi}_N^\dagger \dot{\mathbf{x}}_i + \mathbf{F}_N \mathbf{v}_{ij} \\ &= \mathbf{F}_N \mathbf{C}_{h_{je}} \mathbf{F}_N^\dagger \mathbf{F}_N \mathbf{\Phi}_N^\dagger \mathbf{F}_N^\dagger \mathbf{F}_N \dot{\mathbf{x}}_i + \mathbf{F}_N \mathbf{v}_{ij} \\ &= \mathbf{\Lambda}_{h_{je}} \mathbf{\Gamma}^\dagger \mathbf{F}_N \dot{\mathbf{x}}_i + \mathbf{V}_{ij}, \end{aligned} \quad (3.11)$$

with  $\mathbf{F}_N = \mathbf{W}/\sqrt{N}$  denoting an  $N$ -size normalized DFT matrix,  $\mathbf{F}_N^\dagger \mathbf{F}_N = \mathbf{I}_N$ ,  $\mathbf{\Lambda}_{h_{je}} = \mathbf{F}_N \mathbf{C}_{h_{je}} \mathbf{F}_N^\dagger$  is a diagonal matrix constituted by the coefficients of the vector  $\mathbf{H}_{je} = \mathbf{F}_N \mathbf{h}_{je}$ , which represents the channel frequency response (CFR) of the augmented version of  $\mathbf{h}_j$  and  $\mathbf{\Gamma}^\dagger = \mathbf{F}_N \mathbf{\Phi}_N^\dagger \mathbf{F}_N^\dagger$ . Finally,

$$\begin{aligned} \hat{\mathbf{x}}_{ij} &= \mathbf{G} \mathbf{\Gamma} \mathbf{Y}_{ij} \\ &= \mathbf{G} \mathbf{\Lambda}_{h_{je}} \mathbf{F}_N \dot{\mathbf{x}}_i + \mathbf{G} \mathbf{V}_{ij}, \end{aligned} \quad (3.12)$$

where  $\mathbf{G}$  denotes a matrix that performs the frequency-domain equalizer (FDE). Following [89], one can make use of the zero forcing (ZF) criterion to implement FDE and, as a consequence,

$$\hat{\mathbf{x}}_{ij} = \dot{\mathbf{x}}_i + \mathbf{F}_N^\dagger \mathbf{\Lambda}_{h_{je}}^{-1} \mathbf{\Gamma} \mathbf{V}_{ij}, \quad (3.13)$$

because  $\mathbf{G} = \mathbf{F}_N^\dagger \mathbf{\Lambda}_{h_{je}}^{-1}$  is the product between the inverse of the normalized DFT matrix and the diagonal matrix constituted by the coefficients of the FDE based on the ZF criterion.

Similar to the transmitter, all details described above can be represented by

$$\hat{\mathbf{x}}_{ij} = \mathcal{Q}(\mathbf{r}_{ij}), \quad (3.14)$$

where  $\mathcal{Q}(\cdot)$  synthesizes the receiver side of the OCDM scheme and  $\hat{\mathbf{x}}_{ij} \in \mathbb{C}^{N \times 1}$  (that is, in the Fresnel domain) is the estimate of  $\mathbf{x}_i$  received by the  $j$ -th user. In an analogous fashion to  $\mathcal{P}(\cdot)$ , the function  $\mathcal{Q}(\cdot)$  expresses each multichirp symbol reception process, reverting the operational elements used in the transmission, so that  $\mathcal{Q}(\mathbf{s}_i) = \mathbf{x}_i$ . Consequently, an estimate of the transmitted MCp-CDMA symbol,  $\hat{x}_{ij}$ , can be obtained by reverting the DS-CDMA encoding and spreading processes that were performed at the transmitter side. In other words,

$$\hat{\mathbf{x}}_{ij,U} = \mathbf{diag}\{\mathbf{k}_j\}\hat{\mathbf{x}}_{ij}, \quad (3.15)$$

where  $\hat{\mathbf{x}}_{ij,U} \in \mathbb{C}^{N \times 1}$  is an estimate of the spread OCDM symbol. Finally, the estimated  $i$ -th symbol by the  $j$ -th user is given by

$$\hat{x}_{ij} = \frac{1}{N} \sum_{l=0}^{N-1} \hat{x}_{ijl,U}, \quad (3.16)$$

where  $\hat{x}_{ijl,U}$  denotes the  $l$ -th element of the vector  $\hat{\mathbf{x}}_{ij,U}$ .

The aforementioned description of the MCp-CDMA scheme was deduced based on the use of the OCDM scheme introduced in [89]. A drawback associated with this scheme refers to the fact it only applies to passband data communication because the time-domain representation of the transmitted signal is complex. In order to overcome this limitation for performing data communication through electric power grids, which is supposed to be carried out through baseband channels, the following section introduces different implementations of the OCDM scheme that allow us to obtain real time-domain signals. Observe that the OCDM scheme could be directly used for providing data communication through PLC channels by performing the modulation of in-phase (real) and quadrature (imaginary) components of the discrete-time transmitted signals but it could require a much more complex hardware. At this point, it is important to emphasize that the DF<sub>n</sub>T, which is used in the OCDM scheme, does not share the same Hermitian symmetric property as the DFT. Therefore,  $\mathcal{P}(\cdot)$  and  $\mathcal{Q}(\cdot)$  need to be designed to allow baseband data communication.

## 3.2 DISCRETE FRESNEL TRANSFORM

Fresnel transform, which describes mathematically the near-field diffraction, is perhaps not well-known beyond optics domain because it has greater complexity compared to the Fourier Transform. But, in fact, it is an interesting and powerful integral transform [99]. The discrete-time version of the Fresnel transform, the DF<sub>n</sub>T, describes the coefficients of the Talbot image (also known as self-image) which is the image formed from a periodic diffraction grating repeated at regular distances away from the grating plane [92]. According to the literature, the DF<sub>n</sub>T is a trigonometric transform of chirped phases and owns a very close relationship with the chirp Z-transform (CZT) and

the Zadoff-Chu sequence [89]. In fact, CZT is a special case of the DFNT, and the root Zadoff-Chu sequence corresponds to the eigen-values of the DFNT [89].

The matrices used for performing the discrete Fresnel transform and its inverse depend upon the length of the vector  $\mathbf{x}_j$  being even or odd [92], which may be generically denoted by  $M \in \mathbb{N} | M > 0$ . In this thesis, only even  $M$  values are considered as DFNT matrices are constituted by DFT matrices, which are efficiently implemented when their size is a power of 2. According to [92], the DFNT for even  $M$  values can be represented by  $\Phi_M \in \mathbb{C}^{M \times M}$ , in which each element of this matrix is the Talbot coefficient given by

$$\Phi_M[m, n] = \frac{e^{-j\pi/4}}{\sqrt{M}} e^{(j\pi/M)(m-n)^2}, \quad (3.17)$$

where  $\Phi_M[m, n]$  is the element of  $\Phi_M$  in the  $m$ -th line and  $n$ -th column. Also,  $m$  and  $n$  are respectively named sample and sub-chirp indexes. Expanding a generic coefficient of the DFNT matrix, one obtains

$$\Phi_M[m, n] = \frac{1}{\sqrt{M}} e^{-j\pi/4} e^{j\pi m^2/M} e^{-2j\pi mn/M} e^{j\pi n^2/M}. \quad (3.18)$$

In other words, the DFNT matrix consists of the well-known DFT matrix pre- and post-multiplied by specific matrices. According to [89], the DFNT matrix can be rewritten as

$$\Phi_M = \frac{1}{\sqrt{M}} \Theta_1 \mathbf{W} \Theta_2, \quad (3.19)$$

where  $\mathbf{W} \in \mathbb{C}^{M \times M}$  is the DFT matrix;  $\Theta_1 = \mathbf{diag}\{\Theta_{1,0}; \Theta_{1,1}; \dots; \Theta_{1,M}\}$  with  $\Theta_{1,m} = e^{-j\pi/4} e^{j\pi m^2/M}$ ;  $\Theta_2 = \mathbf{diag}\{\Theta_{2,0}; \Theta_{2,1}; \dots; \Theta_{2,M}\}$  with  $\Theta_{2,n} = e^{j\pi n^2/M}$ ;  $\mathbf{diag}\{\cdot\}$  is a diagonal matrix whose entries are given by the vector argument. Moreover, the DFNT matrix is unitary, i.e.,  $\Phi_M^\dagger \Phi_M = \mathbf{I}_M$ , in which  $\mathbf{I}_M$  is the identity matrix of size  $M$  and  $\dagger$  represents the Hermitian operator, therefore, the DFNT matrix is invertible and its inverse is  $\Phi_M^\dagger$ .

It is interesting to note that  $\Phi_M$  is a symmetrical matrix, i.e.,  $\Phi_M(m, n) = \Phi_M(n, m)$ . Another interesting aspect of the DFNT transform is its circular convolution property, i.e., the DFNT of the circular convolution between two finite-length sequences equals the convolution of one of them with the DFNT of the other. It is worth to mention that multiplying a signal by the DFNT matrix does not affect its amplitude, but rather shifts its phase.

### 3.3 THE OCDM FOR BASEBAND DATA COMMUNICATION

In this section, a number of distinct ways of implementing  $\mathcal{P}(\cdot)$  and  $\mathcal{Q}(\cdot)$  for the OCDM scheme carry out baseband data communication are portrayed. In this context, let us assume that an OCDM symbol denoted by  $\mathbf{x}_i$  belongs to the Fresnel domain. The purpose is to come up with  $\mathcal{P}(\cdot)$  and  $\mathcal{Q}(\cdot)$  such that  $\mathbf{x}_i = \mathcal{P}(\dot{\mathbf{x}}_i) \in \mathbb{R}^{L \times 1}$  and, as a

consequence,  $\hat{\mathbf{x}}_i = \mathcal{Q}(\mathbf{x}_i)$ . Observe that  $L \in \mathbb{N} | L \leq 2N$  is assumed to ensure that both OCDM and HS-OFDM schemes have the same length in terms of number of samples in the discrete-time domain. Consequently, the discrete sequence of the OCDM symbols can be transmitted through the baseband channels, which characterize data communication through electric power grids.

In this regard, four types of the OCDM scheme for baseband communication are introduced. Each type exploit a different approach that is based on a specific feature of the DF $\nu$ nT transform or on a mapping function that yields a real valued vector for being applied to the inverse DF $\nu$ nT transform.

### 3.3.1 The type-I OCDM scheme

Fig. 5 shows the block diagram of a baseband data communication based on the OCDM scheme which is referenced here as type-I OCDM. More specifically, Fig. 5-a and Fig. 5-b show  $\mathcal{P}(\cdot)$  and  $\mathcal{Q}(\cdot)$ , respectively.

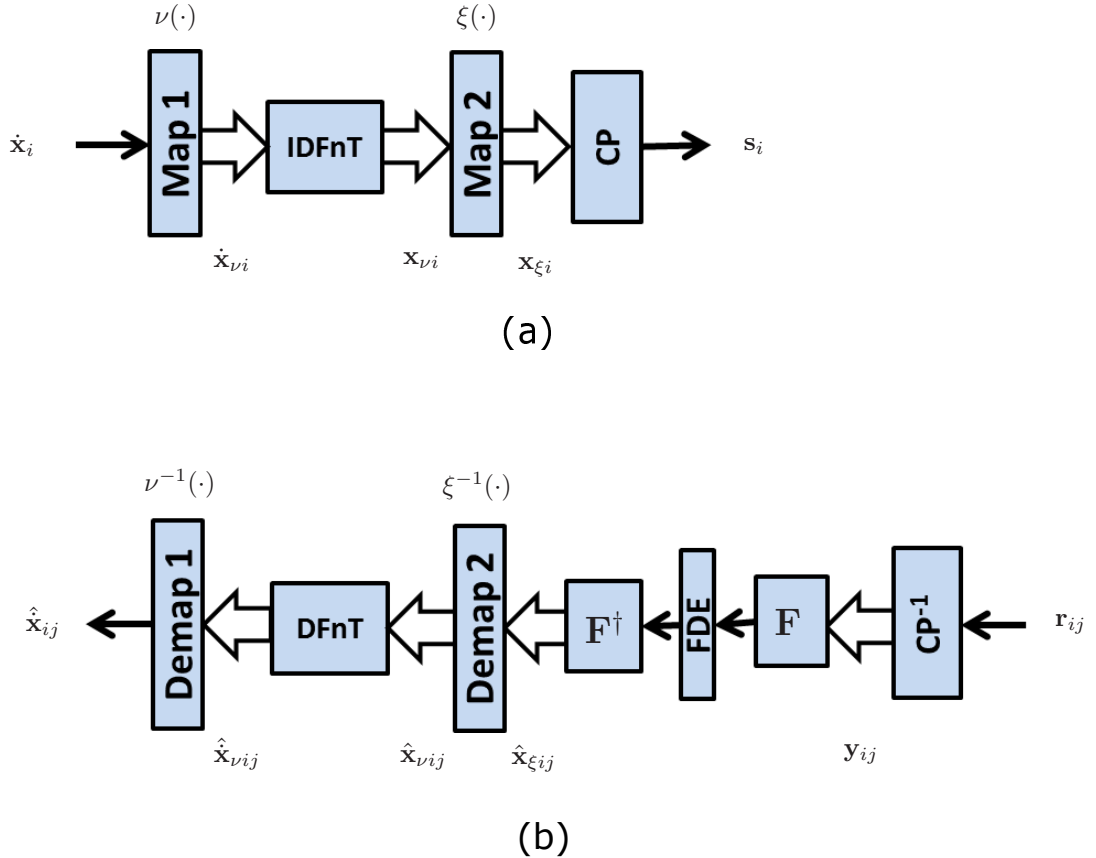


Figure 5: The block diagram of type-I OCDM: (a) represents  $\mathcal{P}(\cdot)$  and (b) represents  $\mathcal{Q}(\cdot)$ .

Based on Fig. 5-a, the mapping function  $\nu(\cdot)$  will rearrange the  $i$ -th MCp-CDMA

symbol  $\dot{\mathbf{x}}_i$  into a  $2N$ -length mirrored vector. Thereby,  $\dot{\mathbf{x}}_{\nu i} = \nu(\dot{\mathbf{x}}_i) \in \mathbb{C}^{2N \times 1}$ , where

$$\dot{\mathbf{x}}_{\nu i} = \nu(\dot{\mathbf{x}}_i) = \begin{bmatrix} \mathbf{I}_N \\ \mathbf{J}_N \end{bmatrix} \dot{\mathbf{x}}_i, \quad (3.20)$$

with  $\mathbf{J}_N$  denoting the backward identity matrix of size  $N$ . It is important to highlight that  $\mathbf{x}_{\nu i}$  is composed of mirrored symmetrical values. After performing the inverse DFNT matrix, given by  $\mathbf{x}_{\nu i} = \Phi_{2N}^\dagger \dot{\mathbf{x}}_{\nu i} \in \mathbb{C}^{2N \times 1}$ , the mapping function  $\xi(\cdot)$  will ensure that the OCDM symbol is real-valued,  $\mathbf{x}_{\xi i} = \xi(\mathbf{x}_{\nu i}) \in \mathbb{R}^{2N \times 1}$ . In other words,

$$\mathbf{x}_{\xi i} = \frac{\xi(\mathbf{x}_{\nu i})}{\sqrt{2}} = \begin{bmatrix} \mathbf{I}_N & \mathbf{0}_N \\ \mathbf{0}_N & \mathbf{0}_N \end{bmatrix} \Re(\mathbf{x}_{\nu i}) + \begin{bmatrix} \mathbf{0}_N & \mathbf{0}_N \\ \mathbf{J}_N & \mathbf{0}_N \end{bmatrix} \Im(\mathbf{x}_{\nu i}), \quad (3.21)$$

in which  $\Re(\cdot)$  and  $\Im(\cdot)$  are respectively the real and imaginary parts of a complex number. After adding CP to  $\mathbf{x}_{\xi i}$ , the time-domain vectorial representation of the transmitted signal,  $\mathbf{s}_i$ , is obtained.

Graphically, the mapping functions  $\nu(\cdot)$  and  $\xi(\cdot)$  can be translated as in Fig. 6-a and Fig. 6-b, respectively. The function  $\nu(\cdot)$  maps an  $N$ -length complex symbol ( $\dot{\mathbf{x}}_i$ ) into a  $2N$ -length complex symbol ( $\nu(\dot{\mathbf{x}}_i)$ ). Notice the first and the second half of  $\nu(\cdot)$  output symbol are mirrored versions of each other. Such mirror state is kept in the inputted  $2N$ -length symbol ( $\mathbf{x}_{\nu i}$ ) to  $\xi(\cdot)$  and its output is also a  $2N$ -length symbol with its first half corresponding to the real part of the inputted symbol ( $\xi(\mathbf{x}_{\nu i})$ ) and the second half corresponding to the imaginary part of the inputted symbol.

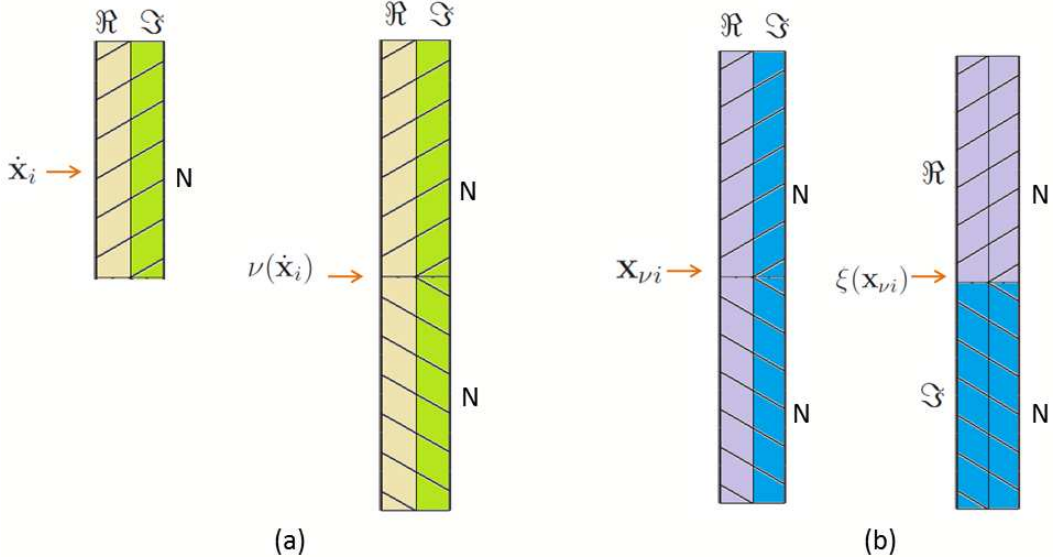


Figure 6: Graphic representation of (a) mapping function  $\nu(\cdot)$  and (b) mapping function  $\xi(\cdot)$ .

The vectorial representation of the received OCDM symbol in the time-domain, after CP removal, with the assumption of perfect synchronization, is

$$\mathbf{y}_{ij} = \mathbf{C}_{\alpha j} \mathbf{x}_{\xi i} + \mathbf{v}_{ij}, \quad (3.22)$$

where  $\mathbf{C}_{\alpha_j}$  is the circulant convolutional matrix associated with the  $j$ -th user after CP removal. This circulant convolutional matrix is obtained based on the vector  $\mathbf{h}_{\alpha_j} = [\mathbf{h}_j^T \mathbf{0}_{2N-L_j}^T]^T$ , in which  $\mathbf{0}_{2N-L_j}$  is the column vector composed of  $2N-L_j$  zeros. In the proposed scheme, FDE is employed in the Fourier domain. The received OCDM symbol from (3.22) is transformed to the frequency-domain as

$$\begin{aligned} \mathbf{Y}_{ij} &= \mathbf{F}_{2N} \mathbf{y}_{ij} \\ &= \mathbf{F}_{2N} \mathbf{C}_{\alpha_j} \mathbf{F}_{2N}^\dagger \mathbf{F}_{2N} \mathbf{x}_{\xi i} + \mathbf{F}_{2N} \mathbf{v}_{ij} \\ &= \mathbf{\Lambda}_j \mathbf{X}_{\xi i} + \mathbf{V}_{ij}, \end{aligned} \quad (3.23)$$

in which  $\mathbf{\Lambda}_j = \mathbf{F}_{2N} \mathbf{C}_{\alpha_j} \mathbf{F}_{2N}^\dagger$  is a diagonal matrix constituted by the coefficients of the PLC channel CFR associated with the  $j$ -th user and  $\mathbf{V}_{ij} = \mathbf{F}_{2N} \mathbf{v}_{ij}$ . For the sake of simplicity, if the ZF criterion is adopted for designing the FDE, then

$$\begin{aligned} \mathbf{X}_{\xi ij} &= \mathbf{\Lambda}_j^{-1} \mathbf{F}_{2N} \mathbf{y}_{ij} \\ &= \mathbf{X}_{\xi i} + \mathbf{\Lambda}_j^{-1} \mathbf{V}_{ij}. \end{aligned} \quad (3.24)$$

Observe that (3.24) returns an estimate of  $\mathbf{X}_{\xi ij} = \mathbf{F}_{2N} \mathbf{x}_{\xi ij}$  associated with the  $j$ -th user, which is in the frequency-domain. Returning (3.24) to the time-domain, the output is an estimate of  $\mathbf{x}_{\xi i}$  given by

$$\begin{aligned} \hat{\mathbf{x}}_{\xi ij} &= \mathbf{F}_{2N}^\dagger \mathbf{X}_{\xi ij} \\ &= \mathbf{x}_{\xi i} + \mathbf{v}_{\mathbf{\Lambda} ij}, \end{aligned} \quad (3.25)$$

where  $\mathbf{v}_{\mathbf{\Lambda} ij} = \mathbf{F}_{2N}^\dagger \mathbf{\Lambda}_j^{-1} \mathbf{V}_{ij}$ . The inverse mapping function  $\xi(\cdot)$  is applied to (3.25) and it is expressed as

$$\hat{\mathbf{x}}_{\nu ij} = \xi^{-1}(\hat{\mathbf{x}}_{\xi ij}) = \mathbf{x}_{\nu i} + \mathbf{v}_{\lambda ij}, \quad (3.26)$$

where  $\mathbf{v}_{\lambda ij} = \xi^{-1}(\mathbf{v}_{\mathbf{\Lambda} ij})$  and  $\hat{\mathbf{x}}_{\nu i}$  is an estimate of  $\mathbf{x}_{\nu i}$  associated with the  $j$ -th user. The received OCDM symbol is then brought back to the Fresnel domain by using the DFNT matrix as

$$\hat{\mathbf{x}}_{\nu i} = \mathbf{\Phi}_{2N} \mathbf{\Phi}_{2N}^\dagger \hat{\mathbf{x}}_{\nu i} + \mathbf{\Phi}_{2N} \mathbf{v}_{\lambda ij} = \dot{\mathbf{x}}_{\nu i} + \dot{\mathbf{v}}_{\lambda ij}, \quad (3.27)$$

with  $\dot{\mathbf{v}}_{\lambda ij} = \mathbf{\Phi}_{2N} \mathbf{v}_{\lambda ij}$ . Lastly, the inverse mapping function is applied to (3.27) in order to obtain an estimate of the transmitted MCp-CDMA symbol as

$$\hat{\mathbf{x}}_{ij} = \nu^{-1}(\hat{\mathbf{x}}_{\nu i}) = \dot{\mathbf{x}}_i + \dot{\mathbf{v}}_{ij}, \quad (3.28)$$

where  $\dot{\mathbf{v}}_{ij} = \nu^{-1}(\dot{\mathbf{v}}_{\lambda ij})$ . Observe that  $\hat{\mathbf{x}}_{ij}$  is the estimate of the  $i$ -th transmitted symbol,  $\dot{\mathbf{x}}_i$ , which is received by the  $j$ -th user.

The way the type-I OCDM scheme spreads each transmitted OCDM symbol is depicted in Fig. 7. To obtain this plot, it was used QPSK constellation for carrying out data communication. The depicted spectrogram, which refers to sub-chirp #130

when  $2N = 512$ , shows clearly the existence of two down-chirp spreading forms (linearly decreasing frequency) and two up-chirp spreading forms (linearly increasing frequency). Comparing such figure with the spectrogram obtained with the OCDM scheme (Appendix A), one can notice that the mapping functions are responsible for such distinct kind of spreading, which is the toll taken for designing the type-I OCDM scheme.

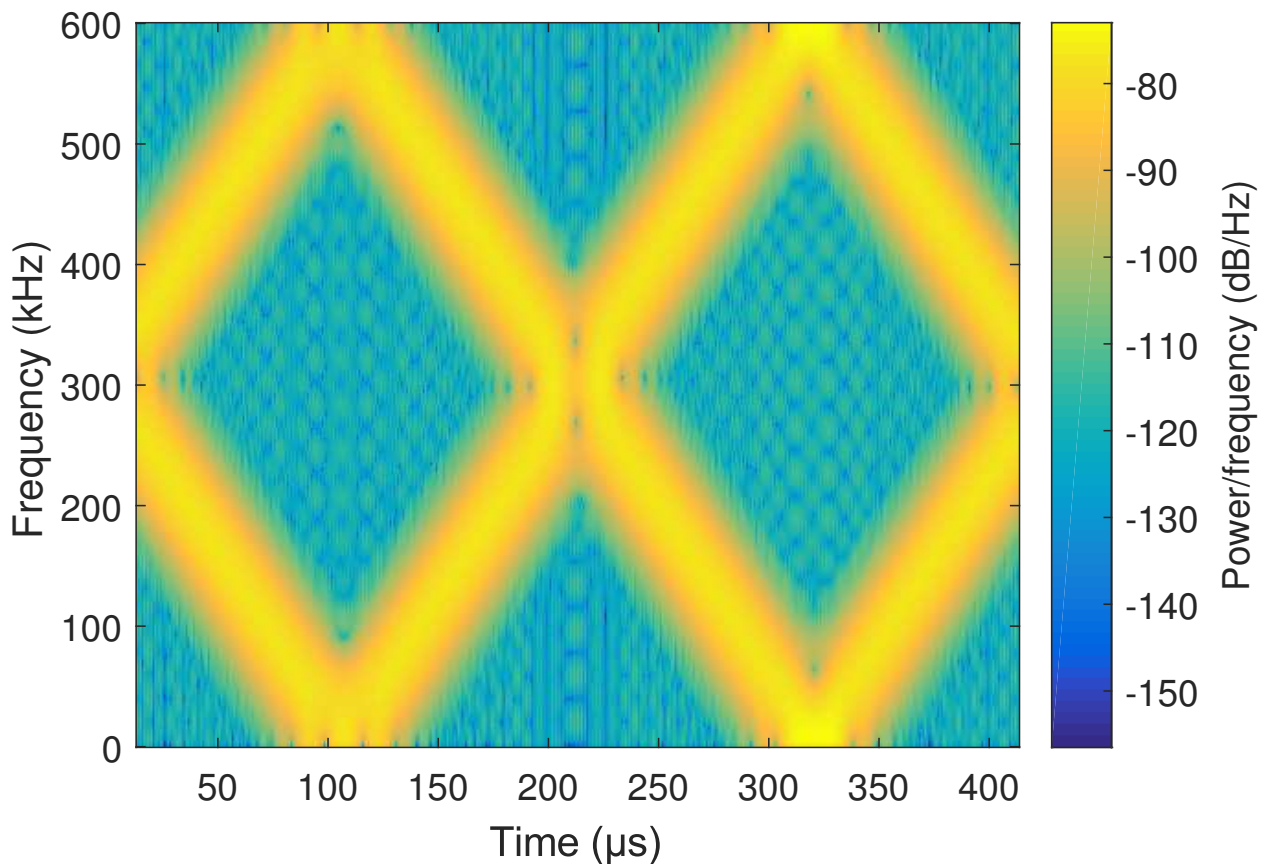


Figure 7: Spectrogram for type-I OCDM: sub-chirp #130 from a 256-length symbol considering QPSK modulation.

A video showing the spreading effect obtained using the remaining sub-chirps for type-I can be seen through the following hyper link: <https://drive.google.com/file/d/1KNJtRdWJN3mHbaeQaeQoJxW7LEXNzbPL/view?usp=sharing>. Alternatively a QR code with such link can be found in the Appendix B, Fig. 30-a.

### 3.3.2 The type-II and type-IV OCDM schemes

Fig. 9 depicts the block diagram for both type-II OCDM and type-IV OCDM. Note that Fig. 9-a and Fig. 9-b represent  $\mathcal{P}(\cdot)$  and  $\mathcal{Q}(\cdot)$ , respectively. The inputted symbol to  $\mathcal{P}(\cdot)$  is  $\dot{\mathbf{x}}_i$ , as expressed in (3.3), which has length  $N$ . Based on Fig. 9-a, the inverse DFNT is applied directly to obtain the time-domain vectorial representation of the transmitted signal,  $\dot{\mathbf{x}}_i$ , which can be expressed as  $\mathbf{x}_i = \Phi_N^\dagger \dot{\mathbf{x}}_i$ . Next, the mapping function  $\zeta(\cdot)$  is

applied in order to obtain  $\mathbf{x}_{\zeta i} = \zeta(\mathbf{x}_i)$ , where the output of the mapping function  $\zeta(\cdot)$  is driven by the type of OCDM as

$$\frac{\zeta(\mathbf{x}_i)}{\sqrt{2}} = \begin{cases} \mathbf{Q}_{\Re} \Re\{\mathbf{x}_i\} + \mathbf{Q}_{\Im} \Im\{\mathbf{x}_i\} & \text{for type-IV;} \\ \begin{bmatrix} \mathbf{I}_N \\ \dots \\ \mathbf{0}_N \end{bmatrix} \Re\{\mathbf{x}_i\} + \begin{bmatrix} \mathbf{0}_N \\ \dots \\ \mathbf{I}_N \end{bmatrix} \Im\{\mathbf{x}_i\} & \text{otherwise,} \end{cases} \quad (3.29)$$

in which  $\mathbf{Q}_{\Re}$  and  $\mathbf{Q}_{\Im}$  are matrices of size  $2N \times N$  formed by an identity matrix of size  $N$  with each line intercalated with a null matrix of the same size, defined as

$$\mathbf{Q}_{\Re} = \begin{bmatrix} 1 & 0 & \dots & 0 \\ 0 & 0 & \dots & 0 \\ 0 & 1 & \dots & 0 \\ 0 & 0 & \dots & 0 \\ \vdots & \vdots & \dots & \vdots \\ 0 & 0 & \dots & 1 \\ 0 & 0 & \dots & 0 \end{bmatrix}, \quad \mathbf{Q}_{\Im} = \begin{bmatrix} 0 & 0 & \dots & 0 \\ 1 & 0 & \dots & 0 \\ 0 & 0 & \dots & 0 \\ 0 & 1 & \dots & 0 \\ \vdots & \vdots & \dots & \vdots \\ 0 & 0 & \dots & 0 \\ 0 & 0 & \dots & 1 \end{bmatrix}. \quad (3.30)$$

The difference regarding the construction of type-II OCDM and type-IV OCDM is clearly the way the mapping function  $\zeta(\cdot)$  mounts its output. In fact,  $\zeta(\mathbf{x}_i)$  for the type-II OCDM scheme results in a  $2N$ -length symbol, whose first half is composed of the real part of  $\mathbf{x}_i$  while the other is composed of the imaginary part of  $\mathbf{x}_i$ . On the other hand,  $\zeta(\mathbf{x}_i)$  for the type-IV OCDM scheme results in an alternative form that is composed of the intercalation of real and imaginary parts of the vector  $\mathbf{x}_i$ . In both cases, the mapping function creates a real-valued OCDM symbol ( $\mathbf{x}_{\zeta i} \in \mathbb{R}^{2N \times 1}$ ), which can undergo baseband transmission, as in the HS-OFDM scheme. A graphic representation of  $\zeta(\cdot)$  is shown in Fig. 8-a for type-II and Fig. 8-b for type-IV.

Finally, a CP of length  $L_{cp}$  is inserted to obtain  $\mathbf{s}_i \in \mathbb{R}^{(2N+L_{cp}) \times 1}$ .

Assuming perfect synchronization, the received OCDM symbol in the time-domain after CP removal is expressed as

$$\mathbf{y}_{ij} = \mathbf{C}_{\alpha j} \mathbf{x}_{\zeta i} + \mathbf{v}_{ij}. \quad (3.31)$$

If FDE is employed, the received OCDM symbol from (3.31) is transformed to the frequency-domain as

$$\begin{aligned} \mathbf{Y}_{ij} &= \mathbf{F}_{2N} \mathbf{y}_{ij} \\ &= \mathbf{F}_{2N} \mathbf{C}_{\alpha j} \mathbf{F}_{2N}^\dagger \mathbf{F}_{2N} \mathbf{x}_{\zeta i} + \mathbf{F}_{2N} \mathbf{v}_{ij} \\ &= \mathbf{\Lambda}_j \mathbf{X}_{\zeta i} + \mathbf{V}_{ij}, \end{aligned} \quad (3.32)$$

where  $\mathbf{V}_{ij} = \mathbf{F}_{2N} \mathbf{v}_{ij}$ . The ZF equalization process is

$$\begin{aligned} \mathbf{X}_{\zeta ij} &= \mathbf{\Lambda}_j^{-1} \mathbf{F}_{2N} \mathbf{y}_{ij} \\ &= \mathbf{X}_{\zeta i} + \mathbf{\Lambda}_j^{-1} \mathbf{V}_{ij}. \end{aligned} \quad (3.33)$$

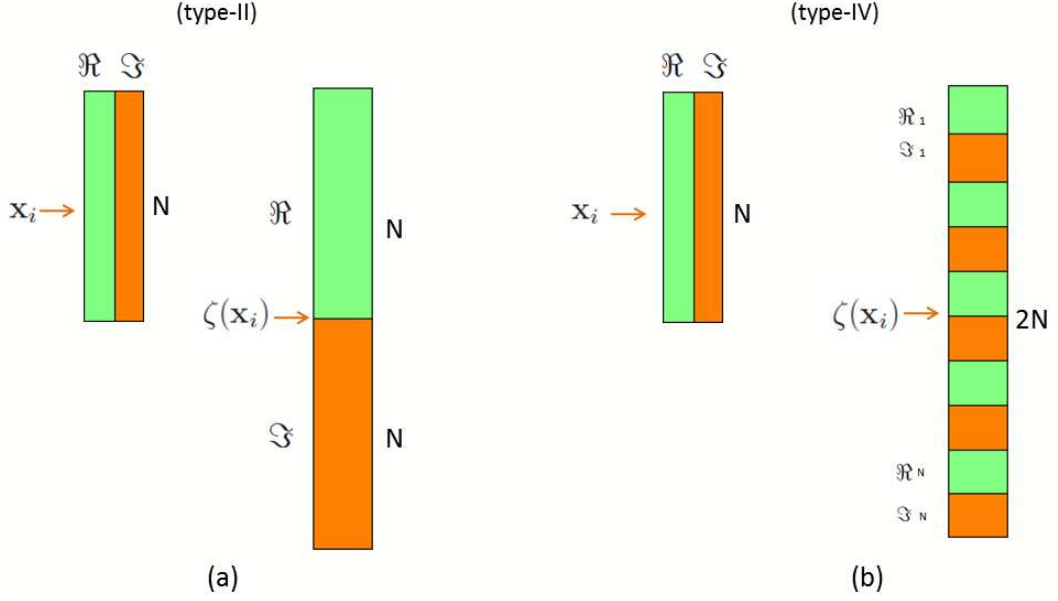


Figure 8: Graphic representation of  $\zeta(\cdot)$  for (a) type-II and (b) type-IV.

Note that other FDE criterion can be used and that (3.33) returns an estimate of  $\mathbf{X}_{\zeta_i} = \mathbf{F}_{2N}\mathbf{x}_{\zeta_i}$  associated with the  $j$ -th user, which is in the frequency-domain. Returning (3.33) to the time-domain, the output is an estimate of  $\mathbf{x}_{\zeta_i}$  associated with the  $j$ -th user, given by

$$\begin{aligned}\hat{\mathbf{x}}_{\zeta_{ij}} &= \mathbf{F}_{2N}^\dagger \mathbf{X}_{\zeta_{ij}} \\ &= \mathbf{x}_{\zeta_i} + \mathbf{v}_{\Lambda_{ij}},\end{aligned}\quad (3.34)$$

where  $\mathbf{v}_{\Lambda_{ij}} = \mathbf{F}_{2N}^\dagger \mathbf{\Lambda}_j^{-1} \mathbf{V}_{ij}$ . The inverse mapping function  $\zeta(\cdot)$  is applied to (3.34) and it is expressed as

$$\hat{\mathbf{x}}_{ij} = \zeta^{-1}(\hat{\mathbf{x}}_{\zeta_{ij}}) = \mathbf{x}_i + \mathbf{v}_{\lambda_{ij}},\quad (3.35)$$

in which  $\mathbf{v}_{\lambda_{ij}} = \zeta^{-1}(\mathbf{v}_{\Lambda_{ij}})$ . The received OCDM symbol is then brought back to Fresnel domain by the DFNT and an estimate of the  $i$ -th transmitted OCDM symbol associated with the  $j$ -th user is obtained as

$$\hat{\mathbf{x}}_{ij} = \mathbf{\Phi}_N \mathbf{\Phi}_N^\dagger \hat{\mathbf{x}}_i + \mathbf{\Phi}_N \mathbf{v}_{\Lambda_{ij}} = \hat{\mathbf{x}}_i + \hat{\mathbf{v}}_{\Lambda_{ij}},\quad (3.36)$$

where  $\hat{\mathbf{v}}_{\Lambda_{ij}} = \mathbf{\Phi}_N \mathbf{v}_{\Lambda_{ij}}$ .

The spectrograms shown in Figs. 10 and 11 depict the obtained spreading formats of the type-II and type-IV OCDM schemes, respectively, in the frequency-domain. For these plots, QPSK modulation is applied to input data and the sub-chirp #130 from a 256-length symbol transmission is represented. Since both types use one mapping function only, the spreading form produces one up-chirp and one down-chirp, accomplishing the effect of doubling the symbol size. Such spreading is clearly visible in Fig. 10. Due to the nature of  $\zeta(\cdot)$  for the type-IV OCDM scheme, which intercalates the real and imaginary

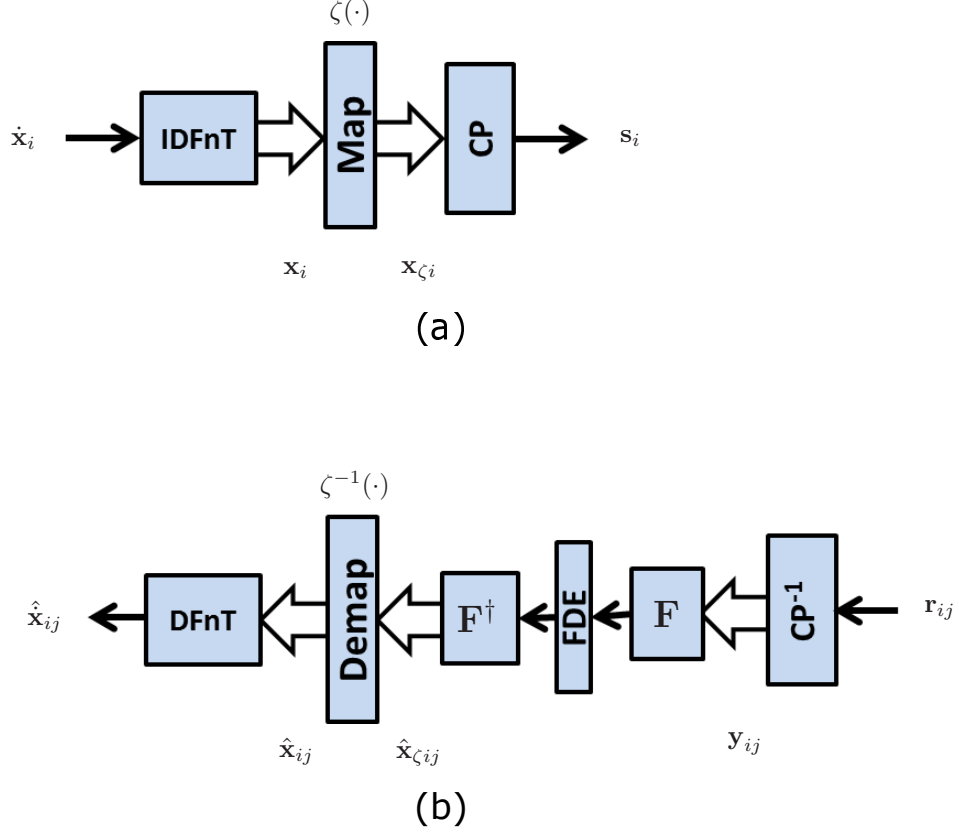


Figure 9: Block diagram of the type-II and type-IV OCDM schemes: (a) represents  $\mathcal{P}(\cdot)$  and (b) represents  $\mathcal{Q}(\cdot)$ .

parts of the symbol, the spectrogram associated with this scheme reflects such situation, as shown in Fig 11.

A video showing the spreading effect obtained using the remaining sub-chirps for type-II can be seen through the following link: <https://drive.google.com/file/d/1qsnxvShwpDE2P8SnpJsQiUiBg7pYTQbq/view?usp=sharing>. Alternatively a QR code with such link can be found in the Appendix B, Fig. 30-b.

For type-IV, the video showing the spreading effect obtained using the remaining sub-chirps can be seen through the following link: [https://drive.google.com/file/d/1To4LHfKdGkvhI4KTm87Wl003xzNbf\\_Mk/view?usp=sharing](https://drive.google.com/file/d/1To4LHfKdGkvhI4KTm87Wl003xzNbf_Mk/view?usp=sharing). Alternatively a QR code with such link can be found in the Appendix B, Fig. 30-d.

### 3.3.3 The type-III OCDM scheme

The type-III OCDM scheme takes advantage of a modification in the DFnT, making possible to obtain directly real-valued OCDM symbol in the time-domain. In order to present the modification, firstly, let the diagonal matrix  $\mathbf{\Gamma}_M$  be formed by pre- and

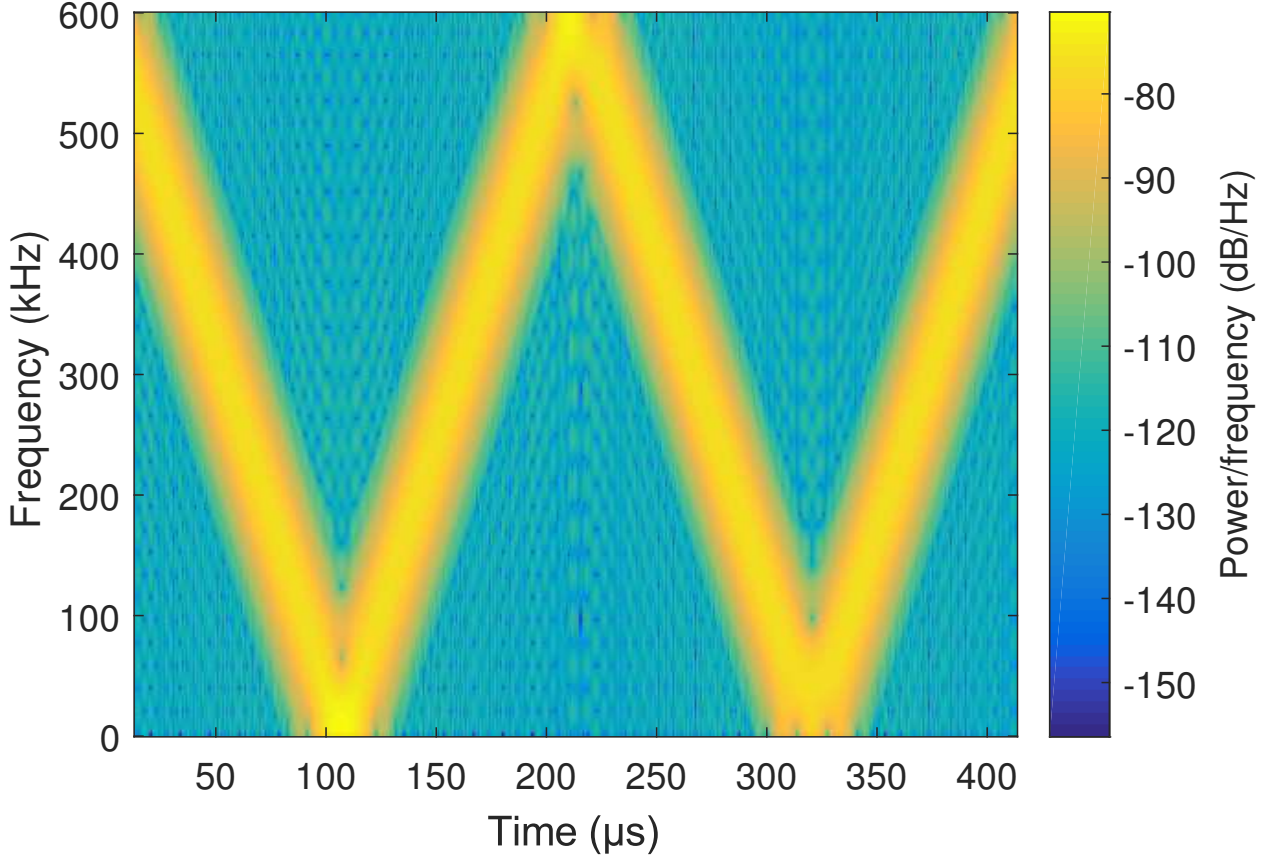


Figure 10: Spectrogram for the type-II OCDM scheme: sub-chirp #130 from a 256-symbol length considering QPSK modulation.

post-multiplication of the DF<sub>n</sub>T matrix as

$$\mathbf{F}_M \mathbf{\Phi}_M \mathbf{F}_M^\dagger = \mathbf{\Gamma}_M. \quad (3.37)$$

The diagonal  $M$ -inputs of  $\mathbf{\Gamma}_M$  are the eigenvalues of  $\mathbf{\Phi}_M$ . In [89], each element of  $\mathbf{\Gamma}_M = \mathbf{diag}\{\Gamma_{00}, \Gamma_{11}, \dots, \Gamma_{M-1M-1}\}$  for even  $M$  values is expressed as

$$\Gamma_{kk} = e^{(-j\pi/M)(k)^2}. \quad (3.38)$$

A subtle alteration in  $\mathbf{\Gamma}_M$  matrix is able to produce a real-valued OCDM symbol by artificially adding the Hermitian symmetry from the DFT to the DF<sub>n</sub>T. The modified  $\mathbf{\Gamma}_M$  matrix, responsible for obtaining a real-valued OCDM symbol in the time-domain, is denoted by  $\mathbf{\Gamma}_{M_{HS}} \triangleq \mathbf{diag}\{\Gamma_{HS,00}, \Gamma_{HS,11}, \dots, \Gamma_{HS,M-1M-1}\}$ , where

$$\Gamma_{HS,kk} \triangleq \begin{cases} e^{(-j\pi/M)(k)^2} & \text{for } k \leq M/2 \\ e^{(j\pi/M)(k)^2} & \text{for } k > M/2 \end{cases}. \quad (3.39)$$

This alteration allows the main diagonal of the  $\mathbf{\Gamma}_{M_{HS}}$  matrix to have Hermitian symmetry. Fig. 12 represents graphically the artificial insertion of the Hermitian symmetry for  $\mathbf{\Gamma}_M$ ,

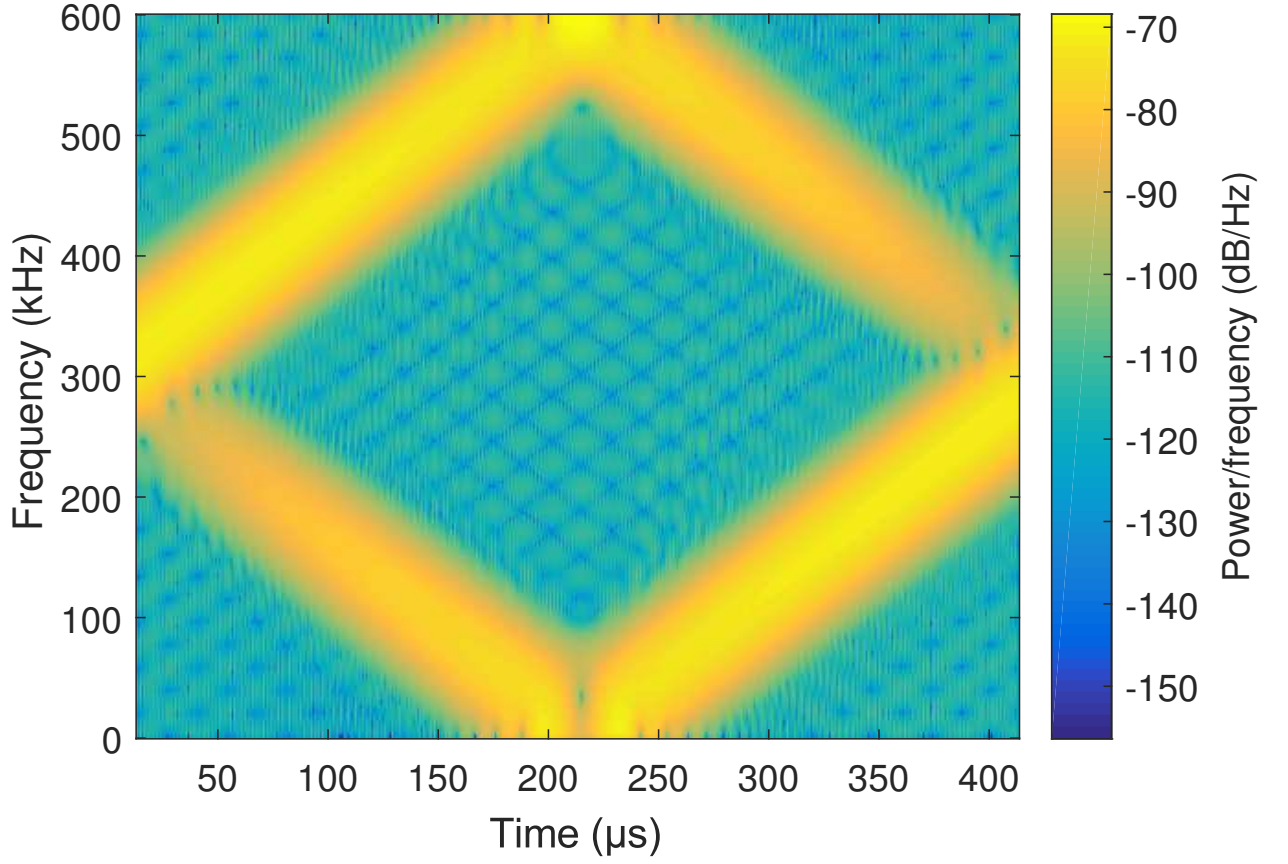


Figure 11: Spectrogram for the type-IV OCDM scheme: sub-chirp #130 from a 256-symbol length considering QPSK modulation.

creating a modified  $\mathbf{\Gamma}_{M_{HS}}$ .

Finally,  $\mathbf{\Phi}_{M_{HS}}$  can be obtained as

$$\mathbf{\Phi}_{M_{HS}} = \mathbf{F}_M^\dagger \mathbf{\Gamma}_{M_{HS}} \mathbf{F}_M. \quad (3.40)$$

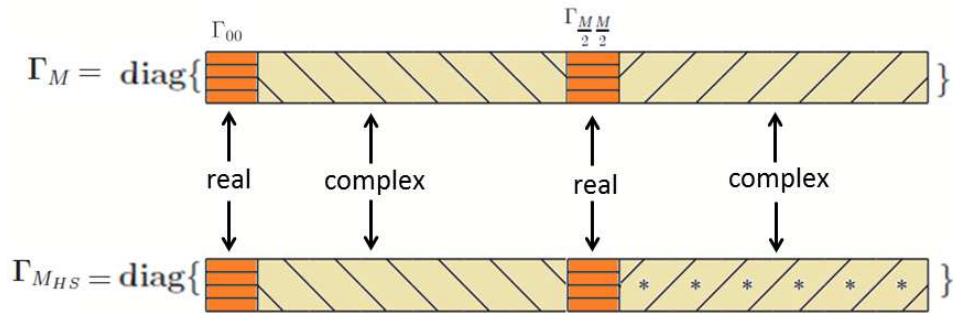


Figure 12: Graphic representation of the artificial insertion of the Hermitian symmetric property for a type-III OCDM.

It is important to mention that  $\mathbf{\Phi}_{M_{HS}} \in \mathbb{R}^{M \times M}$  and  $\mathbf{\Phi}_{M_{HS}} \mathbf{\Phi}_{M_{HS}}^\dagger = \mathbf{I}_M$ . Notice

that  $\Phi_{MHS}$  is a modified version of the DFnT.

This way, the block diagram for the type-III OCDM scheme is shown in Fig. 13. Observe that Fig. 13-a and Fig. 13-b denote  $\mathcal{P}(\cdot)$  and  $\mathcal{Q}(\cdot)$ , respectively. Based on this figure, the inputted composite symbol ( $\hat{\mathbf{x}}_i \in \mathbb{C}^{N \times 1}$ ) undergoes the mapping function  $\zeta(\cdot)$ , producing a real-valued OCDM symbol with length  $2N$  ( $\hat{\mathbf{x}}_{\zeta i} = \zeta(\hat{\mathbf{x}}_i) \in \mathbb{R}^{2N \times 1}$ ). It is worth to mention that the inputted composite symbol can also be generated so that it has only one dimension (i.e.,  $\hat{\mathbf{x}}_i \in \mathbb{R}^{2N \times 1}$ ). In this case, the mapping function  $\zeta(\cdot)$  is not required. Next, the mapped OCDM symbol ( $\hat{\mathbf{x}}_{\zeta i}$ ) is brought to the time-domain using the inverse of the modified version of the DFnT, yielding the time-domain vectorial representation of the OCDM symbol ( $\mathbf{x}_{\zeta i} = \Phi_{2NHS}^\dagger \hat{\mathbf{x}}_{\zeta i} \in \mathbb{R}^{2N \times 1}$ ). Next, a CP is inserted to obtain the transmitted composite signal ( $\mathbf{s}_i \in \mathbb{R}^{(2N+L_{cp}) \times 1}$ ).

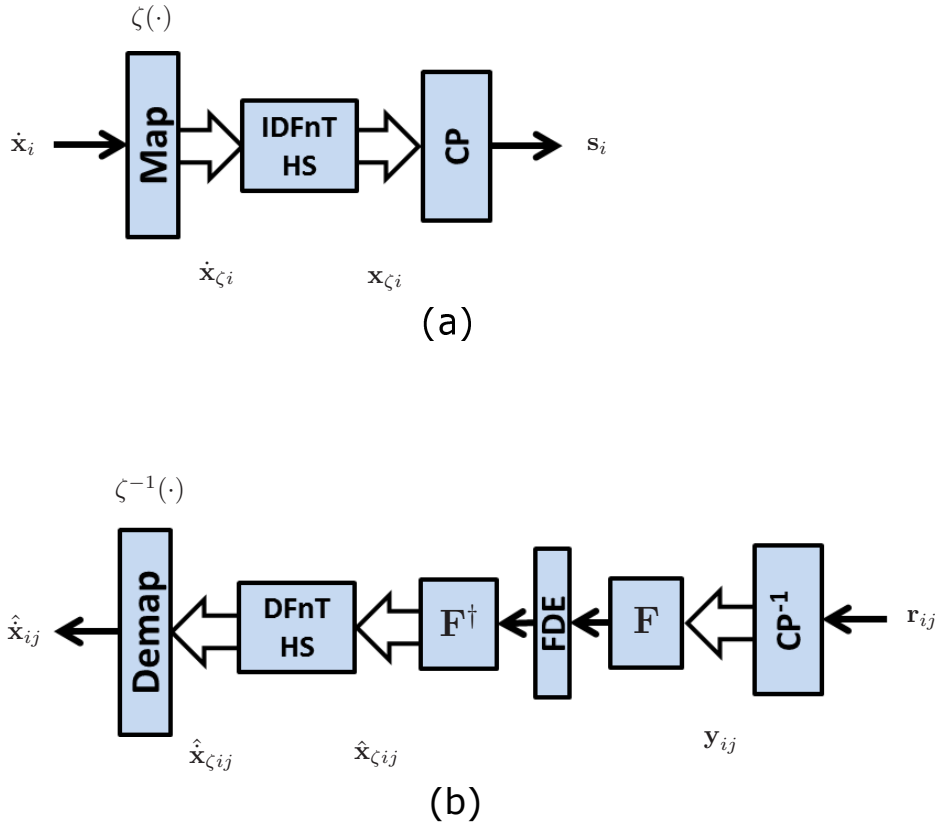


Figure 13: Block diagram of the OCDM type-III scheme: (a) represents  $\mathcal{P}(\cdot)$  and (b) represents  $\mathcal{Q}(\cdot)$ .

Assuming perfect synchronization at the receiver side, the vectorial representation of the received OCDM symbol in time-domain, after the removal of the CP from  $\mathbf{r}_{ij}$ , is

$$\mathbf{y}_{ij} = \mathbf{C}_{\alpha j} \mathbf{x}_{\zeta i} + \mathbf{v}_{ij}. \quad (3.41)$$

In order to perform FDE, the received OCDM symbol from (3.41) is transformed to the

frequency-domain as follows

$$\begin{aligned}
\mathbf{Y}_{ij} &= \mathbf{F}_{2N} \mathbf{y}_{ij} \\
&= \mathbf{F}_{2N} \mathbf{C}_{\alpha j} \mathbf{F}_{2N}^\dagger \mathbf{F}_{2N} \mathbf{x}_{\zeta i} + \mathbf{F}_{2N} \mathbf{v}_{ij} \\
&= \mathbf{\Lambda}_j \mathbf{X}_{\zeta i} + \mathbf{V}_{ij},
\end{aligned} \tag{3.42}$$

where  $\mathbf{V}_{ij} = \mathbf{F}_{2N} \mathbf{v}_{ij}$ . By adopting the ZF criterion, the FDE results in

$$\begin{aligned}
\mathbf{X}_{\zeta ij} &= \mathbf{\Lambda}_j^{-1} \mathbf{F}_{2N} \mathbf{y}_{ij} \\
&= \mathbf{X}_{\zeta i} + \mathbf{\Lambda}_j^{-1} \mathbf{V}_{ij}.
\end{aligned} \tag{3.43}$$

Notice that other equalization criterion can be used and (3.43) will return an estimate of  $\mathbf{X}_{\zeta i}$  which is associated with the  $j$ -th user in the frequency-domain. Returning  $\mathbf{X}_{\zeta ij}$  to the time-domain, the output is an estimate of  $\mathbf{x}_{\zeta i}$  perceived by the  $j$ -th user, which is given by

$$\begin{aligned}
\hat{\mathbf{x}}_{\zeta ij} &= \mathbf{F}_{2N}^\dagger \mathbf{X}_{\zeta ij} \\
&= \mathbf{x}_{\zeta i} + \mathbf{v}_{\Lambda ij},
\end{aligned} \tag{3.44}$$

where  $\mathbf{v}_{\Lambda ij} = \mathbf{F}_{2N}^\dagger \mathbf{\Lambda}_j^{-1} \mathbf{V}_{ij}$ . Finally, the  $i$ -th estimated OCDM symbol by the  $j$ -th user is then brought back to Fresnel domain by the modified version of the DF<sub>n</sub>T ( $\mathbf{\Phi}_{2N_{HS}}$ ) as follows:

$$\begin{aligned}
\hat{\mathbf{x}}_{\zeta ij} &= \mathbf{\Phi}_{2N_{HS}} \mathbf{\Phi}_{2N_{HS}}^\dagger \hat{\mathbf{x}}_{\zeta i} + \mathbf{\Phi}_{2N_{HS}} \mathbf{v}_{\Lambda ij} \\
&= \hat{\mathbf{x}}_{\zeta i} + \hat{\mathbf{v}}_{\Lambda ij},
\end{aligned} \tag{3.45}$$

in which  $\hat{\mathbf{v}}_{\Lambda ij} = \mathbf{\Phi}_{2N_{HS}} \mathbf{v}_{\Lambda ij}$ . The inverse mapping function  $\zeta(\cdot)$  is applied to (3.45) and an estimate of the transmitted OCDM symbol associated with the  $j$ -th user is obtained as

$$\hat{\mathbf{x}}_{ij} = \zeta^{-1}(\hat{\mathbf{x}}_{\zeta ij}) = \hat{\mathbf{x}}_i + \hat{\mathbf{v}}_{\lambda ij}, \tag{3.46}$$

where  $\hat{\mathbf{v}}_{\lambda ij} = \zeta^{-1}(\hat{\mathbf{v}}_{\Lambda ij})$ .

Fig. 14 depicts  $\mathcal{Q}(\cdot)$  demanding lower computational complexity than in  $\mathcal{Q}(\cdot)$  shown in Fig. 13-b. This low computational complexity is achieved by type-III OCDM scheme due to the sole application of the DFT and the exploitation of properties of diagonal matrices ( $\mathbf{\Lambda}_j$  and  $\mathbf{\Gamma}_{M_{HS}}$ ). Consequently, the computational complexity of this type of OCDM scheme is reduced. In this regard, (3.41) can be rewritten, taking advantage of the equivalent received OCDM symbol in Fresnel domain, as

$$\mathbf{y}_{ij} = \mathbf{C}_{\alpha j} \mathbf{\Phi}_{2N_{HS}} \hat{\mathbf{x}}_{\zeta i} + \mathbf{\Phi}_{2N_{HS}} \hat{\mathbf{v}}_{ij}. \tag{3.47}$$

The received OCDM symbol is then transformed to the frequency-domain as follows

$$\begin{aligned}
\mathbf{Y}_{ij} &= \mathbf{F}_{2N} \mathbf{y}_{ij} \\
&= \mathbf{F}_{2N} \mathbf{C}_{\alpha j} \mathbf{F}_{2N}^\dagger \mathbf{F}_{2N} \mathbf{\Phi}_{2N_{HS}}^\dagger \mathbf{F}_{2N}^\dagger \mathbf{F}_{2N} \hat{\mathbf{x}}_{\zeta i} + \mathbf{F}_{2N} \mathbf{\Phi}_{2N_{HS}}^\dagger \mathbf{F}_{2N}^\dagger \mathbf{F}_{2N} \hat{\mathbf{v}}_{ij}.
\end{aligned} \tag{3.48}$$

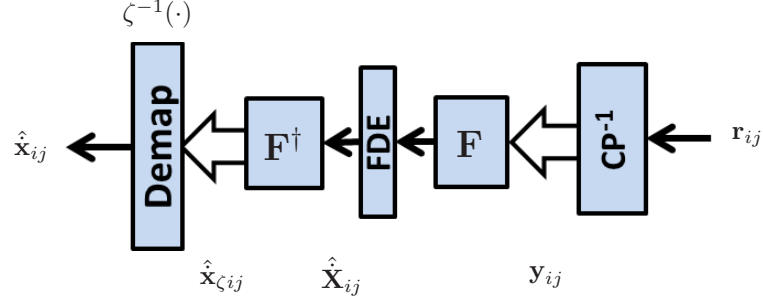


Figure 14: Block diagram for  $Q(\cdot)$  of the type-III OCDM scheme with reduced implementation complexity.

Using the  $\Lambda_j$  and  $\Gamma_{M_{HS}}$  matrices, (3.48) can be rewritten as follows

$$\mathbf{Y}_{ij} = \Lambda_j \Gamma_{2N_{HS}}^\dagger \mathbf{F}_{2N} \dot{\mathbf{x}}_{\zeta i} + \Gamma_{2N_{HS}}^\dagger \mathbf{F}_{2N} \dot{\mathbf{v}}_{ij}. \quad (3.49)$$

Consequently, an estimate of the  $i$ -th OCDM symbol obtained by the  $j$ -th user in the frequency dimension of the Fresnel domain can be expressed as

$$\begin{aligned} \hat{\mathbf{X}}_{ij} &= (\Lambda_j \Gamma_{2N_{HS}}^\dagger)^{-1} \Lambda_j \Gamma_{2N_{HS}}^\dagger \mathbf{F}_{2N} \dot{\mathbf{x}}_{\zeta i} + (\Lambda_{ij} \Gamma_{2N_{HS}}^\dagger)^{-1} \Gamma_{2N_{HS}}^\dagger \mathbf{F}_{2N} \dot{\mathbf{v}}_{ij} \\ &= \mathbf{F}_{2N} \dot{\mathbf{x}}_{\zeta i} + \Lambda_j^{-1} \mathbf{F}_{2N} \dot{\mathbf{v}}_{ij}. \end{aligned} \quad (3.50)$$

Equation (3.50) is then passed through the inverse DFT block, resulting in

$$\hat{\mathbf{x}}_{\zeta ij} = \dot{\mathbf{x}}_{\zeta i} + \mathbf{F}_{2N}^\dagger \Lambda_j^{-1} \mathbf{F}_{2N} \dot{\mathbf{v}}_{ij}, \quad (3.51)$$

which is an estimate of the  $i$ -th OCDM symbol obtained by the  $j$ -th user, missing only the inverse mapping function  $\zeta(\cdot)$ . It is important to highlight that the noise in (3.45) is the same as the one found in (3.51), i.e.,  $\dot{\mathbf{v}}_{\Lambda ij} = \mathbf{F}_{2N}^\dagger \Lambda_j^{-1} \mathbf{F}_{2N} \dot{\mathbf{v}}_{ij}$ . As a consequence, both receivers have equivalent performance in terms of bit error probability.

Fig. 15 shows the spectrogram of the type-III OCDM scheme. In this figure, subchirp #130 from a 256-length OCDM symbol is depicted, considering that QPSK modulation is applied to input data. The frequency spreading of the transmitted signal associated with the use of type-III OCDM scheme is very close to that of the OCDM scheme, see Appendix A.

A video showing the spreading effect obtained using the remaining sub-chirps for type-III can be seen through the following link: <https://drive.google.com/file/d/1pMjPdmQFE-Mwfh1n4mHhcvJVMXRg720N/view?usp=sharing>. Alternatively a QR code with such link can be found in the Appendix B, Fig. 30-c.

### 3.4 SIMULATION RESULTS

This section addresses numerical results regarding performance of the OCDM and MCp-CDMA schemes when AWGN, ABGN, PLC channel corrupted by AWGN, and

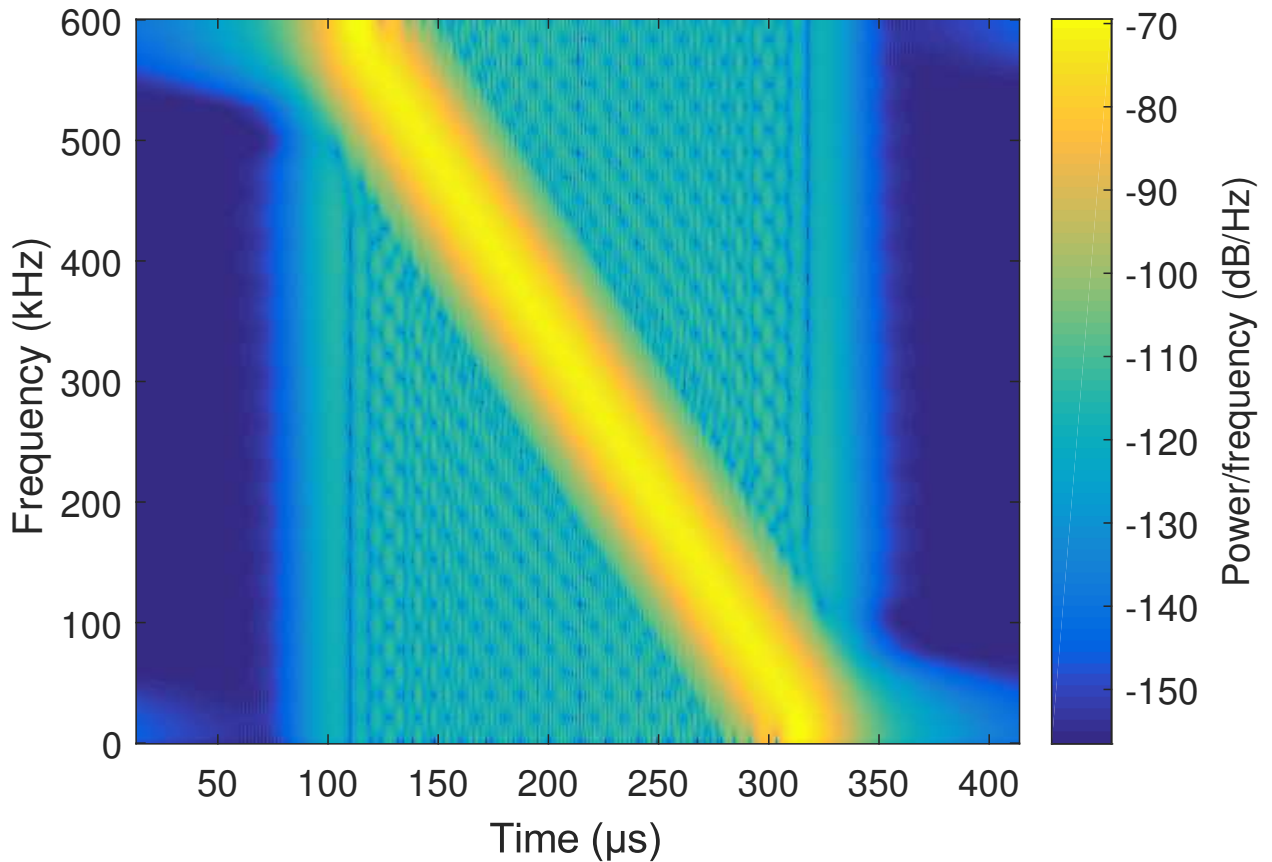


Figure 15: Spectrogram for the type-III OCDM scheme: sub-chirp #130 from a 256-symbol length considering QPSK modulation.

PLC corrupted by ABGN models are considered. All analyses are carried out in terms of bit error rate (BER) performance based on the assumption that complete channel state information (CSI) is available at the receiver side. In other words, the transmitter does not have any information about the channel state information and, as a consequence, a fair comparison among the proposed and existing schemes will be accomplished. In this regard, the analyses are expressed for the single-user case, see Subsection 3.4.1, and then, the multiuser case is examined, see Subsection 3.4.2. Moreover, HS-OFDM and SC-CP schemes [61, 94, 100, 101] are used for comparison purposes in both cases. It is important to emphasize that the HS-OFDM scheme makes use of uniform energy and bit allocation technique in order to ensure fairness in all simulations. In addition, in order for the results to be compatible and coherently analyzed, the SC-CP scheme uses the mapping function  $\zeta(\cdot)$ , where the output will be the real part of an  $N$ -length input vector concatenated with the imaginary part of the same input vector, forming a real-valued vector of length  $2N$ . The use of these schemes aims to provide readers with the kind of improvement that the OCDM and MCp-CDMA schemes can offer to PLC systems, which are supposed to operate over electric power grids eventually characterized by the aforementioned set of channel models.

### 3.4.1 The OCDM scheme: single-user analyses

The OCDM scheme in the single-user scenario can be understood as a special case of the multiuser, constructively ignoring the initial and final parts of Fig. 4 which corresponds exactly to the DS-CDMA scheme. This way, the blocks named ‘spreader’, ‘encoder’, ‘decoder’, and ‘de-spreader’, as well as the summation block are not part of a single-user system. In this regard, Fig. 16 depicts the single-user system representation block diagram. It is important to clarify that, in this case,  $\mathcal{P}(\cdot)$ ,  $\mathcal{Q}(\cdot)$ , and all elements

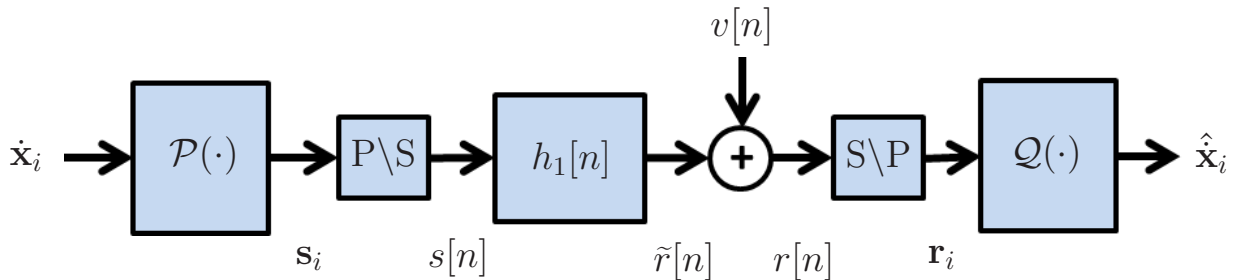


Figure 16: Single-user representation block diagram.

in between these two blocks (considering only one user) remain untouched. The mapped symbols coming from a digital modulator will feed directly the vector  $\hat{\mathbf{x}}_i \in \mathbb{C}^{N \times 1}$ . The  $\mathcal{P}(\cdot)$  function will produce vector  $\mathbf{s}_i \in \mathbb{R}^{(2N+L_{cp}) \times 1}$  as an output. At this point, the time-domain vectorial representation of the  $i$ -th OCDM symbol is ready to reach the P/S converter that is responsible for serializing consecutive OCDM symbols, forming the discrete-time sequence  $s[n]$ . This signal is then convolved linearly with the CIR,  $\{h_1[n]\}_{n=0}^{L_1-1}$ , resulting in the signal  $\tilde{r}[n]$ , which is corrupted by the additive noise  $v[n]$ , giving rise to the received signal  $r[n]$ . With the assumption that  $r[n]$  undergoes a S/P conversion, the adoption of perfect symbol synchronization, and the fact that  $L_{cp} \geq L_1 - 1$ , then the  $i$ -th received OCDM symbol is denoted by  $\mathbf{r}_i \in \mathbb{R}^{(2N+L_{cp}) \times 1}$ . On the other side, the received symbol  $\mathbf{r}_i$  will be the input of  $\mathcal{Q}(\cdot)$ , having the symbol  $\hat{\mathbf{x}}_i \in \mathbb{C}^{N \times 1}$  as output, which in its turn will be an estimate of  $\hat{\mathbf{x}}_i$ .

For carrying out these simulations, we assumed  $N = 128$ , a frequency band between 0 and  $B = 600 \text{ kHz}$  (i.e., the data communication occurs in the baseband), and BPSK and QPSK modulations. The ABGN parameters used in the computational simulations for modeling the PLC impulsive noise are as follows:  $K = 10$ ;  $L_m = 30$ ;  $p = 0.9$ . For obtaining the AWGN model, the ABGN model is used with  $K = 1$ . This simple change equates the variances  $\sigma_0^2$  and  $\sigma_1^2$  and produces only white Gaussian noise as output. The PLC channels employed in these analyses, when required, are based on multipath channel model, which was introduced in [33]. The parameters for this model are taken from the IEEE 1901.2 standard [102, Annex D], resulting in PLC CIR with  $L_1 \leq 30$ . Fig. 17 portrays the normalized CFR of the PLC channel considered in this section.

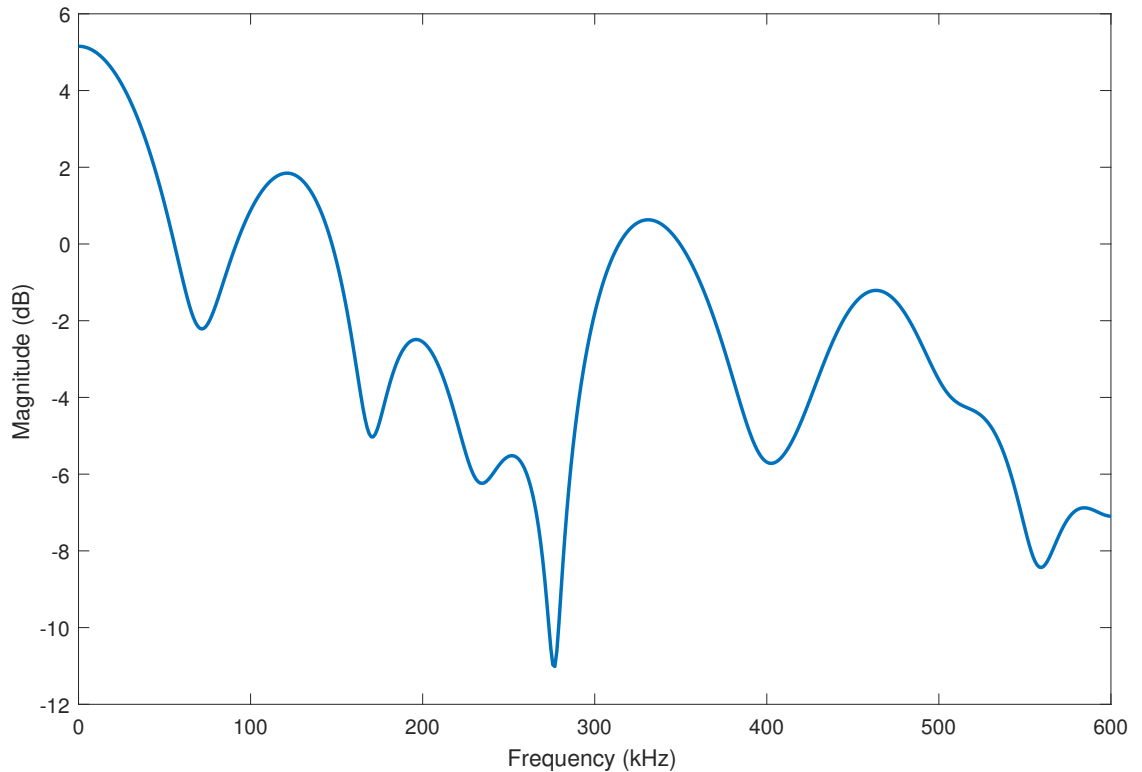


Figure 17: Normalized CFR of the PLC channel considered for performance analyses.

The analyses initiate with the AWGN channel. Fig. 18 portrays, the BER performances in such scenario for the four types of the OCDM scheme together with BPSK and QPSK for modulating the inputted data. Furthermore, HS-OFDM and SC-CP schemes are also used for comparison purposes. Observe that the BER performance of each type of OCDM (analyzing BPSK and QPSK modulations separately) matches the BER performances of HS-OFDM and SC-CP schemes, demonstrating similar results to those indicated in [89]. In this scenario, the four types of OCDM, HS-OFDM, and SC-CP schemes achieve similar performances for both BPSK and QPSK modulations. In other words, under the presence of AWGN channel model, all schemes offer the same performance in terms of BER.

The BER performances considering the ABGN channel model and both BPSK and QPSK for modulating the inputted symbols are shown in Fig. 19. This figure clearly portrays the effect that impulsive noise causes in the shape of the curve for the SC-CP scheme, creating, as a result, a stretch in the central part of the curve. This shows a more sensitive behavior of the SC-CP scheme in an impulsive noise environment compared to the other schemes, which is related to the direct form the SC-CP scheme spreads each transmitted symbol. The SC-CP symbol occupies the whole frequency bandwidth and the impulsive noise is also totally spread over the whole frequency bandwidth because it is a Gaussian random process. It means that for low values of signal-to-noise ratio (SNR), the

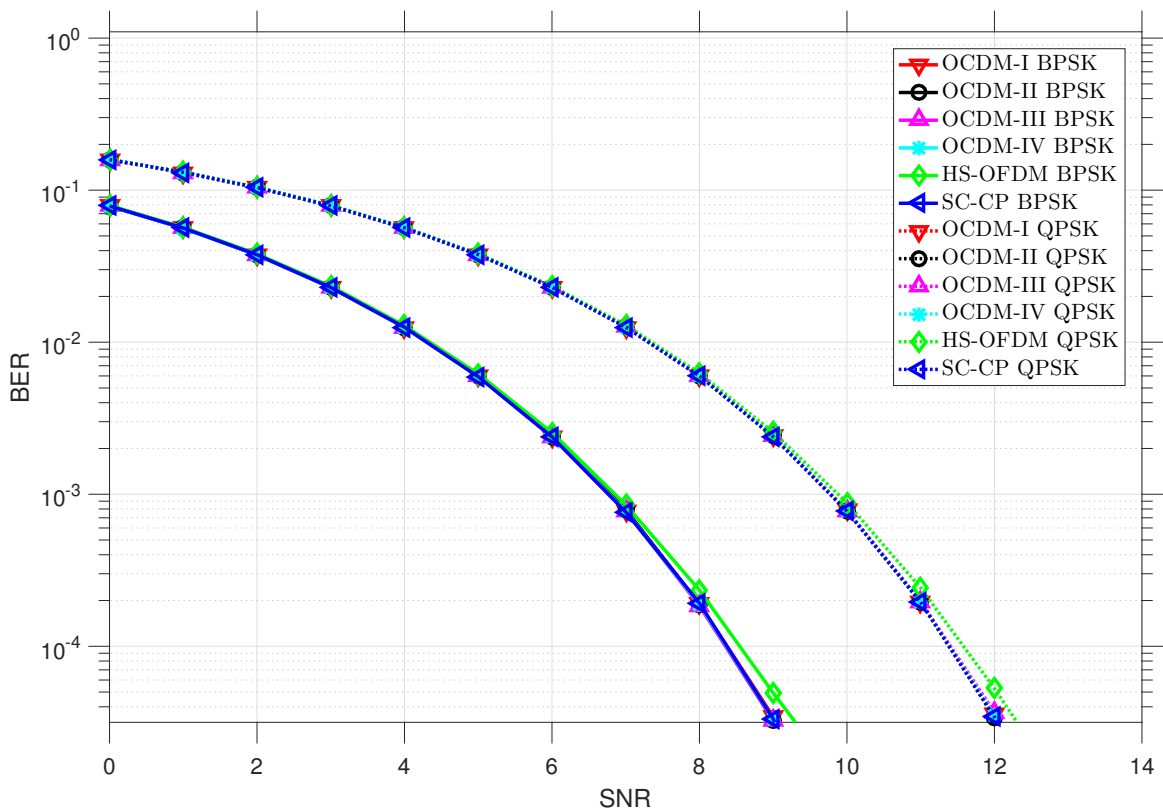


Figure 18: BER performances considering the AWGN channel model and both BPSK and QPSK modulations.

presence of impulsive noises has smaller impact on the BER performance than the other schemes. On the other hand, the increase in SNR values ( $\text{SNR} \geq 14$  dB) shows that the SC-CP scheme yields the worst BER performance. The rationality behind it is the fact that SC-CP symbols are constituted by consecutive BPSK or QPSK symbols in the time-domain and, as the occurrence of impulsive noise is totally defined in the time-domain, it is clear that the influence of the impulsive noise is relevant for  $\text{SNR} \geq 14$  dB because it impacts the detection of finite number of consecutive BPSK or QPSK symbols. Observe also the good performance of all types of OCDM and HS-OFDM schemes in an impulsive noise environment. Moreover, the type-III OCDM scheme yields SNR that is 1 dB apart from the other types of OCDM, but even though, it still has a better performance result than the SC-CP scheme.

An important working condition for the use of the OCDM scheme to deal with single-user case is when intersymbol interference (ISI) becomes relevant, as indicated in [89]. Essentially, the idea is to verify the level of degradation introduced by assuming that  $L_{cp} < L_1 - 1$ . In order to perform this analysis when the data communication occurs in the baseband, computational simulations were performed considering a reduction of the  $L_{cp}$ . In this regard, the correspondent CIR energy reduction associated with each  $L_{cp}$  length considered in this analysis are shown in Table 1. It is important to highlight

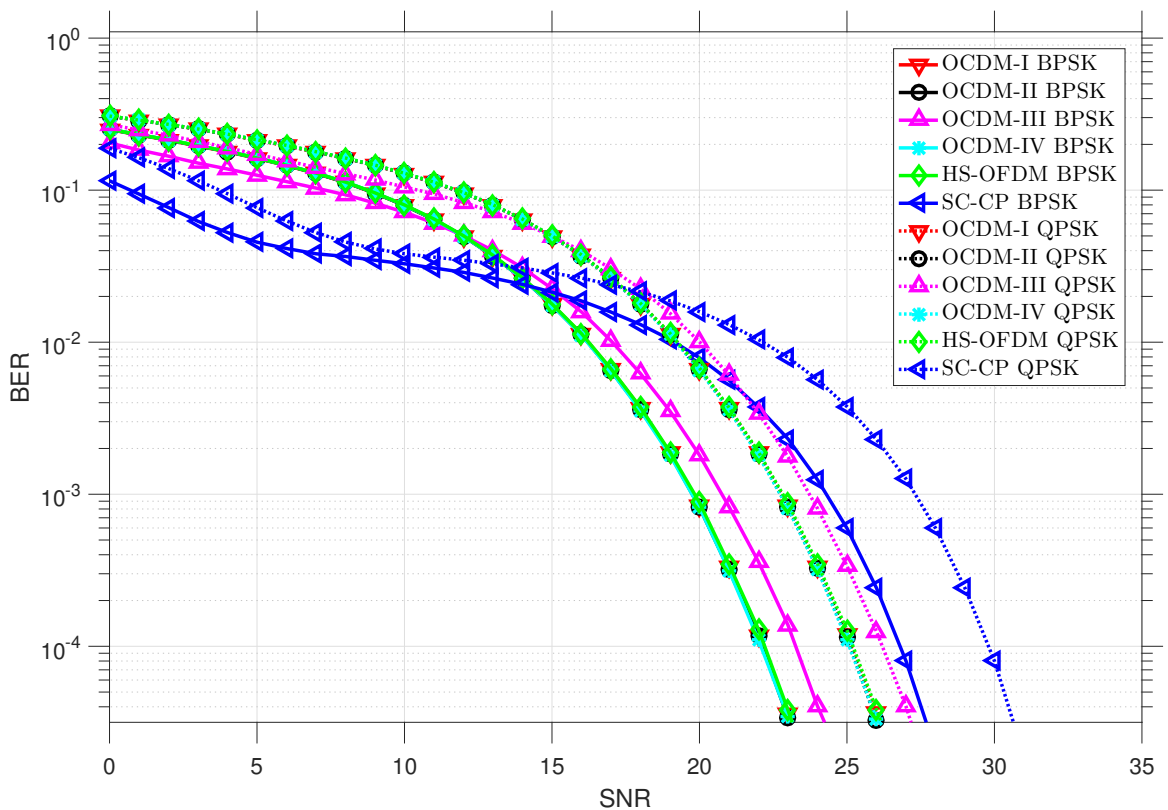


Figure 19: BER performances considering the ABGN channel model and both BPSK and QPSK modulations.

Table 1: Correspondence between  $L_{cp}$  reduction and its associated CIR energy.

$L_{cp}$	Length Reduction (%)	Energy Reduction (%)
30	0	0
15	50	15
7	77	83
3	90	87

that the  $L_{cp}$  length reduction steps, relatively, do not correspond to the same CIR energy reductions. When  $L_{cp}$  falls from 100% to 50% of  $L_1$ , the equivalent channel energy falls only 15% and when  $L_{cp}$  falls from 50% to 77% of  $L_1$ , the equivalent energy is reduced from 15% to 83%, which is the largest difference among the  $L_{cp}$  reduction steps considered. The following set of plots take into account these steps.

The set of plots of Fig. 20 considers the PLC channel corrupted by AWGN and the BPSK modulation as input data. Fig. 20-a shows the BER performance when  $L_{cp}$  corresponds to 100% of  $L_1$ , i.e, inexistent ISI condition. It is observed that all types of OCDM and SC-CP schemes have better BER performance than the HS-OFDM, reflecting the behavior of a frequency-selective channel and the use of uniform bit and energy allocations in the OFDM scheme. Fig. 20-b shows BER performance when  $L_{cp}$  corresponds to 50% of  $L_1$ . Although  $L_{cp}$  has been reduced by half, the channel energy corresponding

to that length contains 83% of its total energy. This was enough to trigger the error floor for both HS-OFDM and SC-CP schemes, keeping BER levels around  $5 \times 10^{-4}$  and  $3 \times 10^{-3}$ , respectively. In this condition, all types of OCDM do not present an error floor, at least, down to a BER of  $10^{-4}$ , demonstrating comparatively, the good performance of such scheme. Fig. 20-c shows BER performance with an  $L_{cp}$  reduction corresponding to 23% of  $L_1$ , which also reflects in an important channel energy reduction as now only 17% of the total CIR energy is being used for protection against ISI. This condition triggers the error floor relatively earlier and in higher BER values not only for HS-OFDM and SC-CP, but also for all types of OCDM. Observe all OCDM types present a lower noise floor than HS-OFDM and SC-CP. Moreover, type-III OCDM continues on its downward trajectory, without reaching an error floor, at least, down to a BER of  $10^{-4}$ . Fig. 20-d shows BER performances with a drastic reduction of  $L_{cp}$  resulting in 10% of  $L_1$ . The corresponding CIR energy being used for protection against ISI has not suffered a significant reduction if compared to previous situation (Fig. 20-c) and is now about 13%. In this case, type-III OCDM also reaches an error floor; however, with much lower BER than the others ( $10^{-4}$  of BER is reached at an SNR of nearly 25 dB). Type-IV OCDM reaches an error floor with a BER level of  $2 \times 10^{-3}$  at an SNR of nearly 26 dB. Types I and II OCDM and HS-OFDM have error floors in a close condition, considering a BER not lower than  $3.7 \times 10^{-3}$  at an SNR of 30 dB. The SC-CP scheme was the one for which the  $L_{cp}$  reduction had the highest impact in terms of BER performance, as it reached an error floor for a BER level not lower than  $3.8 \times 10^{-2}$  and an SNR of almost 20 dB. Observe that when  $L_{cp}$  is shorter than  $L_1$ , all types of the OCDM scheme tend to surpass the performance of HS-OFDM and SC-CP schemes.

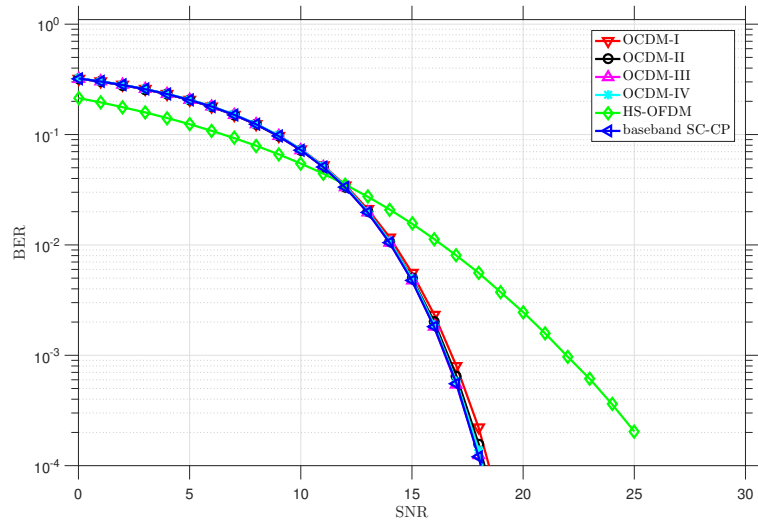
The set of plots of Fig. 21 considers the PLC channel model over an AWGN environment with QPSK modulation as input data. Fig. 21-a considers  $L_{cp} = 100\%$  of  $L_1$ . Observe that the BER plots reach higher SNR values than those using BPSK (Fig. 20-a), as expected. Furthermore, confronting the performances achieved by HS-OFDM in Figs. 20-a and 21-a, one can see that HS-OFDM degrades when compared to baseband OCDM and SC-CP schemes. Such performance degradation is the result from a frequency-selective channel. Baseband OCDM together with SC-CP kept up with better performance, also using QPSK. Fig. 21-b considers  $L_{cp} = 50\%$  of  $L_1$ . The BER plots of this figure shows type-II OCDM as the best scheme, followed closely by type-I OCDM. In such condition, types III and IV OCDM, SC-CP, and HS-OFDM reach error floor. However, both types II and IV of OCDM presented lower error floors than HS-OFDM and SC-CP schemes. Fig. 21-c considers  $L_{cp} = 23\%$  of  $L_1$ , when the energy associated with CIR length suffers the greatest fall among the  $L_{cp}$  steps used. One can note that type-II OCDM is the best scheme in this plot (in fact, type-II is the best scheme for such set). The lower error floor is reached by type-II OCDM scheme for a BER level of  $5.4 \times 10^{-3}$  and an SNR of 30 dB. The highest error floor is reached by SC-CP scheme for a BER

level not lower than  $1.5 \times 10^{-2}$  and an SNR of 25 dB. Fig. 21-d considers  $L_{cp} = 10\%$  of  $L_1$ . Observe that, except for type-III OCDM, all other types have better performance (even tiny) than HS-OFDM and SC-CP schemes. Observe also that with an extreme  $L_{cp}$  reduction, the performance of all types of OCDM are more and more approaching the HS-OFDM scheme.

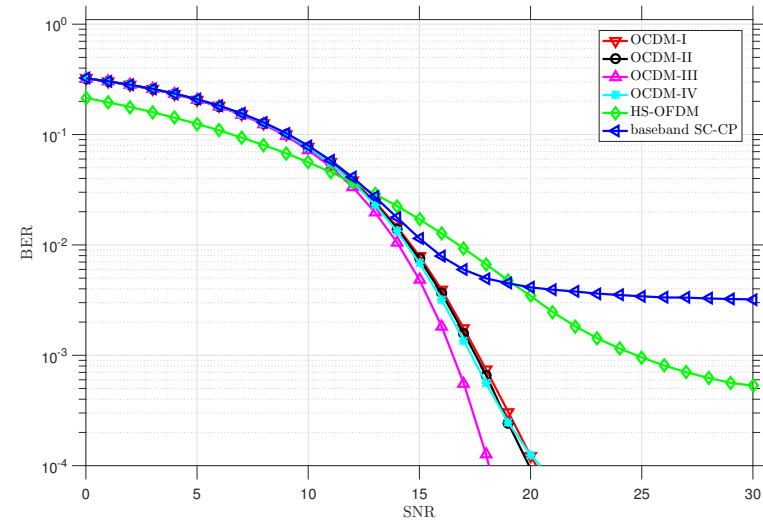
The set of plots of Fig. 22 considers the PLC channel model over an ABGN environment with BPSK modulation as input data. Fig. 22-a considers  $L_{cp} = 100\%$  of  $L_1$ . It must be observed the interesting behavior of HS-OFDM and SC-CP schemes when the simulation considers both PLC channel (in which HS-OFDM had not a good performance, as depicted in Figs. 20-a and 21-a) and ABGN environment (in which baseband SC-CP performance had suffered more than other schemes, as depicted in Fig. 19). When these elements are put together, the two aforementioned schemes degrade their performances relatively to baseband OCDM, as expected; however, for a BER of  $10^{-4}$ , SC-CP is 3 dB better than HS-OFDM. Fig. 22-b considers  $L_{cp} = 50\%$  of  $L_1$ . This figure exhibits the performance result when ISI increases, and in this condition, SC-CP (which was better than HS-OFDM in the previous plot) is more affected, swapping positions with HS-OFDM. Nevertheless, these two schemes reach, in this condition, error floors with BER levels of  $5 \times 10^{-4}$  for HS-OFDM and  $3 \times 10^{-3}$  for baseband SC-CP. All types of OCDM still have the best performance, continuing on its downward trajectory, not reaching an error floor, at least, down to a BER of  $10^{-4}$ . Fig. 22-c considers  $L_{cp} = 23\%$  of  $L_1$ . This condition reveals an interesting performance of the scheme with the least computational complexity, type-III OCDM, as it was the only scheme not reaching an error floor, leastwise down to a BER of  $10^{-4}$ . On the other hand, the performance of types I, II, and IV OCDM were close to HS-OFDM, with error floor levels not less than  $1 \times 10^{-3}$ . Furthermore, SC-CP quickly reached an error floor, with a BER level of  $2 \times 10^{-2}$ . Fig. 22-d considers  $L_{cp} = 10\%$  of  $L_1$ . In such plot, type-III OCDM also reaches an error floor, however, with a BER much lower than the others. Except for type-III OCDM, when a drastic reduction of  $L_{cp}$  takes place, the other types of OCDM are close to the HS-OFDM performance. Moreover, considering a BER of  $10^{-4}$ , type-III OCDM scheme reaches an error floor at an SNR of 38 dB. Considering a BER of  $2 \times 10^{-3}$ , type-IV OCDM scheme reaches an error floor at an SNR of 39 dB. Considering a BER not lower than of  $4 \times 10^{-3}$ , type-II OCDM scheme reaches an error floor at an SNR also of 39 dB. Considering a BER not lower than of  $4.4 \times 10^{-3}$ , HS-OFDM scheme reaches an error floor at an SNR of 39 dB. Considering a BER not lower than of  $5 \times 10^{-3}$ , type-I OCDM scheme reaches an error floor at an SNR of 39 dB. Finally, for a BER not lower than of  $3.7 \times 10^{-2}$ , SC-CP scheme reaches an error floor at an SNR of 34 dB. This set of plots have similar results to those using AWGN (Fig. 20), but in an impulsive environment, higher SNR values are needed to reach the same BER values, as expected. In a comparison between Fig. 22-b and Fig. 20-b (similar situation using AWGN), BER curves for all types of OCDM have a more uniform per-

formance, but requiring higher SNR values. Overall, it should be noticed that in a hard noise situation, such as the one considered in this simulation set, the behavior of all types of OCDM tends to be more advantageous, mainly in relevant ISI condition.

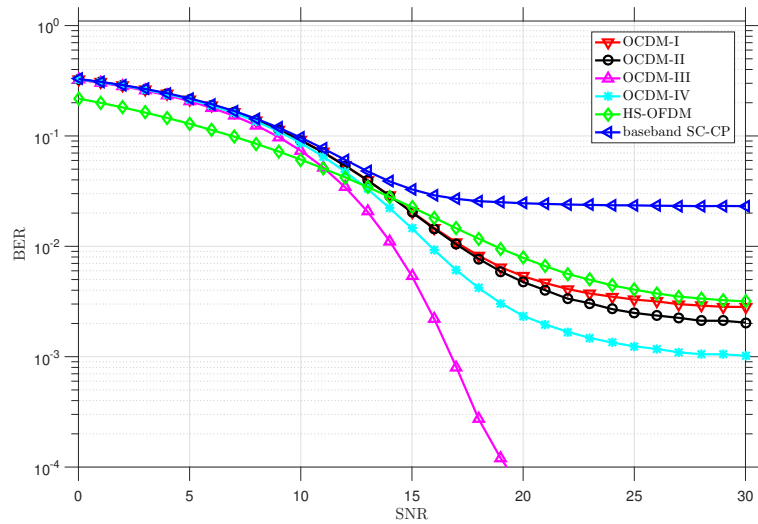
The same advantage is perceived in the set of plots of Fig. 23 that considers the PLC channel model corrupted by ABGN with QPSK modulation as input data. Fig. 23-a considers  $L_{cp} = 100\%$  of  $L_1$ , and it depicts a similar situation perceived in Fig. 22-a, where SC-CP and HS-OFDM suffer with the impulsive noise presence and the frequency selectivity of PLC channel. As a result, all types of OCDM performed better comparatively to HS-OFDM and SC-CP schemes. Fig. 23-b considers  $L_{cp} = 50\%$  of  $L_j$ . In this figure, types III and IV OCDM reached error floors with a BER level of  $3 \times 10^{-4}$ , differently from the analogous situation depicted in Fig. 22-b, where all types of OCDM are still on a downward trajectory, leastwise down to a BER of  $10^{-4}$ . Fig. 23-c considers  $L_{cp} = 23\%$  of  $L_1$ , which is the largest CIR energy reduction situation. In the face of that, the performance results of the simulated schemes are close to those depicted in Fig. 21-c, but requiring higher SNR values to reach similar BER levels. Albeit the error floor levels are close to each other, clearly all types of OCDM have better performances than HS-OFDM and SC-CP, except for type-III OCDM. Fig. 23-d considers  $L_{cp} = 10\%$  of  $L_1$ , simulating a severe ISI condition. One can observe that, despite type-II OCDM has a better performance, the difference among the error floor levels of the simulated schemes is small. In such situation, the advantage of all types of OCDM are not so evident, and also, these schemes have a close performance to the HS-OFDM scheme.



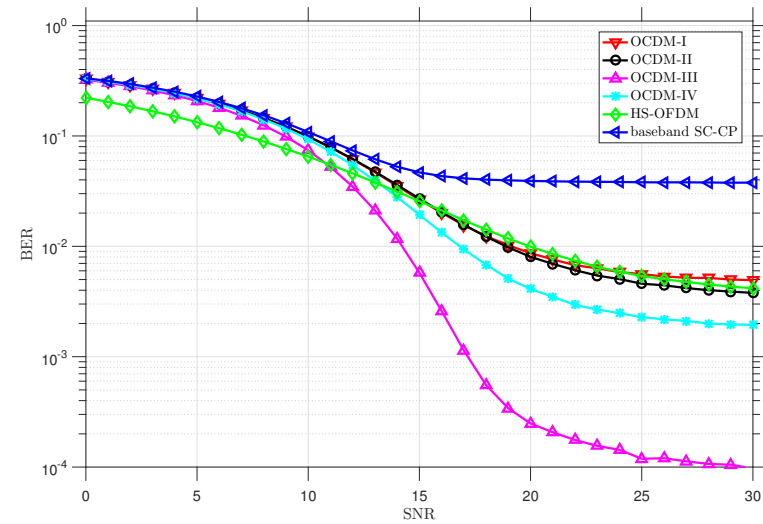
(a)



(b)

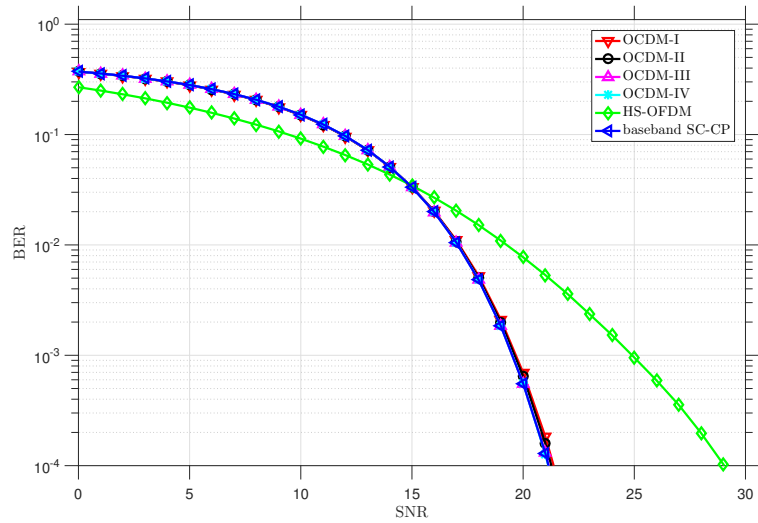


(c)

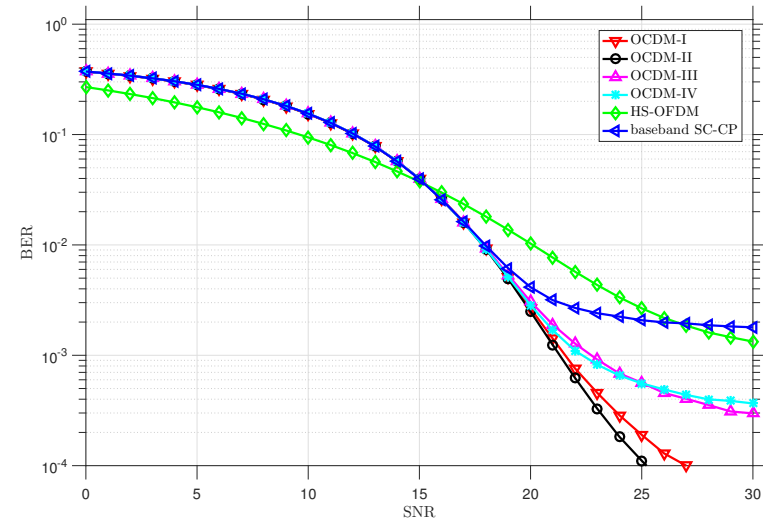


(d)

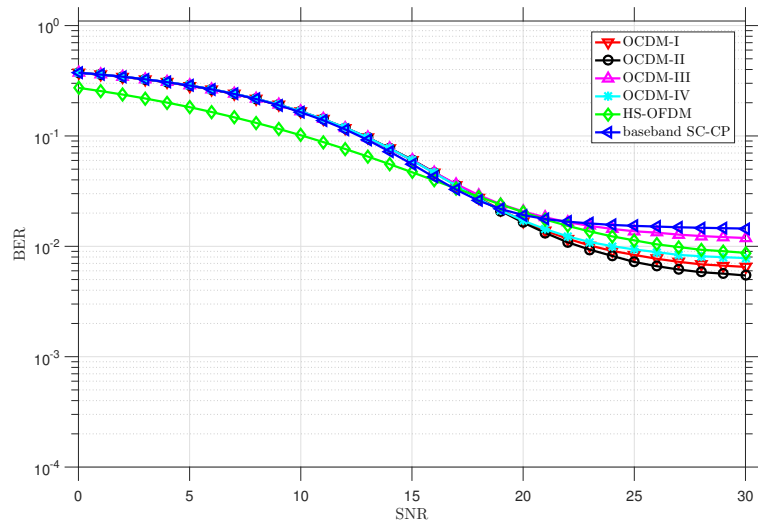
Figure 20: BER performance considering BPSK and PLC channel model corrupted by AWGN: (a)  $L_{cp} = 100\%$  of  $L_1$ ; (b)  $L_{cp} = 50\%$  of  $L_1$ ; (c)  $L_{cp} = 23\%$  of  $L_1$ ; (d)  $L_{cp} = 10\%$  of  $L_1$ .



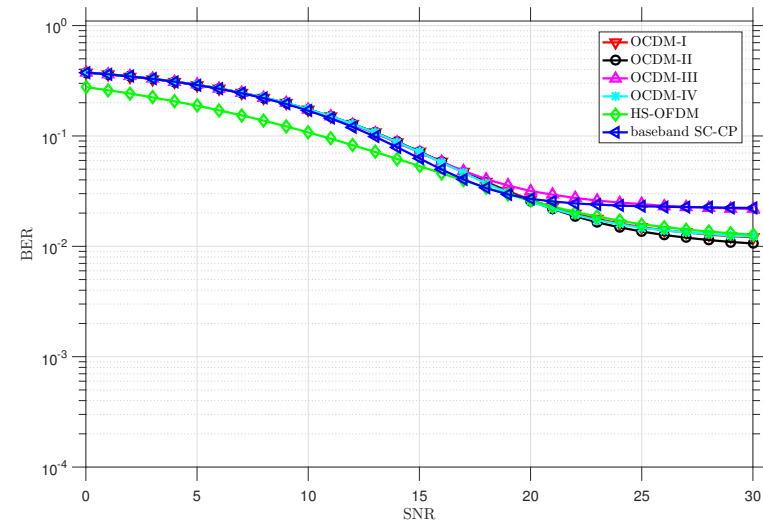
(a)



(b)

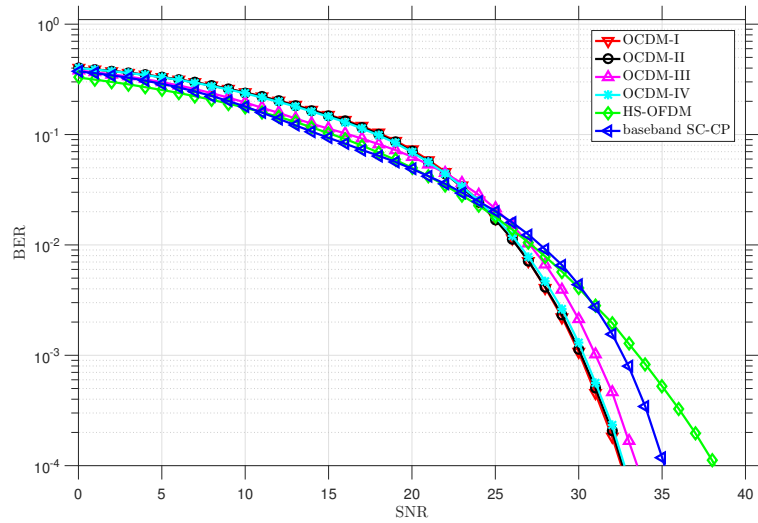


(c)

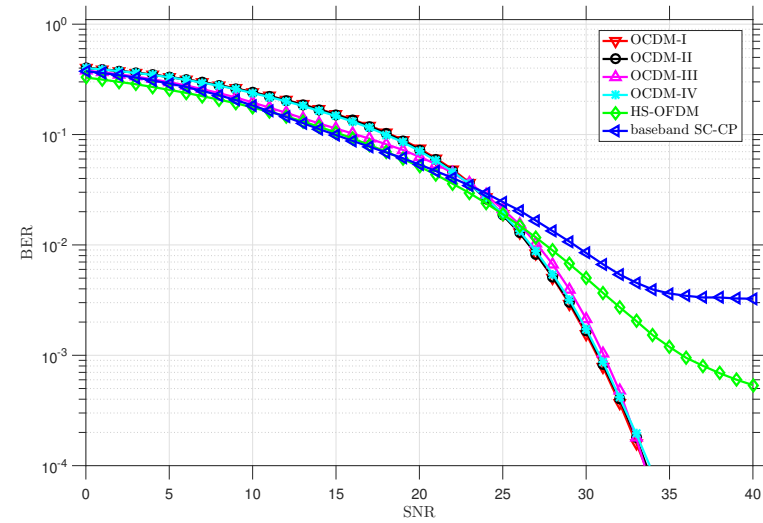


(d)

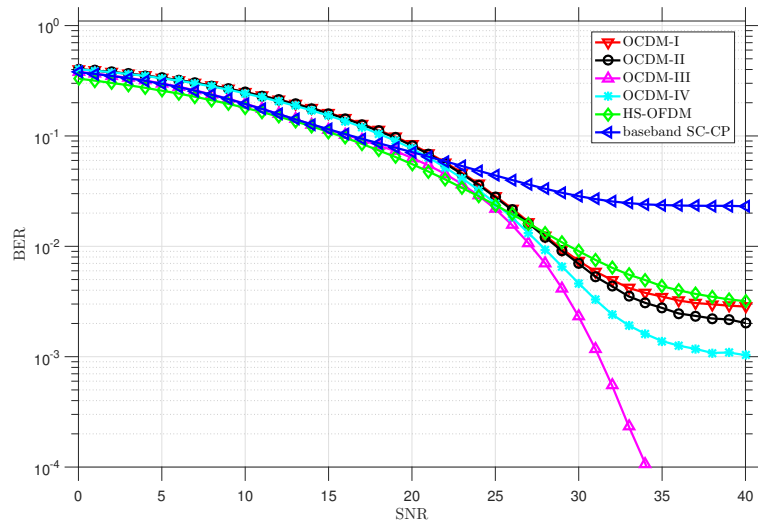
Figure 21: BER performance considering QPSK and PLC channel model corrupted by AWGN: (a)  $L_{cp} = 100\%$  of  $L_1$ ; (b)  $L_{cp} = 50\%$  of  $L_1$ ; (c)  $L_{cp} = 23\%$  of  $L_1$ ; (d)  $L_{cp} = 10\%$  of  $L_1$ .



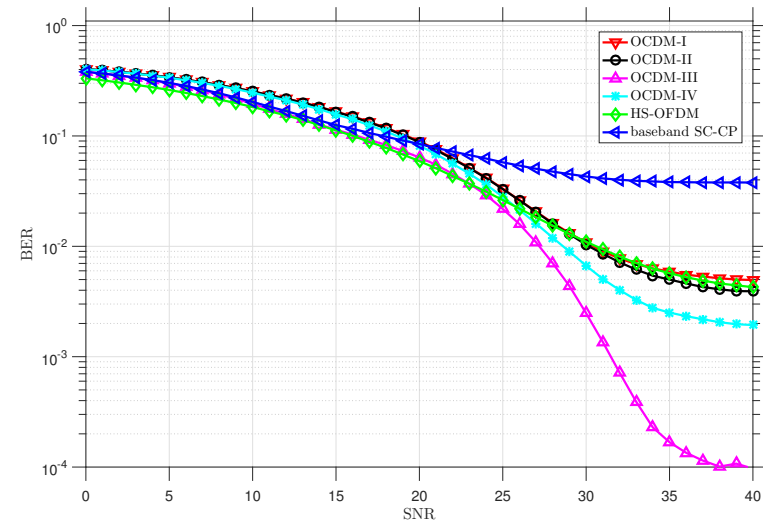
(a)



(b)

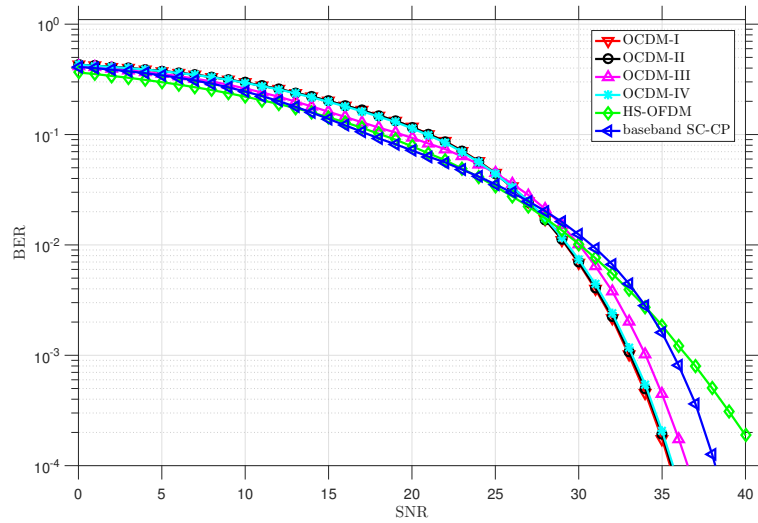


(c)

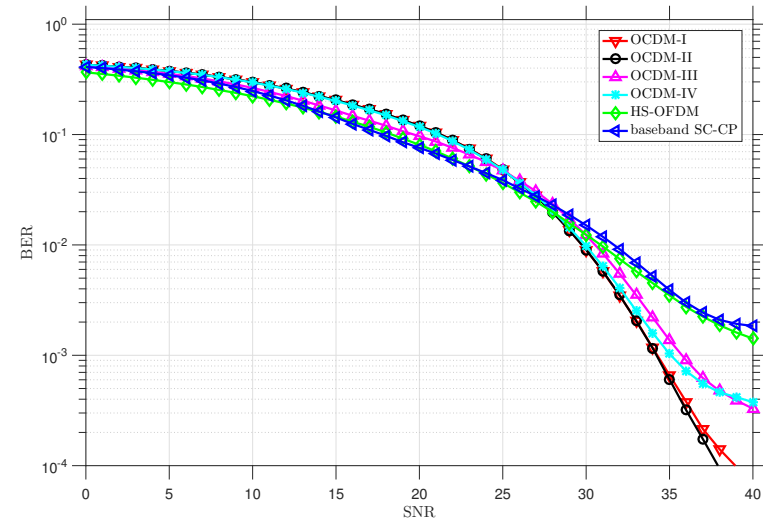


(d)

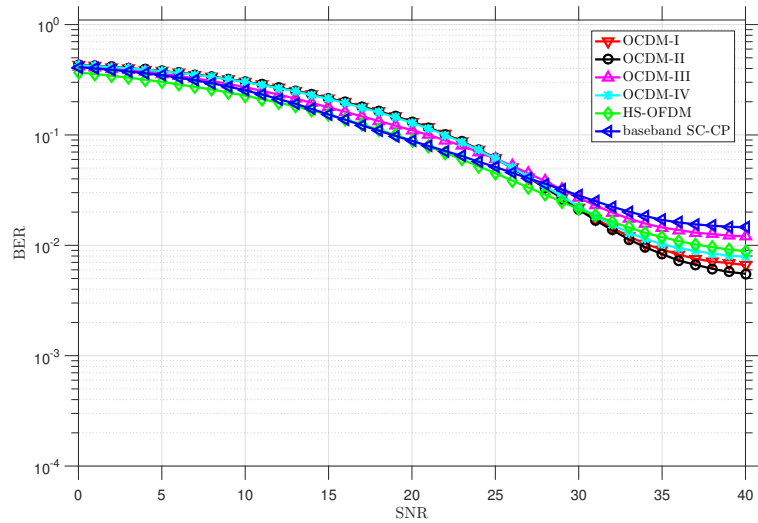
Figure 22: BER performance considering BPSK and PLC channel model corrupted by ABGN: (a)  $L_{cp} = 100\%$  of  $L_1$ ; (b)  $L_{cp} = 50\%$  of  $L_1$ ; (c)  $L_{cp} = 23\%$  of  $L_1$ ; (d)  $L_{cp} = 10\%$  of  $L_1$ .



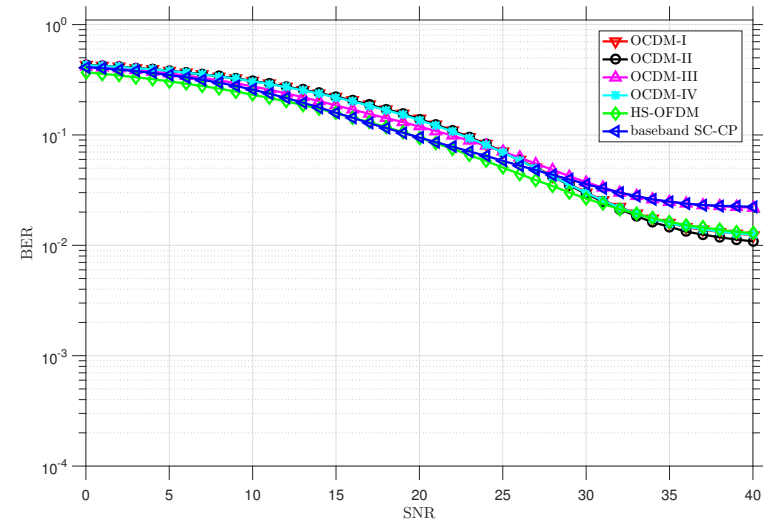
(a)



(b)



(c)



(d)

Figure 23: BER performance considering QPSK and PLC channel model corrupted by ABGN: (a)  $L_{cp} = 100\%$  of  $L_1$ ; (b)  $L_{cp} = 50\%$  of  $L_1$ ; (c)  $L_{cp} = 23\%$  of  $L_1$ ; (d)  $L_{cp} = 10\%$  of  $L_1$ .

### 3.4.2 Multiuser analyses

For these analyses, a four-user system was exercised and the following parameters were considered:  $N = 128$ ,  $S_F = N$  and  $B = 600$  kHz. The PLC channel depicted in Fig. 17 was utilized by each user in order to guarantee a fair performance comparison. Also, Hadamard codes [103] are employed for defining  $\mathbf{k}_j$ . In this section, types I to IV MCp-CDMA refer to the use of types I to IV OCDM, respectively.

The set of plots of Fig. 24 depicts BER performance of user #1 from four-user types I to IV MCp-CDMA schemes, as well as MC-CDMA and SC-CDMA schemes. The PLC channel corrupted by AWGN is utilized in this set. Fig. 24-a depicts the BER performance using BPSK for modulating the input data when  $L_{cp}$  corresponds to 100% of  $L_j$ , i.e, inexistent ISI condition. It is noticed that there is an uniformity in the performance of all schemes considered in the simulation. If a BER level of  $10^{-4}$  is set as reference, the correspondent SNR of each scheme varies from 18.1 dB for the leftmost curve (MC-CDMA) to 18.8 dB for the rightmost curve (type-I MCp-CDMA). This small difference among MCp-CDMA, MC-CDMA, and SC-CDMA reflects clearly the performance similarity promoted by the CDMA portion of each scheme. Fig. 24-b depicts the BER performance using QPSK for modulating the input data when  $L_{cp}$  corresponds to 100% of  $L_j$ . The uniformity in the performance is confirmed if the BER level of  $10^{-4}$  is set as reference. In this case, the correspondent SNR of each scheme varies from 21.3 dB for the leftmost curve (MC-CDMA) to 22.1 dB for the rightmost curve (type-II MCp-CDMA). Observe that this plot requires higher SNR values than Fig. 24-a, which uses BPSK modulation, as expected. Fig. 24-c depicts the BER performance using BPSK as input data with a drastic reduction of  $L_{cp}$ , resulting in 10% of  $L_j$ . The corresponding CIR energy being used for protection against ISI, in this case, is about 13%. This condition allows the performances to vary slightly more compared to the previous plot using BPSK (Fig. 24-a). For a BER level of  $10^{-4}$ , the correspondent SNR of each scheme varies from 18.1 dB for the leftmost curve (SC-CDMA) to 19.9 dB for the rightmost curve (type-III MCp-CDMA), which is a difference of almost 2 dB, confirming the effect of a high ISI, although timid in relation to the single-user situation shown in Subsection 3.4.1. The high ISI condition, however, was not enough to trigger error floor to any simulated multiuser scheme. Fig. 24-d depicts the BER performance using QPSK as input data with high ISI condition ( $L_{cp} = 10\%$  of  $L_j$ ). For a BER level of  $10^{-4}$ , the correspondent SNR of each scheme varies from 21.5 dB for the leftmost curve (MC-CDMA) to 23 dB for the rightmost curve (type-I MCp-CDMA). Also, there is no evidence of error floor to any multiuser scheme addressed in this plot. The performance uniformity and the absence of error floor during high ISI condition are originated from the spreading implemented by the CDMA portion of each multiuser system. The spreading effect performed on the inputted symbols, in this case, overlaps any effect originated from the utilized schemes.

The set of plots of Fig. 25 depicts the BER performance of user #1 from four-user types I to IV MCp-CDMA schemes, as well as MC-CDMA and SC-CDMA schemes. The PLC channel corrupted by ABGN is utilized in this set. Fig. 25-a depicts the BER performance using BPSK as input data when  $L_{cp}$  corresponds to 100% of  $L_j$ , i.e, inexistent ISI condition. If a BER level of  $10^{-4}$  is set as reference, the correspondent SNR of each scheme varies from 31.9 dB for the leftmost curve (type-IV MCp-CDMA) to 33.5 dB for the rightmost curve (type-III MCp-CDMA). The uniformity in the performance of all schemes considered in the simulation occurs again (but with a slight difference among the curves of each scheme due to the effect of the impulsive noise). The impulsive noise tends to stretch the central part of the curves, but in the present case, there is a more attenuated version compared to a similar single-carrier BER performance (Fig. 22-a). In fact, the CDMA spreading is able to absorb part of the impulsive noise effect, which is another benefit of using a CDMA-based scheme. Fig. 25-b depicts the BER performance using QPSK as input data when  $L_{cp}$  corresponds to 100% of  $L_j$ . For a BER level of  $10^{-4}$ , the correspondent SNR of each scheme varies from 35.8 dB for the leftmost curve (type-IV MCp-CDMA) to 36.8 dB for the rightmost curve (type-I MCp-CDMA) and the consistency related to the performance of the curves is maintained. The stretch in the central part of the curves is slightly more pronounced in relation to the previous plot (Fig. 25-a), but it is possible to identify that the present case is a more attenuated version compared to a similar single-carrier BER performance (Fig. 23-a). Fig. 25-c depicts the BER performance using BPSK as input data with a drastic reduction of  $L_{cp}$  resulting in 10% of  $L_j$ . For a BER level of  $10^{-4}$ , the correspondent SNR of each scheme varies from 32.5 dB for the leftmost curve (type-IV MCp-CDMA) to 34.4 dB for the rightmost curve (type-III MCp-CDMA), which is a difference of 1.9 dB, confirming the effect of a high ISI, although much more attenuated than the single-user situation shown in Subsection 3.4.1. No error floor is triggered to any multiuser scheme simulated in this scenario. Fig. 25-d depicts the BER performance using QPSK as input data under high ISI condition ( $L_{cp} = 10\%$  of  $L_j$ ). For a BER level of  $10^{-4}$ , the correspondent SNR of each scheme varies from 35.8 dB for the leftmost curve (type-III MCp-CDMA) to 37.1 dB for the rightmost curve (type-I MCp-CDMA). Once again, the spreading portion of the CDMA overlaps any effect originated from each multiuser system utilized and prevents any occurrence of error floor in a hard scenario like the one pictured in such plot.

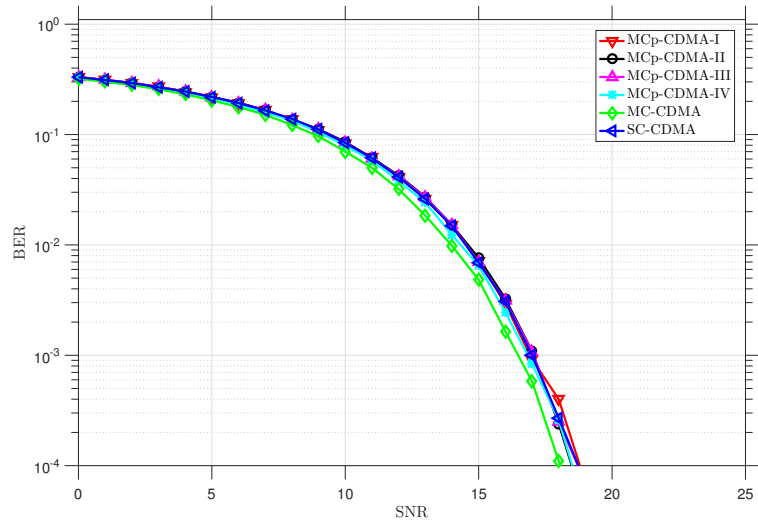
The set of plots of Fig. 26 depicts BER performance for each of the four-users of type-III MCp-CDMA scheme, which holds the least computation complexity among all types, as seen in Subsection 3.3.3. Fig. 26-a portrays the scenario in which AWGN channel model is used with BPSK as input data. In this scenario, each type-III user experiences similar performance in terms of BER. For a BER of  $10^{-4}$ , the average SNR level for each user is nearly 8.3 dB. Fig. 26-b portrays the scenario in which AWGN channel model is used with QPSK as input data. Analogously to the previous situation using BPSK

(Fig. 26-a), the users have similar performance in terms of BER. For a BER of  $10^{-4}$ , the average SNR level from each user is nearly 11.6 dB. Fig. 26-c considers the PLC channel corrupted by AWGN and BPSK modulation as input data. For a BER level of  $10^{-4}$ , the correspondent SNR of each user varies from 17.8 dB for the leftmost curve (user #2) to 18.7 dB for the rightmost curve (user #1). Comparing this scenario with the one depicted in Fig. 26-a, it is possible to identify the distortion promoted by the PLC channel model. Fig. 26-d considers the PLC channel corrupted by AWGN and QPSK modulation as input data. For a BER level of  $10^{-4}$ , the correspondent SNR of each user varies from 21.1 dB for the leftmost curve (user #2) to 22 dB for the rightmost curve (user #1). The distortion promoted by the PLC channel model can be noted comparing this plot with the one depicted in Fig. 26-b (analogous situation using AWGN channel model). Observe that the consistency related to the performance of the curves is maintained also in this set and the small difference among them is connected to the coding sequence that is associated with each user, i.e., how a particular coding sequence interacts with the distortion caused by the channel.

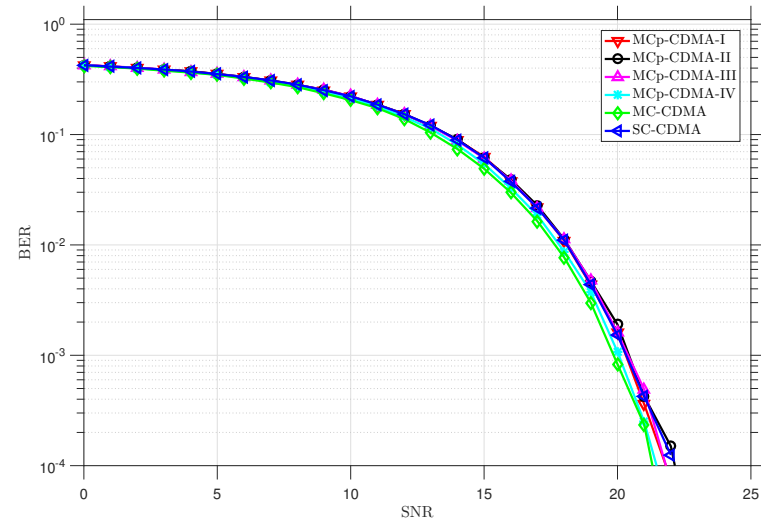
The set of plots of Fig. 27 depicts BER performance for each of the four-users of type-III MCp-CDMA scheme. Fig. 27-a portrays the scenario in which ABGN channel model is used with BPSK as input data. In this scenario, each type-III user experiences similar performance in terms of BER. In this context, for a BER of  $10^{-4}$ , the average SNR level for each user is nearly 23 dB. Comparing Fig. 26-a with Fig. 27-a, it is possible to identify that, although the impulsive noise tends to stretch the central part of the curves, the CDMA spreading is able to absorb part of such impulsive noise effect. Fig. 27-b shows the scenario in which ABGN channel model is used with QPSK as input data. The users have comparable performance in terms of BER (similarly to Fig. 27-a, which uses BPSK as input data). If a BER of  $10^{-4}$  is used as a reference, the average SNR level for each user is nearly 25.5 dB. The stretch in the central part of the curves is slightly more pronounced in relation to the previous plot (Fig. 27-a), but comparing the results from Fig. 26-b and Fig. 27-b, it is possible to identify that the CDMA spreading is able to absorb part of such impulsive noise effect in the present case. Fig. 27-c considers the PLC channel corrupted by ABGN and the BPSK modulation as input data. For a BER level of  $10^{-4}$ , the correspondent SNR for each user varies from 31.8 dB for the leftmost curve (user #2) to 33.5 dB for the rightmost curve (user #1). Comparing this scenario with the one depicted in Fig. 27-a, it is possible to notice the distortion effect promoted by the PLC channel model on the BER performance result. Fig. 27-d considers the PLC channel corrupted by ABGN and the QPSK modulation as input data. If a BER level of  $10^{-4}$  is used as a reference, the correspondent SNR of each user varies from 34.7 dB for the leftmost curve (user #4) to 36 dB for the rightmost curve (user #1). Comparing this scenario with the one depicted in Fig. 27-b, it is possible to observe the distortion effect promoted by the PLC channel model in the BER performance result. Observe that

the PLC channel corrupted by ABGN (Fig. 27-d) requires higher SNR to achieve the same BER as the PLC channel corrupted by AWGN (Fig. 26-d), in a similar scenario, as expected.

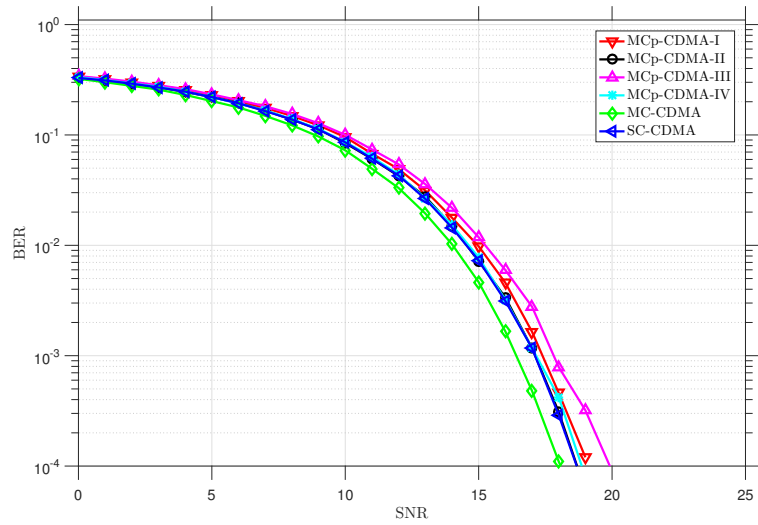
Furthermore, it is interesting to highlight the consistency related to the order in which each user appears in the results shown Figs. 26-c, 26-d, 27-c, and 27-d. Observe that user #2 is associated with leftmost curve and user #1 is associated with rightmost curve in almost all these plots. This behavior indicates that the coding sequence (associated with each user) is the source of such stability and the small difference among the users is related to how a particular coding sequence interacts with the distortion caused by the channel.



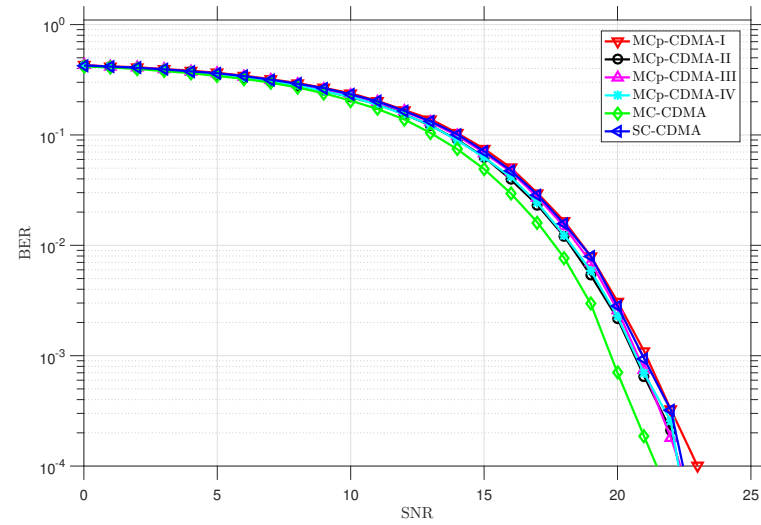
(a)



(b)

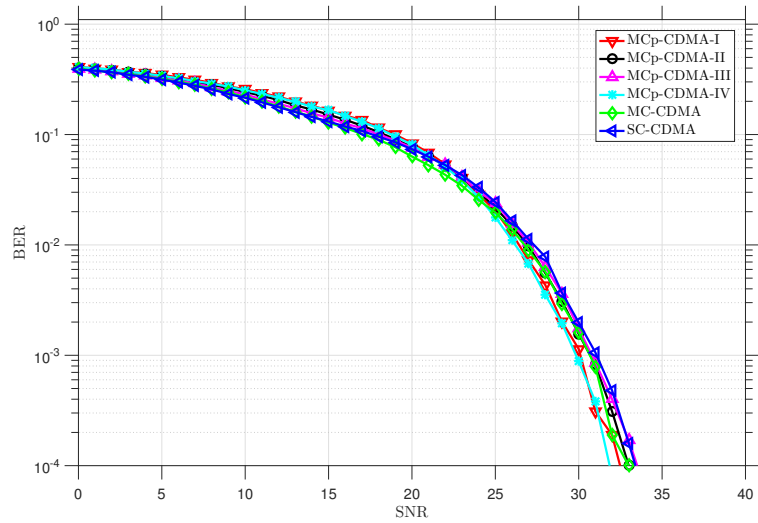


(c)

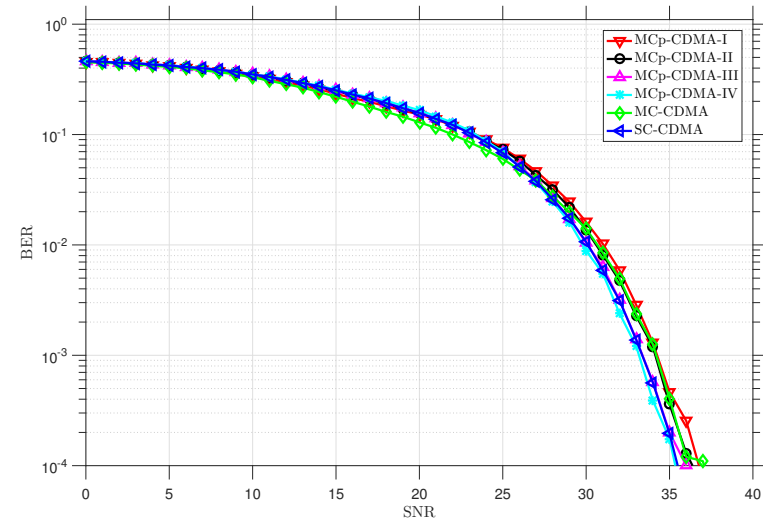


(d)

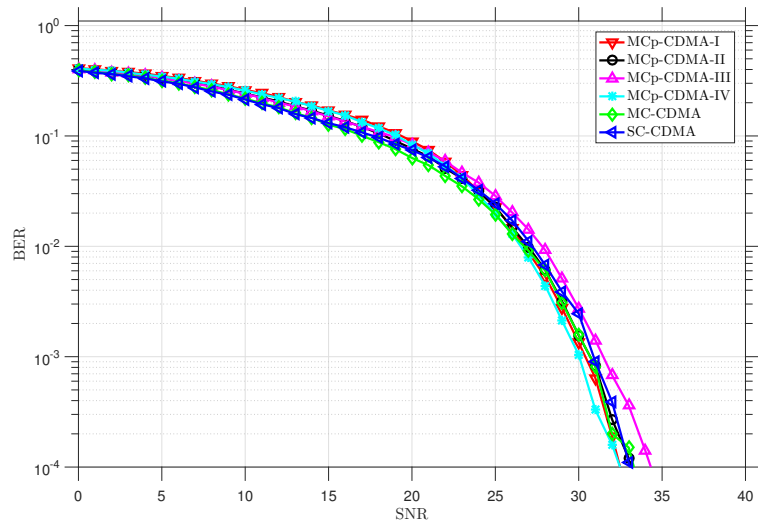
Figure 24: Comparison among MCp-CDMA, MC-CDMA and SC-CDMA Four-user PLC channel+AWGN: (a) BPSK,  $L_{cp} = 100\%$  of  $L_j$ ; (b) QPSK,  $L_{cp} = 100\%$  of  $L_j$ ; (c) BPSK,  $L_{cp} = 10\%$  of  $L_j$ ; (d) QPSK,  $L_{cp} = 10\%$  of  $L_j$ .



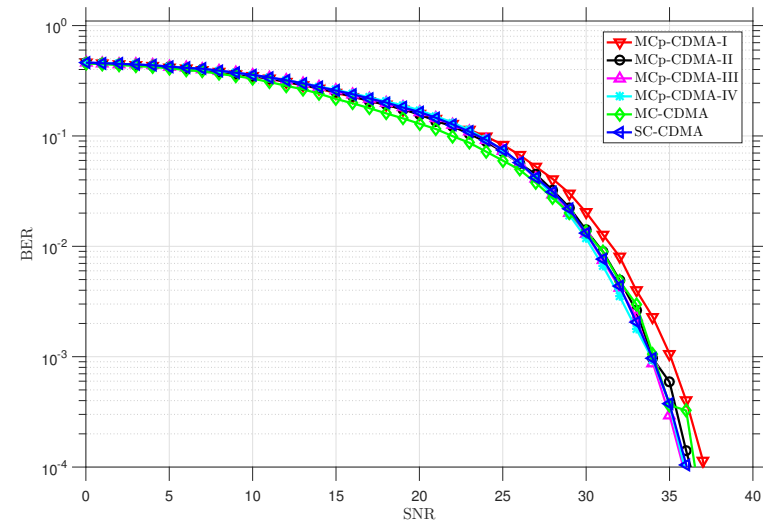
(a)



(b)

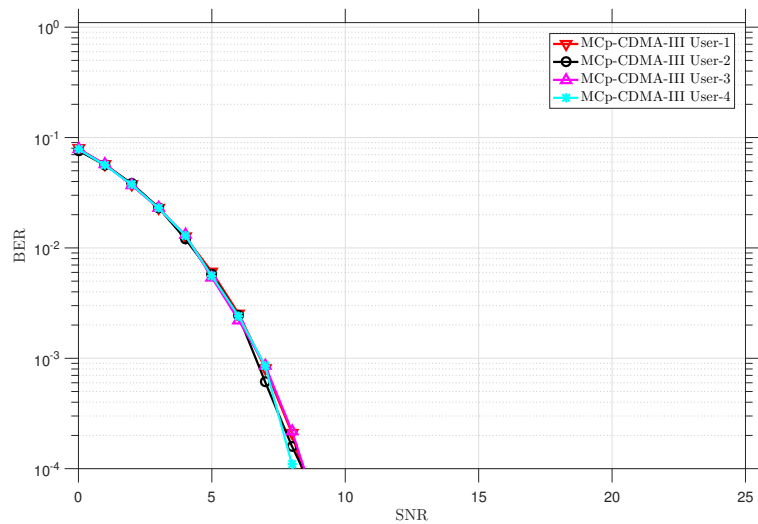


(c)

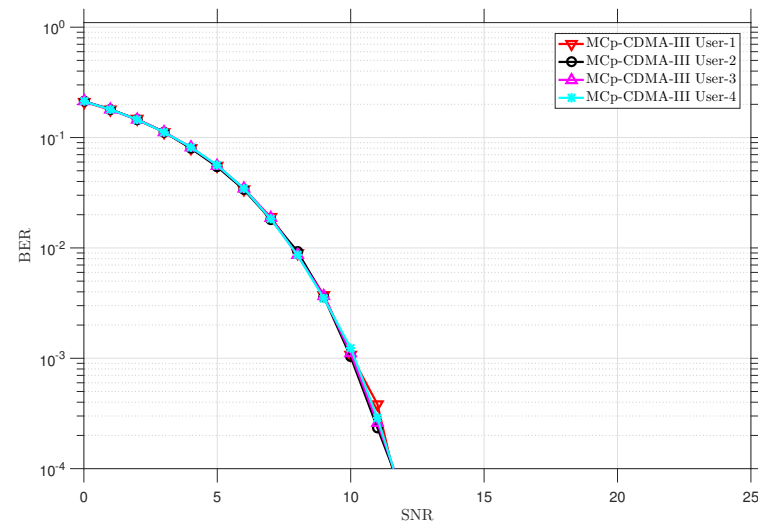


(d)

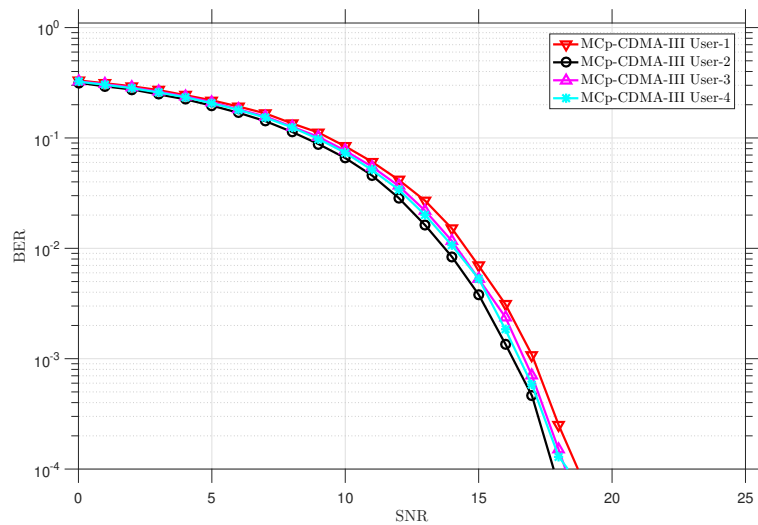
Figure 25: Comparison among MCp-CDMA, MC-CDMA and SC-CDMA Four-user PLC channel+ABGN: (a) BPSK,  $L_{cp} = 100\%$  of  $L_j$ ; (b) QPSK,  $L_{cp} = 100\%$  of  $L_j$ ; (c) BPSK,  $L_{cp} = 10\%$  of  $L_j$ ; (d) QPSK,  $L_{cp} = 10\%$  of  $L_j$ .



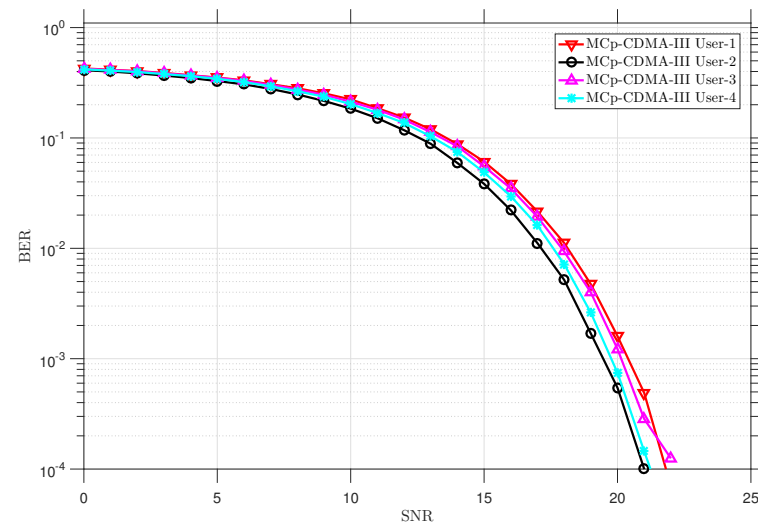
(a)



(b)

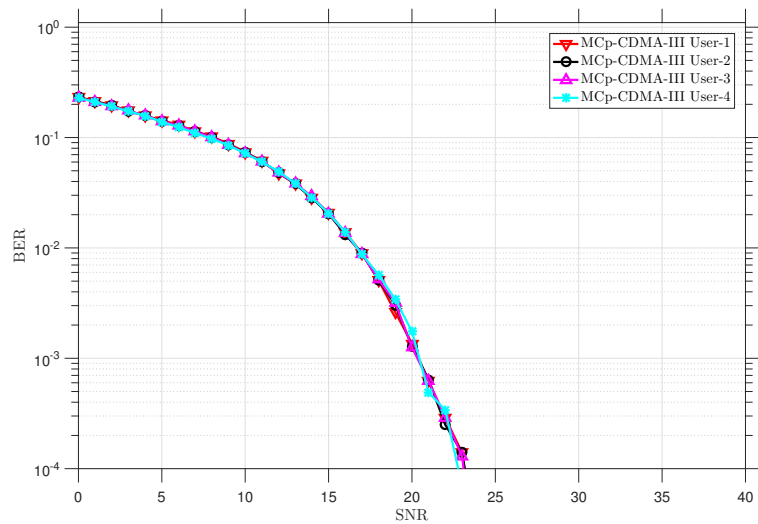


(c)

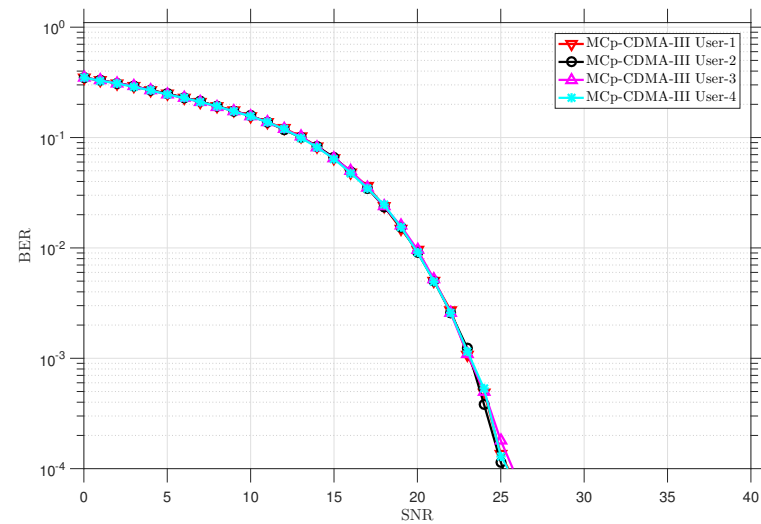


(d)

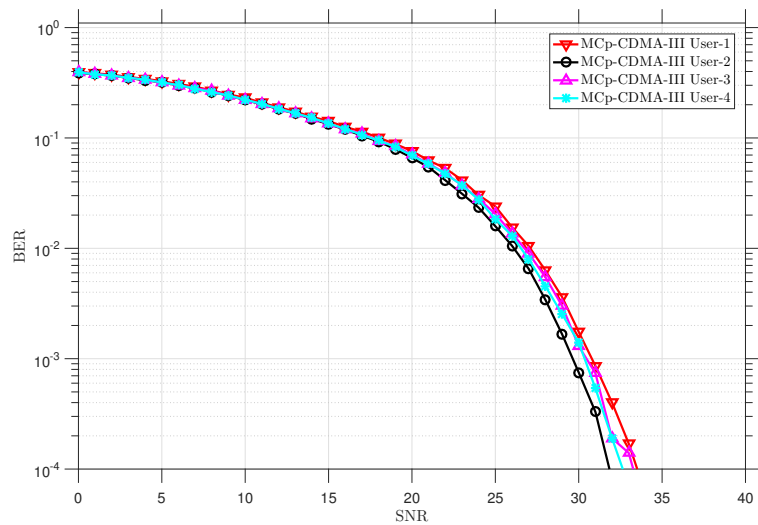
Figure 26: Comparison among each the four users for type-III MCp-CDMA: (a) BPSK and AWGN channel model; (b) QPSK and AWGN channel model; (c) BPSK and PLC channel model corrupted by AWGN; (d) QPSK and PLC channel model corrupted by AWGN.



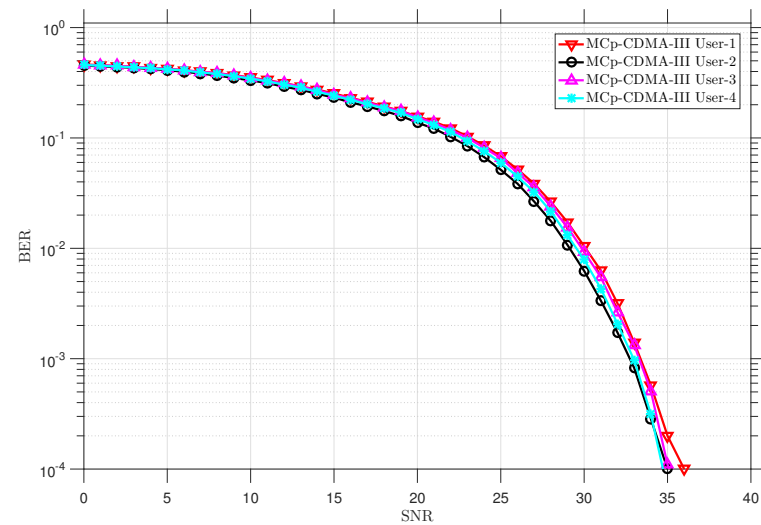
(a)



(b)



(c)



(d)

Figure 27: Comparison among each the four users for type-III MCp-CDMA: (a) BPSK and ABGN channel model; (b) QPSK and ABGN channel model; (c) BPSK and PLC channel model corrupted by ABGN; (d) QPSK and PLC channel model corrupted by ABGN.

## 4 CONCLUSIONS

This thesis discussed important aspects of hybrid PLC/wireless data communication system for SG and IoT applications considering essential drivers and up-to-date aspects of the use of existing technology. Also, it discussed and introduced the employment of a multiuser technique (MCp-CDMA) based on the recent OCDM scheme at the downlink aiming the organization of PLC data communication to serve multiple network nodes.

Chapter 2 showed that the number of consumers connected to a distribution transformer should be economically reasonable considering the number of equipment on the field and the number of consumers served. Furthermore, it was noticed that the implementation of a hybrid PLC/wireless data communication system is very dependent on the configuration of LV outdoor electric power grids and the environment it is immersed in. Furthermore, the environmental influences on PLC and wireless communication were debated and important security aspects from the point of view of a massive-node deployment were discussed. For applications requiring low data rate, the combination of IoT and SG technologies can leverage deployment options and project expansion for alternative configurations, while it maintains the data communication cost as low as possible.

In sequel, Chapter 3 presented a comprehensive analysis of an OCDM-based scheme targeting PLC systems for IoT and SG applications as an alternative to the predominant HS-OFDM scheme. On this subject, it was introduced four types for executing OCDM to allow baseband communication using the not-so-widespread DF<sub>n</sub>T. Among the introduced types, one stands out comparatively to the other ones (type III OCDM) due to its low computational complexity. The principles of CDMA were also explored through its spread/encoding/de-spread/decoding fundamentals. Furthermore, this contribution showed that impulsive noise requires higher SNR values comparatively to the purely Gaussian noise in order to reach similar BER values but when the OCDM scheme is used in a hard and noisy environment, it becomes advantageous, being able to soften the impulsive noise effect, keeping BER in lower levels than the SC-CP scheme if the same SNR is considered. When there is great uncertainty regarding the channel length, the simulations showed that OCDM is more interesting, comparatively to HS-OFDM and SC-CP schemes, allowing the BER results to be the lowest among all schemes, for a given SNR. If the energy associated with the channel length has a drastic reduction, the OCDM performance tends to be closer to the HS-OFDM scheme.

The multiuser analyzes, using an  $S_F$  of 128 demonstrated small performance difference among the considered schemes (types I to IV MCp-CDMA, MC-CDMA, and SC-CDMA). This holds regardless of the ISI level considered in the simulations. In high ISI scenario, any occurrence of error floor is shown in the performed simulations. Finally,

it is possible to observe the stability and consistency of performance related to the results obtained with multiuser simulations. Such behavior is closely connected to the spreading effect performed on the inputted symbols. As a result, any action from the baseband schemes utilized is overlapped.

#### 4.1 FUTURE WORKS

A suggested list of future works are as follows:

- to analyze the effect of reducing the  $S_F$  in the MCp-CDMA scheme and to understand the ideal  $S_F$ , so that the advantages of the OCDM shown in this thesis are evident (when combined with CDMA), in a way that both can balance their contribution to the system performance.
- to expand this thesis towards a hybrid PLC/wireless implementation, analyzing how the interaction between PLC and wireless communication, working together, can influence the overall system performance.

## REFERENCES

- [1] B. Vejlgaard, M. Lauridsen, H. Nguyen, I. Z. Kovacs, P. Mogensen, and M. Sorensen, "Coverage and capacity analysis of sigfox, lora, gprs, and nb-iot," in *2017 IEEE 85th Vehicular Technology Conference (VTC Spring)*, June 2017, pp. 1–5.
- [2] U. Raza, P. Kulkarni, and M. Sooriyabandara, "Low power wide area networks: An overview," *IEEE Communications Surveys Tutorials*, vol. 19, no. 2, pp. 855–873, Secondquarter 2017.
- [3] H. C. Ferreira, L. Lampe, J. Newbury, and T. G. Swart, *Power line communications: theory and applications for narrowband and broadband communications over power lines*. John Wiley, 2010.
- [4] T. R. Oliveira, C. A. G. Marques, W. A. Finamore, S. L. Netto, and M. V. Ribeiro, "A methodology for estimating frequency responses of electric power grids," *J. Control Autom. Elec. Syst.*, vol. 25, no. 6, pp. 720–731, Dec. 2014.
- [5] L. G. S. Costa, A. C. M. Queiroz, B. Adebisi, V. L. R. Costa, and M. V. Ribeiro, "Coupling for power line communication: A survey," *J. of Commun. and Inf. Systems*, vol. 32, no. 1, pp. 8 – 22, 2017.
- [6] R. M. Oliveira, M. S. P. Facina, M. V. Ribeiro, and A. B. Vieira, "Performance evaluation of in-home broadband PLC systems using a cooperative MAC protocol," *Comput. Netw.*, vol. 95, pp. 62–76, Dec. 2015.
- [7] O. A. Gonzalez, J. Urminsky, M. Calvo, and L. de Haro, "Performance analysis of hybrid broadband access technologies using PLC and wi-fi," in *Proc. Int. Conf. on Wireless Netw., Commun. and Mobile Computing*, vol. 1, no. 12, Jun. 2005, pp. 564–569.
- [8] T. Holden and J. Yazdani, "Hybrid security for hybrid vehicles exploring smart grid technology, powerline and wireless communication," in *Proc. IEEE PES Int. Conf. and Exhibition on Innov. Smart Grid Technol.*, Dec. 2011, pp. 1–5.
- [9] A. Cataliotti *et al.*, "Experimental evaluation of an hybrid communication system architecture for smart grid applications," in *Proc. IEEE Int. Workshop on Applied Measurements for Power Systems*, Sep. 2015, pp. 96–101.
- [10] P. Kiedrowski, B. Boryna, and T. Marciniak, "Last-mile smart grid communications based on hybrid technology as a reliable method of data acquisition and distribution," *Rynek Energii*, pp. 127–132, Feb. 2013.
- [11] J. Mafra, M. Hosami, L. Freitas, M. Martinelli, and A. Almeida, "Hybrid communication module - motivations, requirements, challenges and implementations," in *Proc. IEEE PES Innov. Smart Grid Technol. Latin Amer.*, Oct. 2015, pp. 25–29.
- [12] S. W. Lai and G. G. Messier, "Using the wireless and PLC channels for diversity," *IEEE Trans. Commun.*, vol. 60, no. 12, pp. 3865–3875, Dec. 2012.
- [13] M. Sayed and N. Al-Dhahir, "Narrowband-PLC/wireless diversity for smart grid communications," in *Proc. IEEE Global Commun. Conf.*, Dec. 2014, pp. 2966–2971.

- [14] S. W. Lai and G. G. Messier, "The wireless/power-line diversity channel," in *Proc. IEEE Int. Conf. on Commun.*, May. 2010, pp. 1–5.
- [15] —, "System and method for providing a wireless/power-line diversity communications channel," Nov. 24 2011, US Patent 8861574.
- [16] J. H. Lee and Y. H. Kim, "Diversity relaying for parallel use of power-line and wireless communication networks," *IEEE Trans. Power Del.*, vol. 29, no. 3, pp. 1301–1310, June 2014.
- [17] A. Mathur, M. Bhatnagar, and B. Panigrahi, "Performance of a dual-hop wireless-powerline mixed cooperative system," in *Proc. Int. Conf. on Advanced Technologies for Commun.*, Oct. 2016, pp. 401–406.
- [18] S. Galli, A. Scaglione, and Z. Wang, "For the grid and through the grid: The role of power line communications in the smart grid," *Proc. IEEE*, vol. 99, no. 6, pp. 998–1027, June 2011.
- [19] F. A. Santos, L. M. F. D. Silveira, D. Fernandes, L. de M. B. A. Dib, F. P. V. D. Campos, and M. V. Ribeiro, "Integration of a smart meter with the brazilian broadband plc system," in *XXXIII Simposio Brasileiro de Telecomunicacoes (SBrT 2015)*, 2015.
- [20] A. N. Milioudis, G. T. Andreou, and D. P. Labridis, "Enhanced protection scheme for smart grids using power line communications techniques - part i: Detection of high impedance fault occurrence," *IEEE Trans. on Smart Grid*, vol. 3, no. 4, pp. 1621–1630, Dec 2012.
- [21] —, "Enhanced protection scheme for smart grids using power line communications techniques - part ii: Location of high impedance fault position," *IEEE Trans. on Smart Grid*, vol. 3, no. 4, pp. 1631–1640, Dec 2012.
- [22] L. T. Berger, A. Schwager, and J. J. Escudero-Garzas, "Power line communications for smart grid applications," *J. of Electr. and Comput. Eng.*, vol. 2013, pp. 1–16, 2013.
- [23] S. Galli and T. Lys, "Next generation narrowband (under 500 khz) power line communications standards," *China Commun.*, vol. 12, no. 3, pp. 1–8, Mar. 2015.
- [24] A. A. Amarsingh, H. A. Latchman, and D. Yang, "Narrowband power line communications: Enabling the smart grid," *IEEE Potentials*, vol. 33, no. 1, pp. 16–21, Jan. 2014.
- [25] H. A. Foudeh and A. S. Mokhtar, "Automated meter reading and advanced metering infrastructure projects," in *Proc. Jordanian Int. Electr. and Electronics Eng. Conf.*, Oct. 2015, pp. 1–6.
- [26] Z. Han, D. Niyato, W. Saad, T. Başar, and A. Hjørungnes, *Game Theory in Wireless and Communication Networks: Theory, Models, and Applications*. Cambridge University Press, 2012.
- [27] P. Cheng, H. Zhang, and J. Chen, *Cybersecurity for Industrial Control Systems*. CRC Press, 2016.

- [28] J. Petajajarvi, K. Mikhaylov, A. Roivainen, T. Hanninen, and M. Pettissalo, "On the coverage of lpwans: range evaluation and channel attenuation model for lora technology," in *Proc. Int. Conf. on ITS Telecommun.*, Dec. 2015, pp. 55–59.
- [29] M. Y. Zhai, "Transmission characteristics of low-voltage distribution networks in china under the smart grids environment," *IEEE Trans. Power Del.*, vol. 26, no. 1, pp. 173–180, Jan. 2011.
- [30] L. Förstel and L. Lampe, "Grid diagnostics: Monitoring cable aging using power line transmission," in *2017 Proc. IEEE Int. Symp. Power Line Commun. Appl.*, April 2017, pp. 1–6.
- [31] G. R. Colen, C. A. G. Marques, T. R. Oliveira, F. P. V. de Campos, and M. V. Ribeiro, "Measurement setup for characterizing low-voltage and outdoor electric distribution grids for PLC systems," in *Proc. PES Conf. Innov. Smart Grid Technol. Latin Amer.*, Apr. 2013, pp. 1–5.
- [32] T. R. Oliveira, A. A. M. Picorone, S. L. Netto, and M. V. Ribeiro, "Characterization of brazilian in-home power line channels for data communication," *Electric Power Systems Research*, vol. 150, pp. 188–197, 2017.
- [33] M. Zimmermann and K. Dostert, "A multipath model for the power line channel," *IEEE Trans. Commun.*, vol. 50, no. 4, pp. 553–559, Apr. 2002.
- [34] G. R. Colen, L. G. de Oliveira, A. J. H. Vinck, and M. V. Ribeiro, "A spectral compressive resource allocation technique for PLC systems," *IEEE Trans. Commun.*, vol. 65, no. 2, pp. 816–826, Feb. 2017.
- [35] N. Qasem and S. R., "Frequency selective wall for enhancing wireless signal in indoor environments," in *Proc. Loughborough Antennas Propag. Conf.*, Nov. 2009, pp. 573–576.
- [36] —, "Parametric studies in enhancing indoor wireless communication system via environmental modification," in *Proc. Antennas and Propag. Conf.*, Nov. 2012, pp. 1–4.
- [37] L. Xie, Y. Mo, and B. Sinopoli, "Integrity data attacks in power market operations," *IEEE Trans. on Smart Grid*, vol. 2, no. 4, pp. 659–666, Dec 2011.
- [38] Y. Yang, L. Wu, G. Yin, L. Li, and H. Zhao, "A survey on security and privacy issues in internet-of-things," *IEEE Internet of Things J.*, vol. PP, no. 99, pp. 1–1, 2017.
- [39] W. Trappe, R. Howard, and R. S. Moore, "Low-energy security: Limits and opportunities in the internet of things," *IEEE Security Privacy*, vol. 13, no. 1, pp. 14–21, Jan 2015.
- [40] S. A. Salami, J. Baek, K. Salah, and E. Damiani, "Lightweight encryption for smart home," in *2016 Int. Conf. on Availability, Reliability and Security*, Aug 2016, pp. 382–388.
- [41] I. Andrea, C. Chrysostomou, and G. Hadjichristofi, "Internet of things: Security vulnerabilities and challenges," in *2015 IEEE Symp. on Comput. and Commun.*, July 2015, pp. 180–187.

- [42] R. R. Mohassel, A. S. Fung, F. Mohammadi, and K. Raahemifar, "A survey on advanced metering infrastructure and its application in smart grids," in *Proc. IEEE Canadian Conf. on Electr. and Comput. Eng.*, Dec. 2014, pp. 1–8.
- [43] A. Molina-Markham *et al.*, "Private memoirs of a smart meter," in *Proc. IEEE Canadian Conf. on Electr. and Comput. Eng.*, Nov. 2010, pp. 61–66.
- [44] *Cyber Intelligence Section: Smart grid electric meters altered to steal electricity*, accessed in May 2016. [Online]. Available: <https://krebsonsecurity.com/2012/04/fbi-smart-meter-hacks-likely-to-spread>
- [45] T&D World Magazine, *Malta Discovers Electricity Theft from Altered Smart Meters*, accessed in May 2016. [Online]. Available: <http://www.tdworld.com/node/30142>
- [46] R. A. D. Faria, K. V. O. Fonseca, B. Schneider, and S. K. Nguang, "Collusion and fraud detection on electronic energy meters - a use case of forensics investigation procedures," in *Proc. IEEE Security and Privacy Workshops*, 2014, pp. 65–68.
- [47] A. Al-Ali and R. Aburukba, "Role of internet of things in the smart grid," *Technol. J. of Comput. and Commun.*, vol. 3, pp. 229–233, May 2015.
- [48] J. H. Ziegeldorf, O. G. Morchon, and K. Wehrle, "Privacy in the internet of things: threats and challenges," *Security and Commun. Netw.*, vol. 7, pp. 2728–2742, Dec. 2014.
- [49] N. Cam-Winget, A. R. Sadeghi, and Y. Jin, "Invited: Can IoT be secured: Emerging challenges in connecting the unconnected," in *Proc. ACM/EDAC/IEEE Design Automation Conf.*, Jun. 2016, pp. 1–6.
- [50] E. Ronen and A. Shamir, "Extended functionality attacks on IoT devices: The case of smart lights," in *Proc. IEEE European Symp. on Security and Privacy*, 2016, pp. 3–12.
- [51] V. Gungor and F. Lambert, "A survey on communication networks for electric system automation," *Comput. Netw.*, vol. 50, no. 7, pp. 877 – 897, 2006.
- [52] L. Atzori, A. Iera, and G. Morabito, "The internet of things: A survey," *Comput. Netw.*, vol. 54, no. 15, pp. 2787–2805, 2010.
- [53] S. K. Viswanath, C. Yuen, W. Tushar, W. T. Li, C. K. Wen, K. Hu, C. Chen, and X. Liu, "System design of the internet of things for residential smart grid," *IEEE Wireless Commun.*, vol. 23, no. 5, pp. 90–98, Oct. 2016.
- [54] R. Xu, R. Wang, Z. Guan, L. Wu, J. Wu, and X. Du, "Achieving efficient detection against false data injection attacks in smart grid," *IEEE Access*, vol. 5, pp. 13 787–13 798, 2017.
- [55] S. Persia and L. Rea, "Next generation m2m cellular networks: Lte-mtc and nb-iot capacity analysis for smart grids applications," in *2016 AEIT Int. Annual Conf.*, Oct. 2016, pp. 1–6.

- [56] Internet Society, *The Internet of Things: An Overview*, accessed in May 2016. [Online]. Available: <http://www.internetsociety.org/sites/default/files/ISOC-IoT-Overview-20151022.pdf>
- [57] T. R. Oliveira, C. A. G. Marques, M. S. Pereira, S. L. Netto, and M. V. Ribeiro, "The characterization of hybrid plc-wireless channels: A preliminary analysis," in *2013 IEEE 17th International Symposium on Power Line Communications and Its Applications*, March 2013, pp. 98–102.
- [58] T. R. Oliveira, F. J. A. Andrade, A. M. Picorone, H. A. Latchman, S. L. Netto, and M. V. Ribeiro, "Characterization of hybrid communication channel in indoor scenario," *J. of Communication and information Systems*, vol. 31, no. 1, pp. 224–235, Dec. 2016.
- [59] V. Fernandes, M. L. Filomeno, W. A. Finamore, and M. V. Ribeiro, "An investigation on narrow band PLC-wireless parallel channel capacity," in *Proc. XXXIV Simpósio Brasileiro de Telecomunicações*, Sep. 2016, pp. 834–838.
- [60] M. V. Ribeiro, F. P. V. Campos, G. R. Colen, H. V. Schettino, D. Fernandes, L. M. Sirimarco, V. Fernandes, and A. A. M. Picorone, "A novel power line communication system for outdoor electric power grids," in *2015 IEEE International Symposium on Power Line Communications and Its Applications (ISPLC)*, March 2015, pp. 228–233.
- [61] F. da Costa Pinto, F. S. O. Scoralick, F. P. V. de Campos, Z. Quan, and M. V. Ribeiro, "A low cost ofdm based modulation schemes for data communication in the passband frequency," in *2011 IEEE International Symposium on Power Line Communications and Its Applications*, April 2011, pp. 424–429.
- [62] L. G. de Oliveira, G. R. Colen, M. V. Ribeiro, and A. J. H. Vinck, "Narrow-band interference error correction in coded ofdm-based plc systems," in *2016 International Symposium on Power Line Communications and its Applications (ISPLC)*, March 2016, pp. 13–18.
- [63] C. A. G. Marques, F. P. V. de Campos, T. R. Oliveira, A. S. Menezes, and M. V. Ribeiro, "Analysis of a hybrid ofdm synchronization algorithm for power line communication," in *ISPLC2010*, March 2010, pp. 44–49.
- [64] M. V. Ribeiro, R. R. Lopes, J. M. T. Romano, and C. A. Duque, "Impulse noise mitigation based on computational intelligence for improved bit rate in plc-dmt," *IEEE Transactions on Power Delivery*, vol. 21, no. 1, pp. 94–101, Jan 2006.
- [65] L. de M. B. A. Dib, V. Fernandes, M. de L. Filomeno, and M. V. Ribeiro, "Hybrid PLC/wireless communication for smart grids and Internet of Things applications," *IEEE Internet Things J.*, Oct. 2017, accepted for publication.
- [66] D. P. F. Möller and H. Vakilzadian, "Ubiquitous networks: Power line communication and internet of things in smart home environments," in *IEEE International Conference on Electro/Information Technology*, June 2014, pp. 596–601.
- [67] K. F. Trillingsgaard and P. Popovski, "Downlink transmission of short packets: Framing and control information revisited," *IEEE Transactions on Communications*, vol. 65, no. 5, pp. 2048–2061, May 2017.

- [68] Z. Yuan, G. Yu, W. Li, Y. Yuan, X. Wang, and J. Xu, in *2016 IEEE 83rd Vehicular Technology Conference (VTC Spring)*.
- [69] S. Choochotkaew, H. Yamaguchi, T. Higashino, and M. Shibuya, "Requirement-based prioritization system in multi-user iot," in *2015 IEEE 2nd World Forum on Internet of Things (WF-IoT)*, Dec 2015, pp. 122–127.
- [70] A. Barbato, A. Capone, G. Carello, M. Delfanti, M. Merlo, and A. Zaminga, "House energy demand optimization in single and multi-user scenarios," in *2011 IEEE International Conference on Smart Grid Communications (SmartGridComm)*, Oct 2011, pp. 345–350.
- [71] M. V. Ribeiro, G. R. Colen, F. V. p. De Campos, Z. Quan, and H. V. Poor, "Clustered-orthogonal frequency division multiplexing for power line communication: when is it beneficial?" *IET Communications*, vol. 8, no. 13, pp. 2336–2347, September 2014.
- [72] Y. H. Ma, P. L. So, and E. Gunawan, "Comparison of cdma and ofdm systems for broadband power line communications," *IEEE Transactions on Power Delivery*, vol. 23, no. 4, pp. 1876–1885, Oct 2008.
- [73] X. Zhang, Y. C. Liang, and J. Fang, "Bayesian learning based multiuser detection for m2m communications with time-varying user activities," in *2017 IEEE International Conference on Communications (ICC)*, May 2017, pp. 1–6.
- [74] M. V. Ribeiro, F. P. V. Campos, G. R. Colen, H. V. Schettino, D. Fernandes, L. M. Sirimarco, V. Fernandes, and A. A. M. Picorone, "A novel power line communication system for outdoor electric power grids," in *2015 IEEE International Symposium on Power Line Communications and Its Applications (ISPLC)*, March 2015, pp. 228–233.
- [75] C. F. Teng, C. C. Liao, H. Y. Cheng, and A. Y. A. Wu, "Reliable compressive sensing (cs)-based multi-user detection with power-based zadoff-chu sequence design," in *2017 IEEE International Workshop on Signal Processing Systems (SiPS)*, Oct 2017, pp. 1–5.
- [76] S. Hara and R. Prasad, "Overview of multicarrier cdma," *IEEE Communications Magazine*, vol. 35, no. 12, pp. 126–133, Dec 1997.
- [77] W. Ye and P. K. Varshney, "An equicorrelation-based multiuser communication scheme for ds-cdma systems," *IEEE Transactions on Communications*, vol. 51, no. 1, pp. 43–47, Jan 2003.
- [78] L. Hanzo, M. Münster, B. Choi, and T. Keller, *OFDM and MC-CDMA for Broadband Multi-user Communications, WLANs and Broadcasting*. John Wiley & Sons, May 2003.
- [79] L. L. Yang, "A zero-forcing multiuser transmitter preprocessing scheme for downlink communications," *IEEE Transactions on Communications*, vol. 56, no. 6, pp. 862–865, June 2008.

- [80] A. Chouly, A. Brajal, and S. Jourdan, "Orthogonal multicarrier techniques applied to direct sequence spread spectrum cdma systems," in *Global Telecommunications Conference, 1993, including a Communications Theory Mini-Conference. Technical Program Conference Record, IEEE in Houston. GLOBECOM '93., IEEE*, Nov 1993, pp. 1723–1728 vol.3.
- [81] K.-C. Chen and S.-T. Wu, "A programmable architecture for ofdm-cdma," *IEEE Communications Magazine*, vol. 37, no. 11, pp. 76–82, Nov 1999.
- [82] W. M. Jang, L. Nguyen, and P. Bidarkar, "Multiple access and inter-carrier interference in ofdm-cdma with random sequences," *Journal of Communications and Networks*, vol. 7, no. 1, pp. 21–28, March 2005.
- [83] C. C. Kuo, W. H. Sheen, C. J. Chang, and C. L. Hsiao, "On the transmitter-based preprocessing for 2-d ofdm-cdma forward-link systems over time-varying rayleigh fading channels," *IEEE Transactions on Vehicular Technology*, vol. 57, no. 3, pp. 1968–1974, May 2008.
- [84] K. M. Rabie and E. Alsusae, "On improving communication robustness in plc systems for more reliable smart grid applications," *IEEE Transactions on Smart Grid*, vol. 6, no. 6, pp. 2746–2756, Nov 2015.
- [85] Y.-H. You, W.-G. Jeon, J.-H. Paik, and H.-K. Song, "A simple construction of ofdm-cdma signals with low peak-to-average power ratio," *IEEE Transactions on Broadcasting*, vol. 49, no. 4, pp. 403–407, Dec 2003.
- [86] K. Zheng, G. Zeng, and W. Wang, "Performance analysis for ofdm-cdma with joint frequency-time spreading," *IEEE Transactions on Broadcasting*, vol. 51, no. 1, pp. 144–148, March 2005.
- [87] X. Wang, M. Fei, and X. Li, "Performance of chirp spread spectrum in wireless communication systems," in *2008 11th IEEE Singapore International Conference on Communication Systems*, Nov 2008, pp. 466–469.
- [88] S. Wang, W. Zou, X. Long, and J. Chen, "Influence of phase noise on measurement range in optical pulse compression reflectometry," in *2015 Opto-Electronics and Communications Conference (OECC)*, June 2015, pp. 1–3.
- [89] X. Ouyang and J. Zhao, "Orthogonal chirp division multiplexing," *IEEE Transactions on Communications*, vol. 64, no. 9, pp. 3946–3957, Sept 2016.
- [90] —, "Orthogonal chirp division multiplexing for coherent optical fiber communications," *Journal of Lightwave Technology*, vol. 34, no. 18, pp. 4376–4386, Sept 2016.
- [91] P. J. Bouvet, Y. Auffret, and C. Aubry, "On the analysis of orthogonal chirp division multiplexing for shallow water underwater acoustic communication," in *OCEANS 2017 - Aberdeen*, June 2017, pp. 1–5.
- [92] X. Ouyang, C. Antony, F. Gunning, H. Zhang, and Y. L. Guan, "Discrete fresnel transform and its circular convolution." *CoRR*, vol. abs/1510.00574, 2015. [Online]. Available: <http://dblp.uni-trier.de/db/journals/corr/corr1510.html#OuyangAGZG15>

- [93] B. Davies, *Integral transforms and their applications*, ser. Applied mathematical sciences. Springer-Verlag, 1978.
- [94] J. Cioffi, *A Multicarrier Primer*, accessed in Aug 2017. [Online]. Available: <http://www.stanford.edu/group/cioffi/documents/multicarrier.pdf>
- [95] W. C. Y. Lee, “Overview of cellular cdma,” *IEEE Transactions on Vehicular Technology*, vol. 40, no. 2, pp. 291–302, May 1991.
- [96] K. S. Gilhousen, I. M. Jacobs, R. Padovani, A. J. Viterbi, L. A. Weaver, and C. E. Wheatley, “On the capacity of a cellular cdma system,” *IEEE Transactions on Vehicular Technology*, vol. 40, no. 2, pp. 303–312, May 1991.
- [97] W. Liu, M. Sigle, and K. Dostert, “Channel characterization and system verification for narrowband power line communication in smart grid applications,” *IEEE Communications Magazine*, vol. 49, no. 12, pp. 28–35, December 2011.
- [98] V. Fernandes, W. A. Finamore, M. V. Ribeiro, N. Marina, and J. Karamachoski, “Bernoulli-gaussian distribution with memory as a model for power line communication noise,” in *Proc. XXXV Simpósio Brasileiro de Telecomunicações*, Sep. 2017.
- [99] V. Arrizón, J. G. Ibarra, and J. O.-C. neda, “Matrix formulation of the fresnel transform of complex transmittance gratings,” *J. Opt. Soc. Am. A*, vol. 13, no. 12, pp. 2414–2422, Dec 1996.
- [100] F. A. La-Gatta, M. V. Ribeiro, A. P. Legg, and R. Machado, “Coded cp-sc communication scheme for outdoor power line communications,” in *ISPLC2010*, March 2010, pp. 160–165.
- [101] M. V. Ribeiro, M. B. Loiola, and R. R. Lopes, “Turbo-fuzzy equalization for single-carrier power line channels,” in *2007 IEEE International Symposium on Power Line Communications and Its Applications*, March 2007.
- [102] *IEEE Standard for Low Frequency (less than 500 kHz) Narrow Band Power Line Communications for Smart Grid Application*, IEEE Std. 1901.2, 2013.
- [103] E. H. Dinan and B. Jabbari, “Spreading codes for direct sequence cdma and wide-band cdma cellular networks,” *IEEE Communications Magazine*, vol. 36, no. 9, pp. 48–54, Sep 1998.

## Appendix A – SPREADING FORMS FOR OCDM, OFDM AND SC-CP SCHEMES

Following the OCDM scheme, it is established that the DF<sub>n</sub>T spreads the transmitted OCDM symbols in a very particular form. Fig. 28-a depicts the spectrogram of the sub-chirp #130 from a 256-length OCDM symbol that is supposed to be transmitted through a passband channel [89]. Notice that the frequency of such sub-chirp decays linearly along with time, characterizing a down-chirp process. For comparison purposes, Fig. 28-b depicts the spectrogram of sub-carrier #165 from a 256-length symbol associated with an OFDM scheme, while Fig. 28-c depicts the spectrogram of sub-symbol #30 from a 256-length symbol associated with the SC-CP scheme. Comparing such OCDM spectrogram with the OFDM and SC-CP ones, it can be seen that the way the OCDM scheme spreads the frequency over time can be seen as an intermediate fashion between OFDM and SC-CP.

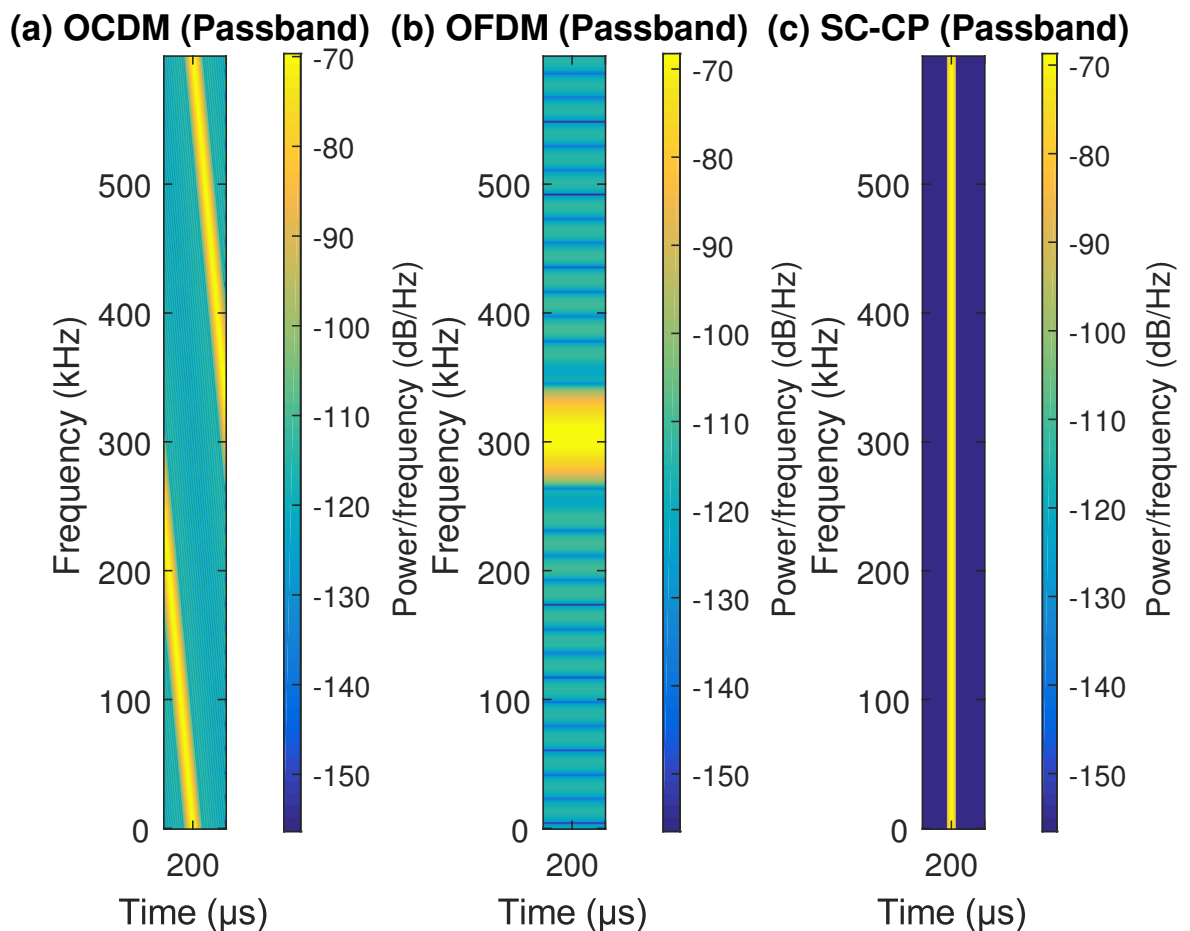


Figure 28: (a) Sub-chirp #130 spectrogram from a 256-length symbol of an OCDM scheme. (b) Sub-carrier #165 spectrogram from a 256-length symbol of an OFDM scheme. (c) Sub-symbol #130 spectrogram from a 256-length symbol of a SC-CP scheme. All indicated schemes employ QPSK modulation as input data.

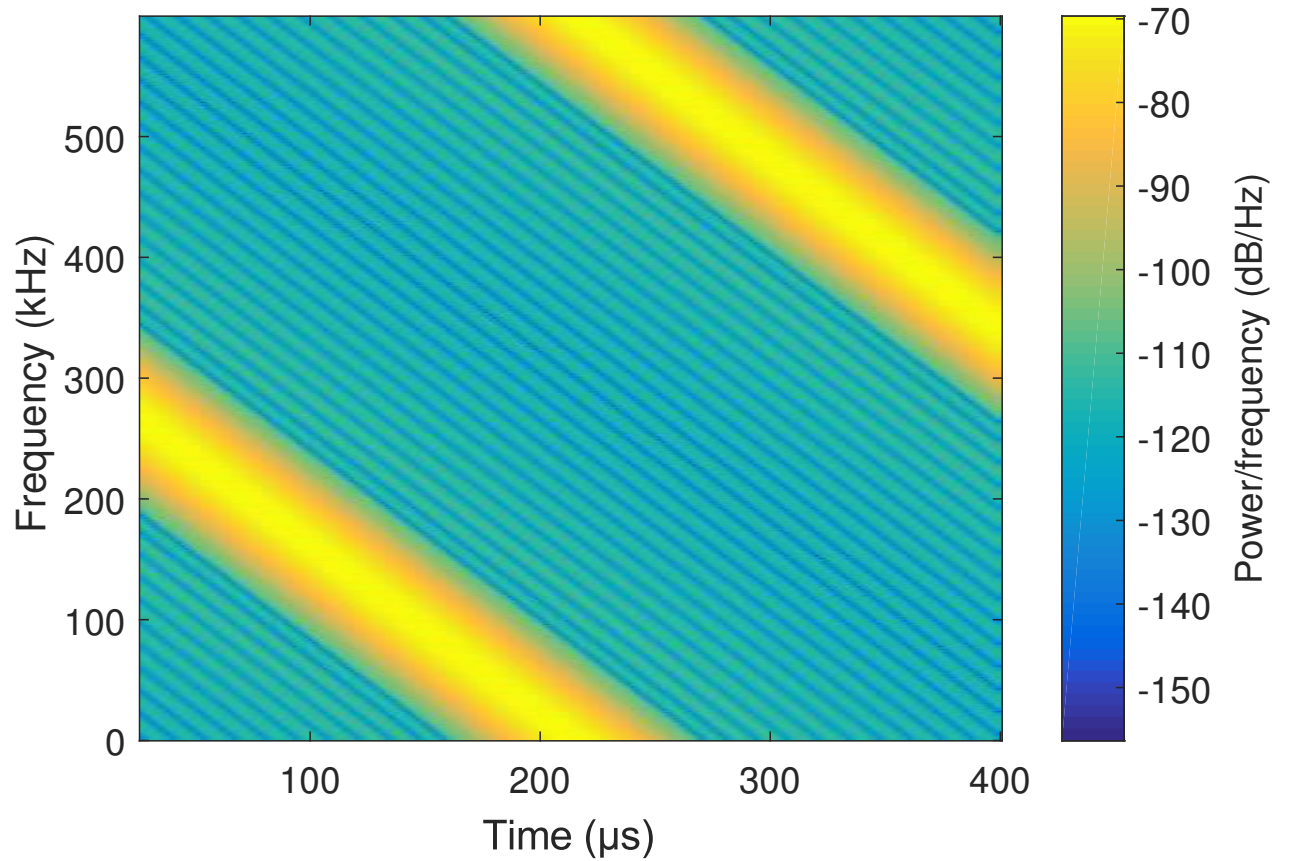


Figure 29: Sub-chirp #130 Spectrogram from a 256-length symbol of an OCDM scheme employing QPSK modulation as input data.

In order to provide a better view in terms of scale for comparison purposes, Fig. 29 shows the OCDM spectrogram using the aforementioned settings isolatedly.

## Appendix B – QR Codes

Videos showing the spreading effect obtained for types I-IV OCDM and also for passband OCDM can be seen in Fig. 30 through the QR codes labeled from (a) to (e), respectively.



Figure 30: QR Codes for video showing the spreading effect obtained for types I-IV and passband OCDM considering a 256-length symbol.

## Appendix C – PUBLICATIONS

The list of journal papers under preparation, written, or submitted during the graduate period is as follows:

- Leonardo de M. B. A. Dib, Victor Fernandes, Mateus de L. Filomeno, Moisés V. Ribeiro, “Hybrid PLC-wireless communication for smart grids and Internet of things applications,” *IEEE Internet of Things Journal*, 2017
- Leonardo de M. B. A. Dib, Guilherme R. Colen, Moisés V. Ribeiro, “Multiuser Orthogonal Chirp Multiplexing for PLC-based IoT Applications,” *IEEE Transactions on Communications*, 2018, to be submitted

The list of conference papers published during the graduate period is as follows:

- Leonardo de M. B. A. Dib, Victor Fernandes, Moisés V. Ribeiro, “A Discussion About Hybrid PLC-Wireless Communication For Smart Grids,” *XXXIV Simpósio Brasileiro de Telecomunicações - SBrT*, 2016
- Felipe A. Santos and Luã M. F. Da Silveira, Diogo Fernandes, Leonardo de M. B. A. Dib, Fabrício P. V. De Campos, Moisés V. Ribeiro, “Integration of a Smart Meter with the Brazilian Broadband PLC System,” *XXXIII Simpósio Brasileiro de Telecomunicações - SBrT*, 2015